Determination of stellar parameters for FGK-dwarf stars: the NIR approach

by

Daniel Thaagaard Andreasen

A thesis submitted in conformity with the requirements
for the degree of Doctor of Philosophy
Graduate Department of Departamento de Fisica e Astronomia
University of Porto

Dedication

To Linnea, Henriette, Rico, and Else
For always supporting me

Acknowledgements

Lorem ipsum dolor sit amet, consectetuer adipiscing elit. Ut purus elit, vestibulum ut, placerat ac, adipiscing vitae, felis. Curabitur dictum gravida mauris. Nam arcu libero, nonummy eget, consectetuer id, vulputate a, magna. Donec vehicula augue eu neque. Pellentesque habitant morbi tristique senectus et netus et malesuada fames ac turpis egestas. Mauris ut leo. Cras viverra metus rhoncus sem. Nulla et lectus vestibulum urna fringilla ultrices. Phasellus eu tellus sit amet tortor gravida placerat. Integer sapien est, iaculis in, pretium quis, viverra ac, nunc. Praesent eget sem vel leo ultrices bibendum. Aenean faucibus. Morbi dolor nulla, malesuada eu, pulvinar at, mollis ac, nulla. Curabitur auctor semper nulla. Donec varius orci eget risus. Duis nibh mi, congue eu, accumsan eleifend, sagittis quis, diam. Duis eget orci sit amet orci dignissim rutrum.

Nam dui ligula, fringilla a, euismod sodales, sollicitudin vel, wisi. Morbi auctor lorem non justo. Nam lacus libero, pretium at, lobortis vitae, ultricies et, tellus. Donec aliquet, tortor sed accumsan bibendum, erat ligula aliquet magna, vitae ornare odio metus a mi. Morbi ac orci et nisl hendrerit mollis. Suspendisse ut massa. Cras nec ante. Pellentesque a nulla. Cum sociis natoque penatibus et magnis dis parturient montes, nascetur ridiculus mus. Aliquam tincidunt urna. Nulla ullamcorper vestibulum turpis. Pellentesque cursus luctus mauris.

Abstract

Nam dui ligula, fringilla a, euismod sodales, sollicitudin vel, wisi. Morbi auctor lorem non justo. Nam lacus libero, pretium at, lobortis vitae, ultricies et, tellus. Donec aliquet, tortor sed accumsan bibendum, erat ligula aliquet magna, vitae ornare odio metus a mi. Morbi ac orci et nisl hendrerit mollis. Suspendisse ut massa. Cras nec ante. Pellentesque a nulla. Cum sociis natoque penatibus et magnis dis parturient montes, nascetur ridiculus mus. Aliquam tincidunt urna. Nulla ullamcorper vestibulum turpis. Pellentesque cursus luctus mauris.

Resumo

Nam dui ligula, fringilla a, euismod sodales, sollicitudin vel, wisi. Morbi auctor lorem non justo. Nam lacus libero, pretium at, lobortis vitae, ultricies et, tellus. Donec aliquet, tortor sed accumsan bibendum, erat ligula aliquet magna, vitae ornare odio metus a mi. Morbi ac orci et nisl hendrerit mollis. Suspendisse ut massa. Cras nec ante. Pellentesque a nulla. Cum sociis natoque penatibus et magnis dis parturient montes, nascetur ridiculus mus. Aliquam tincidunt urna. Nulla ullamcorper vestibulum turpis. Pellentesque cursus luctus mauris.

Contents

List of Tables

List of Figures

Chapter 1

Introduction

Ever since the dawn of time, the humankind have looked at the stars and wondered if we are alone in this Universe. To answer this question, one must look toward the field of extrasolar planets (exoplanets). This is a rapidly growing field in astronomy and science in general. Since the first confirmed discovery of an exoplanet around a millisecond pulsar in 1992 by Wolszczan and Frail (1992) and three years later, the more interesting exoplanet 51 Peg b discovered around a solar-type star by Mayor and Queloz (1995), more than 3600 exoplanets have been discovered at the time of writing, July 2017[1].

With the discoveries of exoplanets, the main focus is now mainly on finding the twin of Earth, that is a planet that can harbour life as we know it. However, it is not enough to simply discover small rocky exoplanets. Accurate and precise determination of the stellar parameters are crucial as the planetary parameters (radius, mass, bulk density, etc.) are directly derived from their host's parameters.

In this chapter there will be a general introduction to exoplanets, detection methods, and characterisation (Section 1.1). Then a throughout introduction on the exoplanet host stars (Section 1.2), which is the main focus on this thesis. While learning about host stars, and stars in general, the results have wide-spread applications, where some will briefly be discussed in the end of this chapter (Section 1.3) before an introduction on what this thesis will consists of (Section 1.4).

1.1   Exoplanets

The holy grail in the field of exoplanets is to find the first exoplanet with life. This is by no means an easy task. To give an idea of the difficulty of detecting life on an exoplanet, one must understand all the difficulties to simply detect and confirm an exoplanet. This will shortly be described in the sections below

1.1.1   Detecting exoplanets

There are sex ways of detecting exoplanets, some with advantages over others. In combination with each other, one can potentially learn a lot about the exoplanet(s).

It is important to note, that different things might mimic planetary signals, however they will not be described in this thesis. The confirmation of an exoplanet often happen, when two techniques are able to detect the same exoplanet.

---

[1]   http://exoplanet.eu/

1.1.1.1   Transit method

The most successful method, if based on numbers of exoplanets detected, is the transit method. This is a well-known method in astronomy, however only used in the last decade for detecting exoplanets. Before this, it has been used extensively for finding and characterising binary stars. The difference here is, that the exoplanet does not radiate (or at least very little radiation). An example of an exoplanet transiting a star can be seen in Figure 1.1.
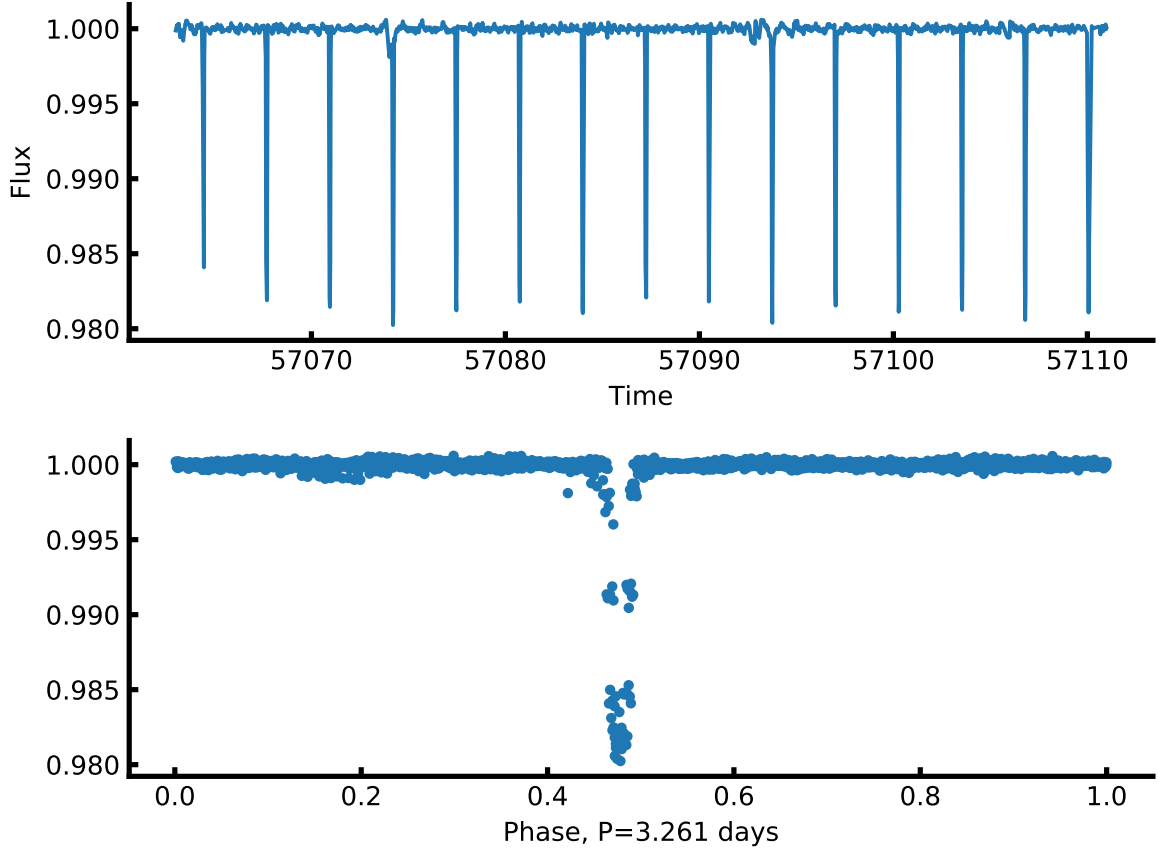
Figure 1.1: *Upper plot*: The lightcurve of a star with an exoplanet transiting. *Lower plot*: The phase curve of the above lightcurve.

As an exoplanet orbit a star, it might transit its host as seen from an observer here on Earth. This signal might be detected if the star's brightness is being monitored as a periodic signal. The decrease in brightness as the planet transit the star is directly related to ration between the stellar radius R_* and the planetary radius R_p:

$$k = \sqrt{\frac{R_p}{R_*}}, \tag{1.1}$$

where k is the depth of the transit compared to the total stellar brightness.

It is possible to obtain the radius of an exoplanet with this method. However, detailed analysis of the phase curve of an exoplanet can reveal the surface temperature of the exoplanet. The transit described

above is also known as the primary transit. If it is possible to detect the secondary transit, that is when the exoplanet goes behind the star as seen from Earth, the difference in light (planet + star right before secondary transit compared to just star) gives the flux of the planet and thus the surface temperature. This is a difficult task as secondary transits are intrinsic faint.

1.1.1.2   Radial velocity method

The radial velocity method is the indirect study of the motion of the host star using the Doppler effect caused by an orbiting exoplanet. This together with the transit method described above is by far the most successful methods to detect and characterise exoplanets. The periodic signal created by the exoplanet on the host star depends on the mass ratio between the star M_* and the planet M_p:

$$K = \frac{28.4329 \,\text{km/s}}{\sqrt{1-e^2}} \frac{M_p \sin i}{M_\text{Jup}} \left(\frac{M_* + M_p}{M_\odot}\right)^{-2/3} \left(\frac{P}{1\,\text{year}}\right) \tag{1.2}$$

where K is the semi-amplitude of the sinusoidal, e is the eccentricity, i is the inclination, P is the orbital period, and M_Jup is the mass of Jupiter. Since $M_* \gg M_p$, the term $M_* + M_p \simeq M_*$ in order to simplify the equation. Often a circular orbit is assumed, $e = 0$. The sinusoidal motion of the star can be seen in Figure 1.2 where both the time series and the phase curve is presented for an exoplanet.
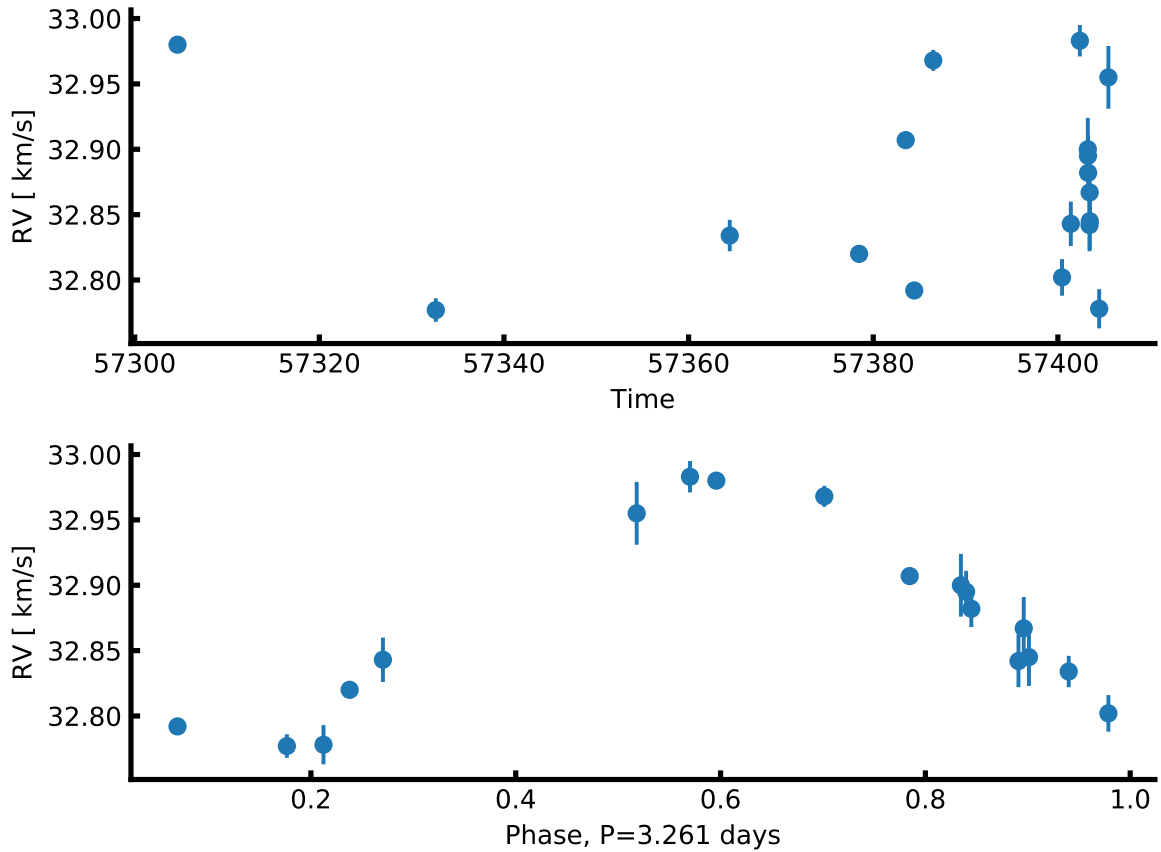
Figure 1.2: *Upper panel*: RV time series of EPIC 9792 from the SOPHIE spectrograph. *Lower panel*: Phase curve of the time series above, using the period of 3.261 days.

In order to apply the radial velocity method for detecting exoplanets, it is necessary to collect spectra, high resolution but often not high S/N, in order to cover most part of the phase of the orbit. These spectra are often combined after the detection of the exoplanet, in order to increase the S/N. This combined spectrum can then be used for characterising the host star.

This method is sensitive to close-in massive exoplanets, also known as hot Jupiters. In combination with the above mentioned transit method, the mass and radius of an exoplanet can be derived, and thus the bulk density which might give hints of the structure and composition of the exoplanet.

1.1.1.3 Direct imaging

Direct imaging is probably the easiest method to understand, however it is quite difficult to actually use this technique. In its core, one has to carefully block the light of a star, and directly imaging the exoplanets around it. However, it is extremely difficult to block the light of the host star and find the reflected light of the exoplanet(s) in orbit.

This technique is sensitive to exoplanets which reflect a lot of light, i.e. a high albedo, and in wide orbits as they are less contaminated by the residual starlight.

1.1.1.4 Astrometry

Using astrometry to detect exoplanets is very similar to the RV method described above in Section 1.1.1.2. Here an observer carefully detect the minute motion of a star caused by an exoplanet. Unlike the RV method, this technique (astrometry) actually looks for changes in the coordinates of the star. This technique has also been used to detect low luminosity stellar companions as e.g. Sirius B.

This technique is sensitive to massive exoplanets as they cause a larger motion compared to lighter companions.

1.1.1.5 Transit timing variation

This technique of detecting exoplanets is a highly indirect method of detecting exoplanets. Here an observer first detect a transiting exoplanet as explained in Section 1.1.1.1. Then variations in the occurrence of mid-transit can be detected if a second non-transiting exoplanet interact with the primary transiting exoplanet (planet-planet interaction). This interaction will periodically course the mid-transit to happen ahead/behind of the time if only one exoplanet would be present.

A careful analysis of the transit timing variations (TTV) can lead to the mass of the secondary non-transiting exoplanet. However, its radius will be unknown. Most of these exoplanets pairs which shows TTV are in an orbital resonant. This technique as well, is more sensitive to massive exoplanets as they will induce a higher signal.

1.1.1.6 Microlensing

This technique is very exotic and not very useful, however since a few exoplanets have been discovered by this technique it deserves a mentioning. The core theory in this technique is the well-known General Relativity. Here an observer looks at a distant star (star A) as a star between the observer and the distant star (star B) passes in front of the line of sight. Star B will act as a microlens and increase the magnitude of star A. This increase of magnitude will reach its maximum as the two stars are most aligned as seen from Earth.

To use this for detecting exoplanet, there will have to be an exoplanet orbiting star B. This act like another lens, momentarily make a secondary increase in magnitude. The amount of increase in magnitude is related to the mass of the exoplanet. The higher the mass, the higher the effect.

While this exotic technique is interesting and has proven successful, it is not very useful as it only occurs once. The stars observed with this technique are often faint, thus making follow-up RV detection very difficult if not impossible with the current instruments.

1.1.2 Towards the Earth twin

The above mentioned techniques will be used to find the Earth twin. Especially will the two first techniques (transit and RV method) be the ones finding the smallest exoplanets as a wide range of instruments are being developed dedicated for this. Since the detection of the first exoplanet around a solar-type star by Mayor and Queloz (1995), the community has been able to detect lower mass exoplanets as seen in Figure 1.3.

Write about JWST, Espresso, NIRPS, etc.
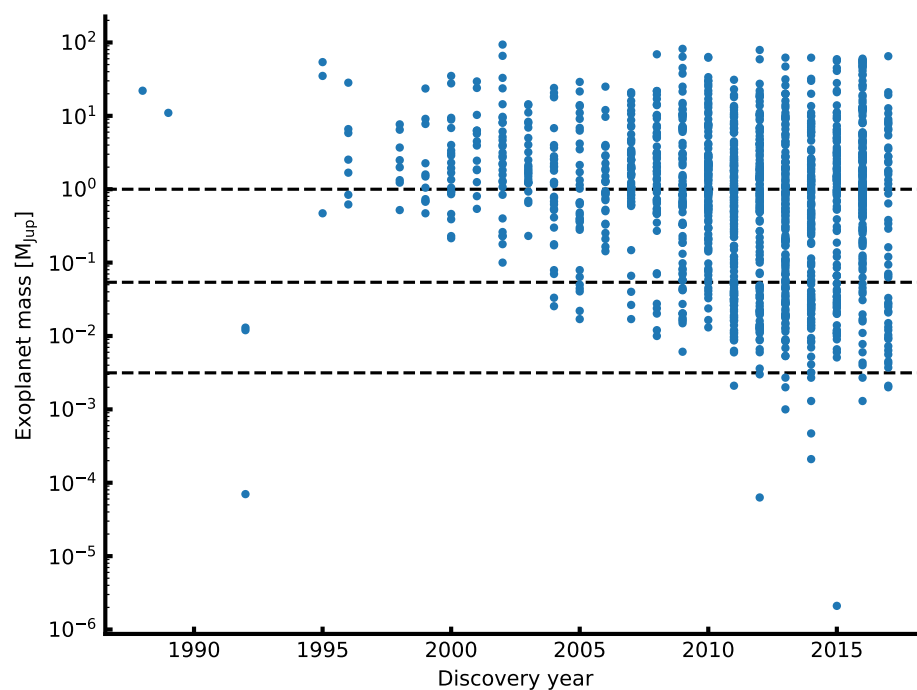
Figure 1.3: The mass of exoplanet since the detection of the first exoplanet until now. The horizontal lines are the mass of Jupiter (upper), Neptune (middle), and Earth (lower).

While the first many discoveries of exoplanets were the, at the time, exotic and strange hot Jupiter like exoplanets in close orbits, the time have come to detect exoplanets with both lower mass and wider orbits. It is crucial to have high precision instruments and long surveys to detect those exoplanets. Missions as *Kepler* and CoRoT have been excellent for this, since they have focused on few fields of the sky for a long time.

The first place to look for Earth's twin is around a solar twin. However, since these stars are quite hot, the habitable zone will also be far from the host star. Indeed, to detect a copy of our own solar system we would need to detect the minute signature of an exoplanet in a 1 year orbit around its host

star (a solar twin). If detected with the transit method, more than one transit is needed, hence this will take at least two years, and probably even longer. The endeavour to get the follow-up RV afterwards will also be extremely challenging with today's technology, and only the next generation of spectrographs will be able to detect these signals.

Therefore, it is not a surprise that an effort have been towards detecting Earth-like planets around less massive stars. These stars (M stars) are also colder, hence the habitable zone will be closer to its host compared to the more massive and hotter stars. The nature have been kind, since it seems that the M stars are prone to produce rocky planets rather than giant planets. The shorter period means that the surveys can be shorter for these planets. Moreover, since they are smaller the signal from a transit will be easier to detect (see Equation 1.1). Similarly will the RV signal be larger for an Earth-like planet in the habitable zone around an M star compared to a similar exoplanet around a G star. Both due to the lower period and due to the lower mass of the host star (see Equation 1.2).

While M stars seems to be the place to look for the Earth's twin, there are still some challenges to tackle. Foremost is the detailed characterisation of the host star, which are particular troublesome for these stars. This is something that will be focused on in the following section.

1.2 Planet host stars

With the present diversity of exoplanets it becomes increasingly important to get an accurate and precise characterisation of the exoplanets in order to study them in samples and on an individual level. An accurate and precise characterisation can give us an idea whether the planet is rocky, composed of water, gaseous, or some other more exotic combination. To characterise stars it is common to use several different methods to learn about different aspects of a star. If the effective temperature is needed, the most reliable comes from the analysis of a high resolution and high signal-to-noise (S/N) spectrum. The same is used to identify chemical abundances of the photosphere of the star, while methods like asteroseismology are used to determine the mass and radius of a star, two parameters which are crucial to characterise the orbiting exoplanet.

Some of these methods are described in greater detail in Chapter 3. These methods work best together. In the example given above, the effective temperature is needed before asteroseismology can be used to determine the mass and radius. These two methods goes extremely well together as the most commonly used detection methods (transit and RV) will obtain the data needed. From the transit method, one will obtain a lightcurve which can be used to detect the transits. If these are carefully removed from the lightcurve, the residual might contain stellar oscillations used to perform an asteroseismic analysis. Likewise will the spectra obtained from the RV method to detect/confirm an exoplanet be used for the stellar characterising afterwards by combining them, after shifting to a RV= 0 km/s, to increase the S/N. This combined high S/N spectrum is ideal for the spectral analysis of stars.

This tactic where spectroscopic analysis is used in conjunction with asteroseismology have proven very successfulfor characterising an exoplanet system (host star and exoplanet). However, it does have its limitations. It can be difficult to detect solar-like oscillations as the stars get colder than the Sun. Especially have the community yet to detect any solar-like oscillations in M dwarf stars. Other times the problem is on spectroscopy. Many of the detected exoplanets are from the *Kepler* mission, where many of the host stars are very faint. While it is not impossible to make spectroscopic observations, it is extremely time consuming. Therefore brighter targets are often prioritised, unless there is an exceptional

case.

With the search for the Earth twin around the small cool M dwarf stars, it is important to develop reliable methods for the analysis of these stars. The tools for detecting the exoplanets are currently more mature than the host star analysis. However, with the advance of NIR spectrographs this is slowly changing. It is general believed that a NIR analysis is needed to characterise M stars. The reason is simple that these stars are so intrinsic faint, that it is important to collect as much flux as possible. This happens in the NIR. Moreover, for spectroscopic studies, the optical spectrum of these stars are heavily contaminated by molecular absorption lines, which depress the continuum. During spectroscopic topics, it is crucial to get the continuum placement correct. In the NIR the continuum depression is less severe, however still challenging. This can clearly be seen in Figure 1.4 where the optical and NIR part of the spectrum for HD 79210, a K7 dwarf star (Kirkpatrick et al., 1991), is plotted. The spectrum was obtained by CARMENES at the same time and have therefore the same exposure time, hence roughly similar S/N. However, it is clear that the NIR spectrum is far less contaminated by molecular lines.
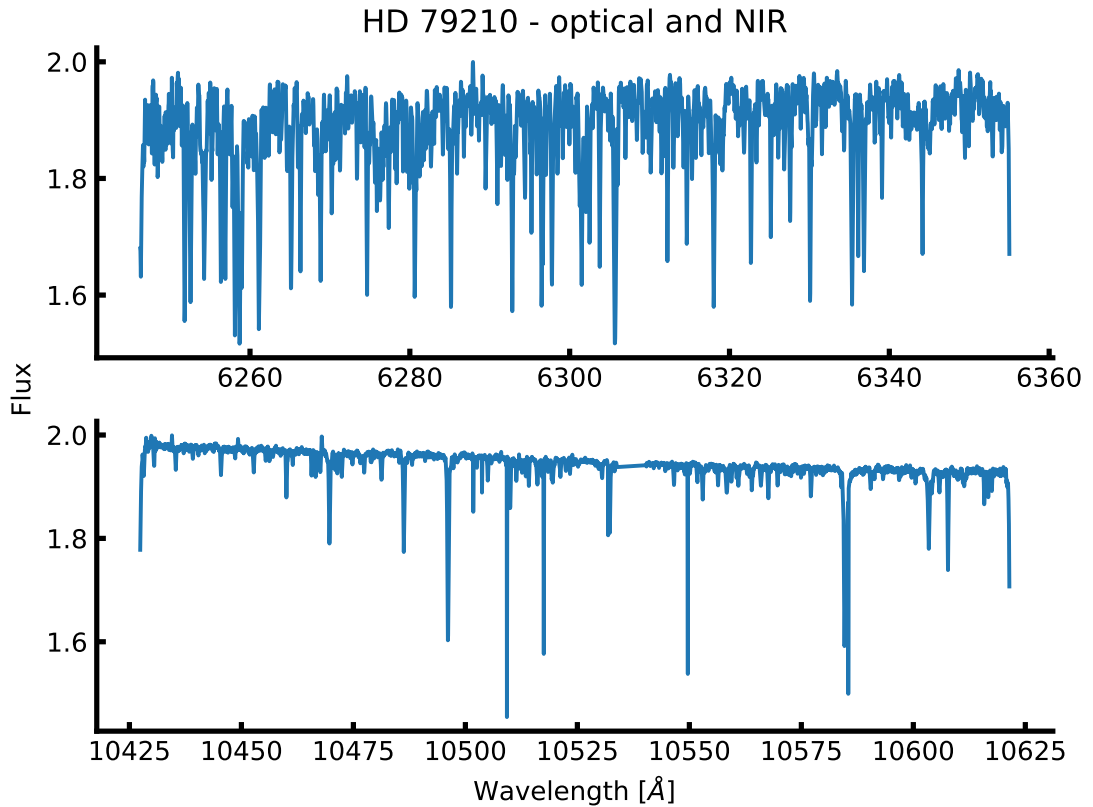
Figure 1.4: Comparison between a optical and NIR part of the spectrum of HD 79210 obtained by the CARMENES spectrograph. This clearly illustrate why NIR spectra are preferred over optical spectra for cool stars. HD 79210 is a K7 dwarf star.

The main goal of this thesis is to work towards a consistent deviation of stellar atmospheric parameters for M stars. Before tackling the M stars, it is important to have a method that work well for solar-like stars (FGK).

1.3 Applications from knowing the stars

1.4 This thesis

Chapter 2

Theory

To encompass all theory regarding stellar structure, evolution, and their atmosphere is far beyond the scope of this thesis. Rather the theory needed is presented below with highlights on the most important aspects.

2.1 Stellar structure

The structure of a non-rotating spherical stars can be described by five rather simple differential equations (see e.g. Kippenhahn and Weigert, 1994) presented below:

1. **Equation of Continuity**

   Relation between the mass, m, the density, ρ, at a symmetric shell at radius r

   $$\boxed{\frac{\partial r}{\partial m} = \frac{1}{4\pi r^2 \rho}.}$$
   (2.1)

2. **Equation of Hydrostatic Equilibrium**

   The equation of hydrostatic equilibrium shows how a star in equilibrium is balanced between two forces. The inward force from gravity and the outward force from pressure, P,

   $$\boxed{\frac{\partial P}{\partial m} = -\frac{Gm}{4\pi r^4}.}$$
   (2.2)

   When working with asteroseismology a time dependent perturbation to this equation is added (see e.g. Aerts et al., 2010, for a thorough discussion). However, this term is neglected here.

3. **Equation of Energy Conservation**

The equation of energy conservation shows how the energy is produced and lost throughout the star.

$$\frac{\partial l}{\partial m} = \varepsilon - \varepsilon_\nu + \varepsilon_g, \tag{2.3}$$

where ε is the energy production in the centre of the star, ε_ν is the energy lost by neutrinos which is always positive, ε_g is a source function of time-dependent terms, and l is the luminosity at m. ε_g comes from the fact that non-stationary shells can change its internal energy, and thus exchange mechanical energy with neighbouring shells.

4. **Equation of Energy Transport**

Energy transportation throughout the star is described with the following equation

$$\frac{\partial T}{\partial m} = -\frac{GmT}{4\pi r^4 P} \nabla_{\text{rad}}, \tag{2.4}$$

where ∇_{rad} is the radiative temperature gradient, and T is the temperature. The value of the temperature gradient compared to the radiative temperature gradient tells if the energy is transported by convection or radiation. In our Sun the outer layer are convective while the inner layer are radiative.

5. **Equation of Chemical Composition**

In this last equation we see the evolution of an element, X_i, when it reacts with other elements with reaction rates r_{ji} and r_{ik}

$$\frac{\partial X_i}{\partial t} = \frac{m_i}{\rho} \left(\sum_j r_{ji} - \sum_k r_{ik} \right). \tag{2.5}$$

Note that this is the only time-dependent equation of the five presented.

These five fundamental equations are implemented in stellar evolutionary codes, which we will use in later chapters. The many different codes that exist take other things into account, e.g the star can rotate, and it may not always be in hydrostatic equilibrium (this is important if we want our star to pulsate). For simplicity we have only presented time-dependence in the Equation of Chemical Composition since timescales of rotation, pulsations, and activity are much shorter than the long timescale found in chemical composition changes.

2.2 Stellar atmosphere

Much of this Section is inspired by Gray (2005). While all the figures here were made by the author of this thesis, most of them can be found in Gray (2005) as well.

Stellar atmospheres are rather complex. This is where the energy produced in the interior of the stars are released. However, the atmosphere of a star is not transparent to all light, and some of the light is absorbed or scattered in the atmosphere. In the case of absorption the light will later be emitted in a random direction. This is seen as an absorption line in the stellar spectrum. The different elements in the atmosphere is the reason for absorbing light at specific wavelength. The strength of the absorption depends on the physical conditions in the atmosphere, the effective temperature (T_{eff}), the pressure/gravity ($\log g$), the overall metallicity ([Fe /H]), the specific abundance of a given element if different from the overall metallicity (A), and the atomic characteristics of the transition coursing the absorption line.

It is important to know the fraction of atoms excited to the nth energy level, N_n. This fraction is proportional to the statistical weight g_n and the Boltzmann factor and is described as:

$$\boxed{\frac{N_n}{N} = \frac{g_n}{u(T)} 10^{-\theta \chi_n}} \qquad \qquad \text{Boltzmann}$$

This equation is also called the Boltzmann equation. Here N is the total number of atoms per unit volume, $u(T) = \Sigma g_i e^{-\chi_i / kT}$ is the partition function, k is Boltzmann's constant, T is the temperature, and χ_n is the excitation potential for the lower energy level.

While atoms can get excited following Boltzmann's equation above, they can also get ionized. The ionization ratio for a collision dominated gas (which is a good approximation for FGKM stars) is described by the Saha equation. This equation relate the ratio of atoms in state r to atoms in the excited state above for the same element, $r + 1$, in the following way:

$$\boxed{\frac{N_{r+1}}{N_r} = \frac{1}{P_e} \frac{(2\pi m_e)^{3/2} (kT)^{5/2}}{h^3} \frac{2u_{r+1}(T)}{u_r(T)} e^{-I/kT} = \frac{\Phi(T)}{P_e}} \qquad \text{Saha}$$

here m_e is the electron mass, h is Planck's constant, I is the ionization potential of the neutral atom, and $\Phi(T)$ is all not related to the electron pressure, P_e.

The atomic lines are characterised by a few quantum mechanical descriptors.

- **T**he wavelength, λ of an absorption (or emission) describes the energy difference between the two energy levels where the transition occurs.

- **T**he ionization state, e.g. Fe I describes iron in its atomic form, while Fe II describes iron in its first ionized form.

- **T**he excitation potential χ. This gives an idea how deep in the atmosphere a line is formed. If χ is high, then higher temperatures (i.e. higher random motion and more collisions between the atoms) is required for forming the absorption line. These higher temperatures are found deeper in the atmosphere.

- **T**he oscillator strength, $\log gf$, is related to the atomic transition probability.

- **T**he damping coefficients, is a natural damping (also known as radiation damping) caused by the uncertainty of lifetime in an energy level according to Heisenberg's uncertainty principle. This is related to a uncertainty in the energy level and thus a natural broadening is introduced.

These are essential to know from either theoretical calculations or experiments. The oscillator strength is a quantity that is difficult to measure, and this is often changed when absorption lines are matched with real observations of e.g. the Sun. This is a way of calibrating a line list and will be described in detail in Section 2.3.

It is important to mention that one of the main differences between absorption lines at different wavelengths is the excitation potential. The energy levels of an atom gets denser packed as the energy level increase as shown in Figure 2.1 for hydrogen. For hydrogen the energy levels E_n follow the very simple formula from Bohr's atomic model, $E_n = \frac{-13.6\,\text{eV}}{n^2}$, where n is the principal quantum number, and $13.6\,\text{eV}$ is the ionization energy for hydrogen, i.e. the minimum amount of energy required to ionize hydrogen. The energy levels for heavier atoms show a similar structure. The outer electron for a multi-electron atom is partially shielded from the nucleus by the inner electrons, and thus does not experience the full charge Z but rather an effective charge Z_eff, giving the expression

$$E_n = -hcR_\infty \frac{Z_\text{eff}^2}{n^2}, \tag{2.6}$$

where h is Planck's constant, c is the speed of light, and R_∞ is Rydberg's constant.

With increasing n the energy levels get closer, or in other words the photon required to excite an electron from one energy level to a neighbouring state will get redder. These redder photons used for exciting an atom are the absorption lines seen in the NIR. However, the excitation to the lower state is from thermal motion and not coursed by photons. Since tight energy levels require a highly excited lower state, the temperature required here are similar high, which means that the NIR lines are typically formed in the deeper layers of the atmosphere compared to absorption lines seen in the optical part of the spectrum.

The above discussed energy transitions are purely electronic, however there exists so called fine structure transitions as well. This is due to the spin of the electron (or magnetic moment) interacting with the orbital angular momentum of the electron. This leads to a splitting of the absorption line. In atoms there also exists an even finer structure, commonly known as the hyperfine structure. This structure arise due to the interaction between the magnetic field created by the electrons and the nuclear spin. These splittings are important to consider for some transitions and some atoms. For Fe the hyperfine structure is not important since the net nuclear spin of protons is 0 because there is an even number of protons, hence hyperfine structure is only important for atoms with an odd number of protons. There are other splitting and shift for spectral absorption lines like the Zeeman splitting coursed by an external magnetic field, and the Stark effect splitting a line due to an external electric field. These two last effect are minor and will not be discussed more, however it is worth noting that the Zeeman splitting can be used to measure the strength of a magnetic field in a star if this is strong enough.

2.2.1 Atmosphere models

In order to derive abundances or calculate a synthetic spectrum, two main things are needed: 1) And atmosphere model, and 2) a radiative transfer code that solves the equations above. There are different atmosphere models available. Throughout this thesis the ATLAS9 model atmosphere are used (Kurucz, 1993). Other mention-able atmosphere models includes MARCS models (Gustafsson et al., 2008) and the PHOENIX models (Husser et al., 2013). An atmosphere model is a description of the structure of the atmosphere. This description has a number of quantities. The atmosphere model grids that are
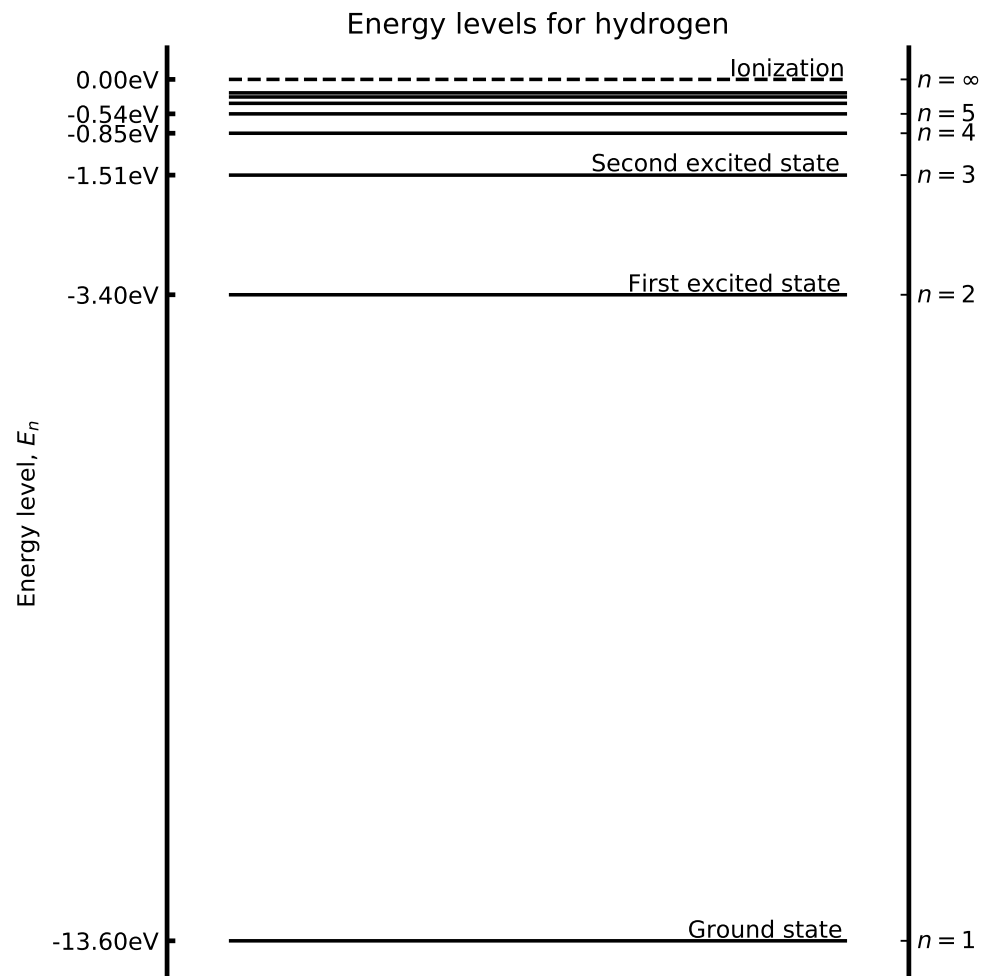
Figure 2.1: Energy levels for hydrogen, $E_n = \frac{-13.6\,\text{eV}}{n^2}$.

available and used here have 72 layers. Each layer includes physical quantities such as temperature, gas and electron pressure, the optical depth, etc. The models can be calculated on the fly, but it is common practise because of computational reasons to pre-calculate a grid of atmosphere models at certain T_{eff}, $\log g$, and [Fe /H]. A specific atmosphere model is then obtained from this grid by interpolating from nearest neighbours. The interpolation code used throughout this work includes the four nearest neighbours in the T_{eff}-space, and the two nearest neighbours in both the $\log g$- and [Fe /H]-space, in total $4 \times 2 \times 2 = 16$ atmosphere models to generate a single interpolated atmosphere model.

2.2.2 Radiative transfer code - `MOOG`

As mentioned above, a radiative transfer code is needed to solve the equations above. There are many different codes that does this. Here the `MOOG` code us used (Sneden, 1973). This code has different drivers, only some are used here.

- Derive a theoretical equivalent width (see Section 2.2.3 for details) for a given star, i.e. atmosphere model with a given set of atmospheric parameters.

- Derive line abundance from a measured equivalent width for a given model atmosphere.

- Calculate a synthetic spectrum for a given model atmosphere and atomic line list.

- Calculate the curve-of-growth for an atomic line.

There exists other drivers as well, but these are the ones used here. Some only for visualising the figures below.

2.2.3 The equivalent width

Measuring the equivalent width (EW) of spectral lines are important for some analysis of stellar spectra. The EW is a measure of the strength of the line, and dependent on the atmospheric conditions in where the spectral line is formed, such as T_{eff}, $\log g$, [Fe /H], and ξ_{micro}.

The EW is mathematically described as integrating over the entire line, and assign this area to a rectangle from 0 to the continuum flux (F_c) with the width, EW. This is illustrated in Figure 2.2 and the equation below:

$$EW = \int_0^\infty \frac{F_c - F(\lambda)}{F_c} d\lambda, \tag{2.7}$$

where λ is the wavelength. This is integral is assuming there is only one single line, hence the integral is over all wavelength. In practice the integral is calculated in small windows around a spectral line. See Section 3.3.2 for more details on how this is performed in practice. The unit of the EW is the same as the wavelength used. Throughout this thesis we will use Ångström ($1\,\text{Å} = 0.1\,\text{nm}$) for the wavelength, and mÅ for the EW.

2.2.3.1 Temperature dependence

As mentioned above the EW depends on the atmospheric parameters. The dependence on T_{eff} is the strongest dependence. At low T_{eff} neutral elements, say Fe I, are the strongest lines as the number of
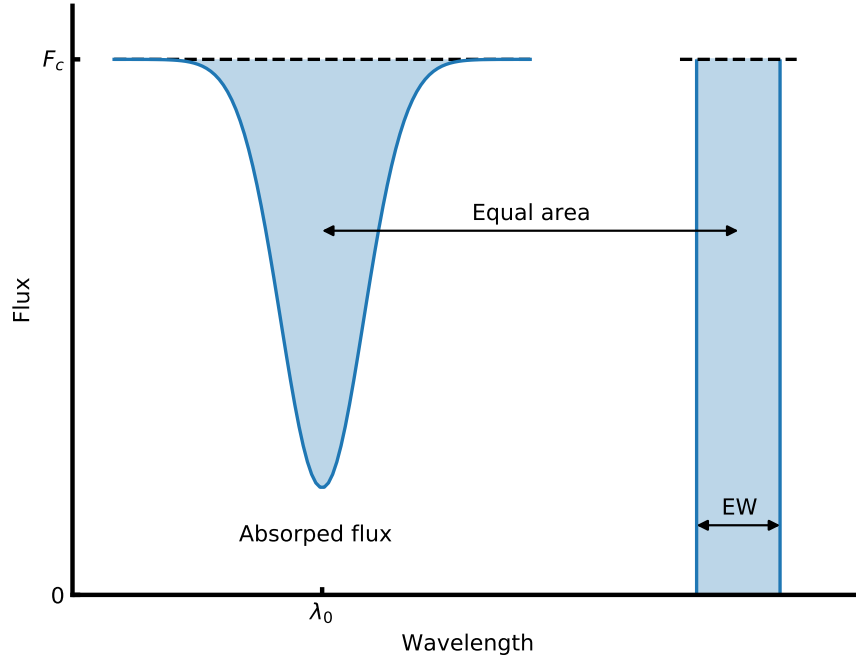
Figure 2.2: An absorption line centred at λ_0 normalised at the flux level F_c. The area of the absorption line to the left is equal to the blue shaded area in the rectangle to the right with width EW.

ionized atoms are too small to contribute significantly to the EW. This is the result the Saha equation. As T_{eff} increases Fe I is converted into ionized Fe II. Slowly, as the number of Fe I decreases so does the EW, and likewise as the number of Fe II increases so does the EW. This goes on until second ionized atoms, Fe III, are formed and the same situation arise again. This is illustrated in Figure 2.3 where the EW of two iron lines, one neutral and one ionized, are plotted against T_{eff}. These two lines have similar EW in the Sun: 46.2 mÅ and 53.9 mÅ for the Fe I and Fe II line respectively.

2.2.3.2   Pressure dependence

Pressure dependence in the stellar atmosphere can be related to the gravity dependence. There are many ways to measure the pressure, and thus the gravity which is what is ultimately the goal with the measurement of $\log g$. Below are listed some of the most common methods to measure $\log g$ from spectroscopy.

- Continuum: The Balmer jump is the only continuum feature sensitive enough to estimate the $\log g$.

- Hydrogen lines: Hydrogen profiles are pressure sensitive and can therefore be used to estimate $\log g$. However, the gravity dependence rapidly diminishes for temperatures above $10\,000$ K.

- Other strong lines: There exists other strong lines with pressure-broadened wings such as the Ca II H and K lines. These are better for cooler stars than the hydrogen lines described above.

- Weak lines: By comparing two stages of ionization for the same element it is possible to obtain $\log g$ using weaker or modestly strong lines.
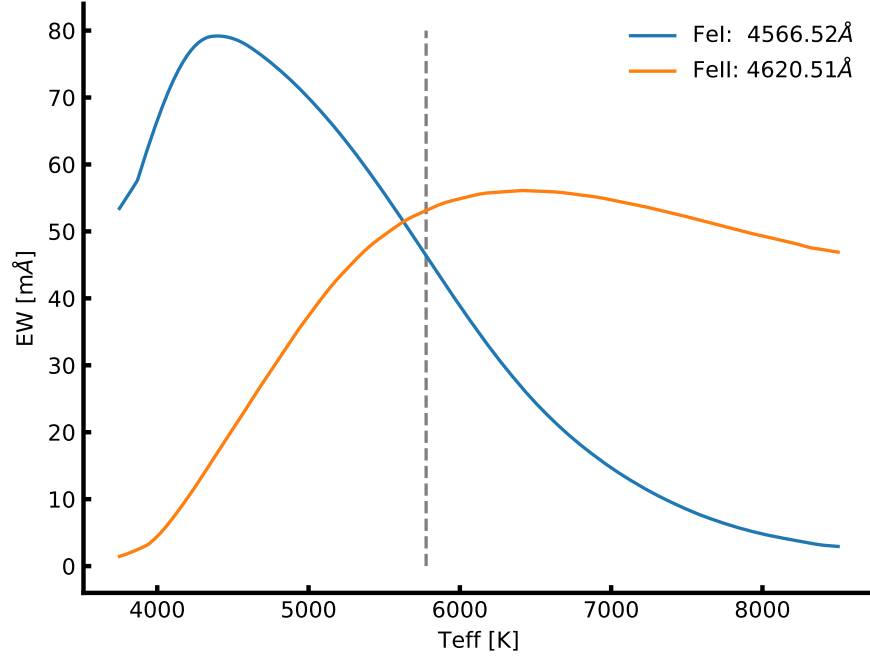
Figure 2.3: The EW for a Fe I and Fe II line with increasing T_{eff}. The two lines have similar EW in the Sun and are found in the optical part of the spectrum. The vertical line show the solar T_{eff}.

In this thesis weak lines are used to measure $\log g$. More specifically a comparison between Fe I and Fe II lines are used. For FGK stars, as the atmosphere contracts (i.e. $\log g$ increases) the pressure likewise increases, which in turn means that both the gas pressure, P_g, and electron pressure, P_e, increases. Since hydrogen is the main electron contributor, but not fully ionized for these stars, the electron pressure is much smaller that the gas pressure. The gas pressure follow a simply empirical approximation with gravity:

$$P_g \approx \text{constant} \, g^{2/3}, \tag{2.8}$$

where g is the gravity. The electron pressure is given by

$$P_e \approx \text{constant} \, g^{1/3}. \tag{2.9}$$

There are three cases for which a line show dependence on gravity, when considering only weak lines:

1. A weak line formed by any ion or atom, where most of the element is in the next higher ionized state.

2. A weak line formed by any ion or atom, where most of the element is in the same ionized state.

3. A weak line formed by any ion, where most of the element is in the next lower ionized state.

Using the Saha equation for case 1, it is important to note that the number of the atoms in the highest state is roughly equal to the total number of atoms of that element, $N_{r+1} \approx N$. Hence

$$N_r \approx \text{constant } P_e \tag{2.10}$$

which means that the line absorption coefficient is

$$l_\nu \approx \text{constant } N_r \approx \text{constant } P_e. \tag{2.11}$$

The strength of a weak line, R, is proportional to the ratio of the line to the continuous absorption coefficient, κ_ν

$$R = \frac{F_c - F_\lambda}{F_c} = \text{constant } \frac{l_\nu}{\kappa_\nu}. \tag{2.12}$$

When negative hydrogen dominates κ_ν which is the case here it is proportional to the electron pressure, $\kappa_\nu \propto P_e$ which means the line strength is not proportional to to electron pressure:

$$R = \frac{l_\nu}{\kappa_\nu} \approx \text{constant}. \tag{2.13}$$

For case 2, the approach is the same, here $N_r \approx N_{r+1} \approx N = \text{constant}$. This leads to $l_\nu \approx \text{constant}$, eventually giving

$$R = \frac{l_\nu}{\kappa_\nu} \approx \frac{\text{constant}}{P_e} \approx \text{constant } g^{-1/3}. \tag{2.14}$$

Only the first two cases are relevant for solar-type stars used in this thesis, and the relation for the third case will be omitted.

In Figure 2.4 is shown how the Fe II line used previously change with $\log g$. The curve of growth is shown in the upper panel, while a synthetic spectrum for each $\log g$ is presented in the lower left panel. It is clear that the ionized line is sensitive to $\log g$ as shown in the lower right panel, where the correlation between the abundance and $\log g$ is 0.40. This is expected as can be seen in Gray (2005, Table 16.1). There is used $\delta \log A / \delta \log g$ as an indicator, and for neutral elements the correlation is much weaker. It is important to note that the correlation does change with T_{eff} and the element used.

2.2.3.3   Abundance dependence

The abundance of a given element obviously has an effect on the EW. The more abundant an element is, the more photons can be absorbed thus increasing the EW. However, the relationship is not strictly linear. For weak lines (GIVE RANGE) EW is approximately linear with the abundance, however it reach a plateau where the core of the line saturates. In this regime the EW only increases slowly, until the absorption "spills" into the wings and the increase is again linear. However, for these strong lines the profile is no longer Gaussian. The curve of growth for the same Fe I line used in Figure 2.3 is shown in Figure 2.5. Instead of EW it is common to use the reduced EW, $\log(EW/\lambda)$[1], which we will use more later. Instead of the abundance of a line, the oscillator strength, $\log gf$, is used.

---

[1]   The reduced EW is useful since it normalises Doppler-dependent phenomena, such as microturbulence and thermal broadening.
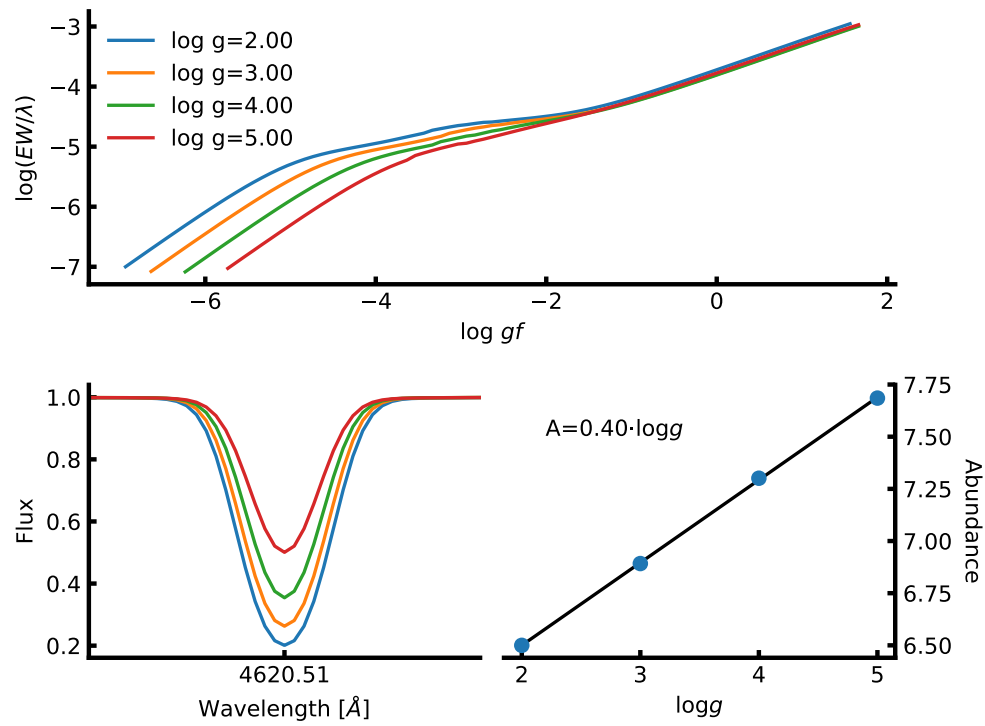
Figure 2.4: *Upper panel*: Curve of growth for same Fe II used in Figure 2.3 for four different $\log g$ values. Here it is the weak lines mostly affected by the change in $\log g$. *Lower left panel*: Synthetic spectra of the same line. The colour scale is the same. *Lower right*: The abundance for the line at different $\log g$. A strong correlation (0.40) is seen.
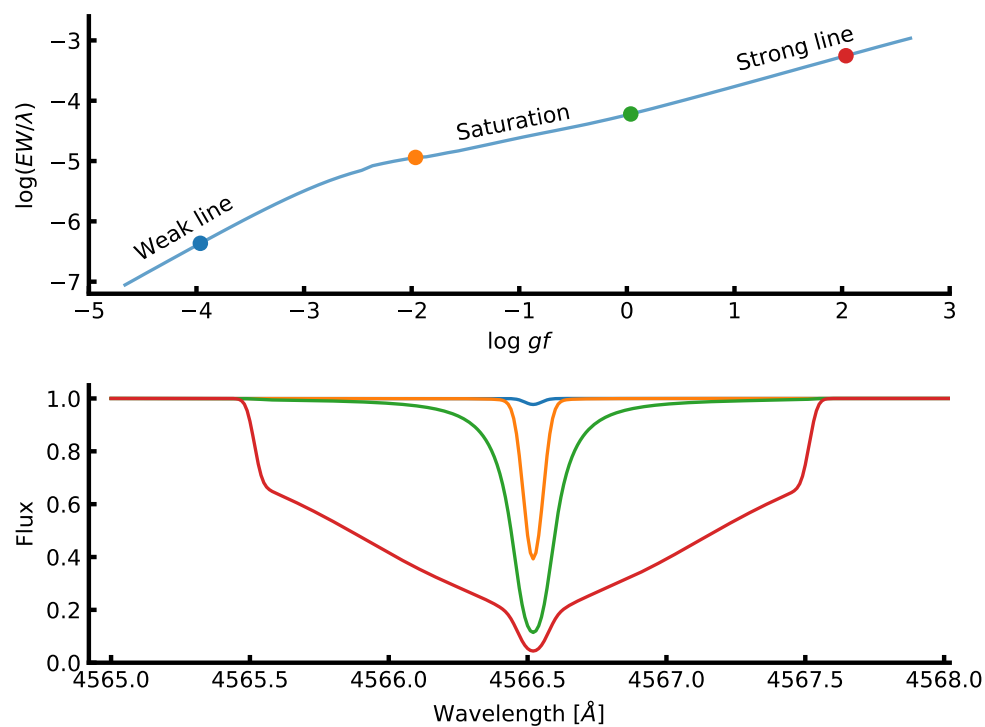
Figure 2.5: *Upper panel:* Curve of growth of the same Fe I line as used in Figure 2.3. Four points are marked which is shown in the *lower panel* as a synthetic spectral line. The RW (proxy for EW) is clearly increasing with log *gf* (proxy for abundance).

2.2.3.4 Microturbulence

Small-scale motion, that is motion of material at length scales small compared to the unit optical depth, are called microturbulence, ξ_{micro}. This is not to be confused with macroturbulence, which is motion of material at scales larger than the unit optical depth. The latter is associated with granulation and will not be discussed further in this thesis. ξ_{micro} comes into play when looking at the curve of growth for saturated lines (i.e. between green and red points in Figure 2.5). If no ξ_{micro} is assumed, then the measured abundance is higher than predicted by models based on thermal and damping broadening alone. In Figure 2.6 is shown three curves of growth with $\xi_{\text{micro}} = 0.5 \, \text{km/s}, 2.5 \, \text{km/s}, 5.0 \, \text{km/s}$. As ξ_{micro} increases, so does the EW and hence the abundance.
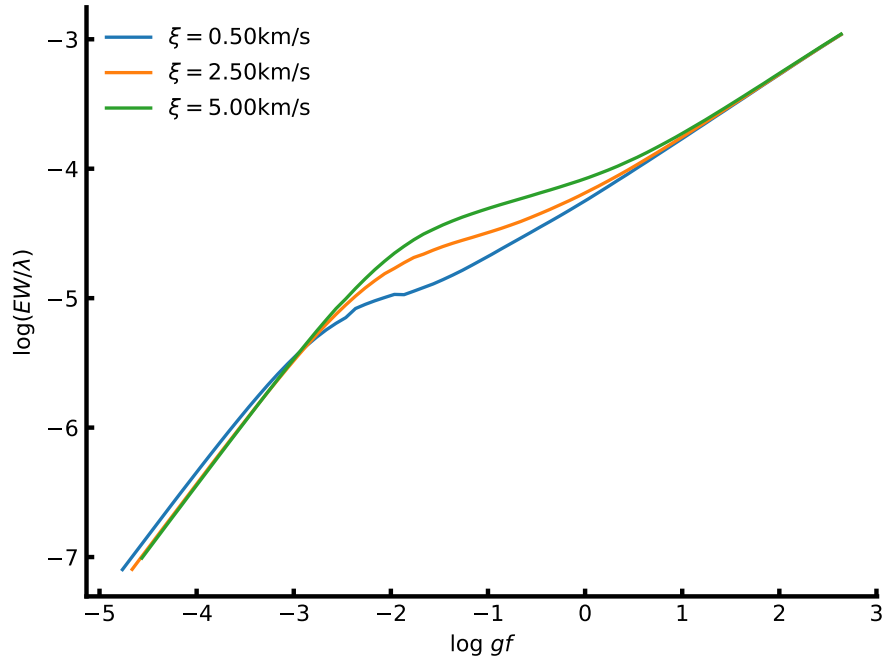
Figure 2.6: Curve of growth for three different values of ξ_{micro}. The EW is increasing with increasing ξ_{micro}.

The broadening of an absorption line measured by the shift in wavelength, $\Delta\lambda$, when ξ_{micro} is included is defined as:

$$\Delta\lambda = \frac{\lambda_0}{c} \sqrt{\frac{2kT}{m} + \xi_{\text{micro}}^2}, \tag{2.15}$$

where c is the speed of light, λ_0 is the rest wavelength of the given line, k is Boltzmann's constant, T is the temperature, and m is the mass of the atom. Setting $\xi_{\text{micro}} = 0 \, \text{km/s}$, we end up with thermal broadening.

2.3 Line list and atomic data

As mentioned above, the atomic data of the absorption lines are required. These data can be found in a database such as *The Vienna Atomic Line Data Base* (VALD) (Kupka et al., 2000; Piskunov et al., 1995). For compiling a usable iron line list, all theoretical transitions in a given wavelength range are requested from VALD. In the near-infrared (NIR), YJHK bands, there are several thousands of theoretical transitions.

In this thesis the EWs are measured (see Section 3.3.2) for all these lines using a solar spectrum (Hinkle et al., 1995b, is used here). Here there are four possible outcomes. 1) A line can not be measured and is thus discarded, 2) the EW of the line is weak (below 5 mÅ) to be reliable, 3) the EW of the line is too strong (above 150 mÅ) and the line show non-linear behaviour in the curve-of-growth (see Figure 2.5), or 4) the EW of the line is between the two limits and is then added to the final line list.

After removing lines which EW is outside the range of EW mentioned above, it is good practise to have a visual inspection. Here one should look for severe line blending with other absorption lines which might prove problematic and unreliable measurements of the EW. If the reference spectrum used, here for the Sun, is not corrected for telluric lines, it is also a good idea to remove lines which exists amidst forest of telluric lines, as these absorption lines might fall on the telluric lines, if the star observed has a different radial velocity (RV).

When blended lines and otherwise lines which shows strange features (can be in a forest of telluric lines), the last step is to calibrate the atomic data. As mentioned above, this is done by changing the log gf value for a given line, until it has the desired determined abundance. In this case, an iron line should have the abundance of 7.47 using the values from Gonzalez and Laws (2000), when using a solar atmosphere model. There is a simple anti-correlation between the determined abundance from the measured EW and the log gf, so a simple bisector minimization can be used to find the best log gf. It is important to calibrate the log gf when changing the version of `MOOG` (or if other radiative transfer codes are used), the atmosphere model and version of those, and even the interpolation of the atmosphere models. These changes in log gf should be minor compared to the change from the VALD database and those we arrive at when calibrated for the Sun.

2.4 Spectrographs

This chapter will be focused on some of the available spectrographs for deriving stellar atmospheric parameters using the method described in Section 3.3. For this we need a spectrum of both high resolution and high signal-to-noise ratio, S/N, which combined will be called a high quality spectrum. In order to get reliable results, a spectral resolution of at least $R = \frac{\lambda}{\Delta\lambda} = 25\,000$ is needed. A $S/N \approx 100$ is at least needed to obtain the parameters. These are approximately values since it can vary across different spectral classes, e.g. it is often relatively easy to obtain parameters of a solar-twin while it gets increasingly difficult as especially T_{eff} diverges in either direction from the solar value. Naturally the higher quality the spectrum is (both resolution and S/N), the better the results will be obtained. It is common practise to increase the S/N for a spectrum by co-adding a sample of lower S/N spectra of the same star from the same spectrograph. This is often used if the star of interest is so dim that it takes several observations to reach a sufficient high S/N. Another case is when spectra have been obtained from the archive. The scientific goal can be very different, e.g. obtaining radial velocities (RV) where a much

lower S/N is needed, however here numerous spectra are needed. It is common to search for exoplanets with the RV detection method, where multiple spectra are obtained, and the stellar parameters are then obtained after co-adding the multiple spectra. It is of course important to put the spectra on a common RV, usually at $0 \, \text{km/s}$.

Spectrographs work in different wavelength regions. The most used region is the optical part of the spectrum, which is also ideal for studying FGK stars with relative low line blending and low telluric contamination. In the recent years there has been an increase of NIR spectrographs. These will mainly be used to study the distant Universe, i.e. at high red-shifts, and cool objects in our own galaxy. Especially interesting are the M stars which consist of around 70% of all stars in our galaxy (Bochanski et al., 2010). These stars are intrinsic dim because of their low T_{eff}, ranging from $2200 \, \text{K}$ to $3500 \, \text{K}$, hence most of their light emitted will be in the NIR. It is advantageous to collect as much light as possible from these dim stars, since reaching a similar S/N in the optical would be more time expensive. The cool M stars have more molecules in the atmosphere than their hotter counterparts. This can be seen in the spectrum, where molecular lines greatly depress the continuum, making EW measurements difficult. This continuum depression is much larger in the optical than the NIR, giving another motivation for studying stars in this wavelength region.

Chapter 3

Deriving stellar parameters

There are different methods for obtaining stellar atmospheric parameters. Here follows a short description of some of the most common methods, however the spectroscopic method will be explained in much greater detail later in this chapter.

3.1 Photometry

Photometry can be used in different ways to estimate the effective temperature. In this section two methods will be mentioned; a colour calibration, and asteroseismology. There are other methods, e.g. SED fitting but this will not be discussed further.

3.1.1 InfraRed Flux Method - IRFM

The InfraRed Flux Method (IRFM) was first described by Blackwell and Shallis (1977). From IRFM it is possible to measure the stellar radius and T_{eff} with a measurement of the angular diameter, θ, derived from infrared photometry. T_{eff} is derived from the angular diameter from the simple relation

$$\sigma T_{\text{eff}}^4 = \frac{4\mathcal{F}_E}{\theta^2}, \tag{3.1}$$

where $\mathcal{F}_E$ is the monochromatic flux measured at Earth, and σ is Boltzmann's constant. The angular diameter is calculated from the following equation:

$$\theta = 2\sqrt{\mathcal{F}_E/\mathcal{F}_S}, \tag{3.2}$$

where $\mathcal{F}_S$ is the calculated monochromatic flux from the star. This flux is based on a model atmosphere with an effective temperature based on the spectral energy distribution (SED). The calculated flux show a strong dependence on T_{eff} in the visible, however this dependence is much weaker in the infrared. Hence a poor first estimation of T_{eff} will lead to a reliable angular diameter. From this new angular diameter T_{eff} can be re-derived, a new model atmosphere can be used with a new set of $\mathcal{F}_S$ can be calculated. Iteratively the angular diameter and T_{eff} can be calculated. If the distance d is known of the star, the stellar radius is $R_* = \frac{\theta d}{2}$. The solar flux, both measured and calculated, from Blackwell and Shallis (1977) are shown in Figure 3.1. Using the data provided the solar radius and T_{eff} were derived using the

equations above: $R = 1.011 R_\odot$ and $T_{\rm eff} = 5963$ K. This was simply done for each wavelength, and the results presented here are just a simple average value.
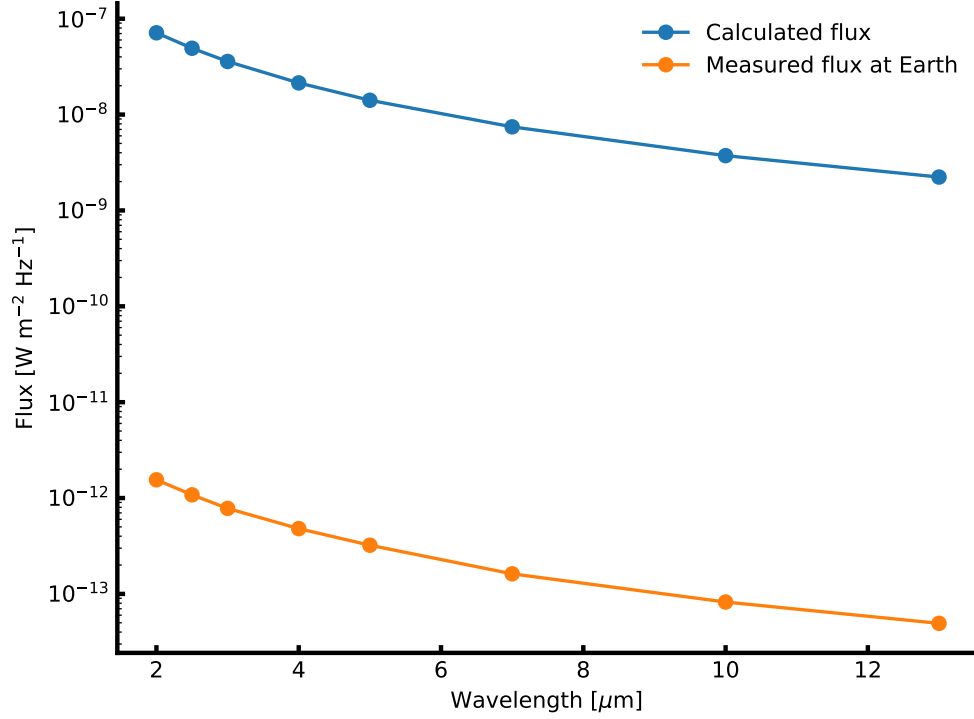
Figure 3.1: Measured and calculated flux from the Sun at infrared wavelengths. Data from Table 2 in Blackwell and Shallis (1977). Mean solar radius from this data is $1.011 R_\odot$, and mean solar $T_{\rm eff} = 5963$ K using Equation 3.1.

The main drawbacks of the IRFM is the model dependence, a drawback many methods share, and the need of high precision infrared photometry. For the model atmosphere a metallicity and surface gravity is assumed which has an effect on $\mathcal{F}_S$, and hence on the final derived $T_{\rm eff}$ and R. A more in-depth description of the IRFM can be see in e.g. Casagrande et al. (2006, section 4).

3.1.2 $T_{\rm eff}$-colour-[Fe/H] calibration

Photometry can be used for deriving $T_{\rm eff}$ using existing colour calibrations like that of for example Ramírez and Meléndez (2005) where adopted $T_{\rm eff}$ and [Fe/H] in combination with colours such as $B - V$, $V - S$, etc. are used to fit a polynomial such that the $T_{\rm eff}$ can easily be estimated with a simple relation:

$$T_{\rm eff} = \frac{5040}{\theta_{\rm eff}} + P(X, [{\rm Fe/H}]), \tag{3.3}$$

where

$$\theta_{\rm eff} = \frac{5040}{T_{\rm eff}} \tag{3.4}$$

$$= a_0 + a_1 X + a_2 X^2 + a_3 X [{\rm Fe/H}] + a_4 [{\rm Fe/H}] + a_5 [{\rm Fe/H}]^2 \tag{3.5}$$

is the polynomial fit between T_{eff} versus a colour (X) and the metallicity. The polynomial $P(X, [\text{Fe}/\text{H}])$ is a correction applied to remove trends in the residuals, for example spectral features such as the Balmer lines or the Paschen jump. This correction is performed after the initial fit.

After obtaining the coefficients (a_i) for different combinations of colours, it is trivial to obtain T_{eff} if the metallicity and a colour is known of the star.

3.1.3 Asteroseismology

Asteroseismology is the study of stellar pulsations. These pulsations propagate as sounds waves throughout a star, their origin and amplitude is determined by the characteristics of the star, hence the study of the pulsations, which are seen on the surface, will thus be a study of the stellar properties. In order to to study these a time series is needed. This can both be radial velocities as it was used in the recent results from the SONG telescope (Grundahl et al., 2017), or photometry like the numerous results from e.g. the space telescopes *CoRoT* and *Kepler* (see e.g. Chaplin et al., 2011; Christensen-Dalsgaard et al., 2010; Huber et al., 2014). The analysis is identical for either time series, however the amplitudes in the power spectrum will look different.

After determining the frequencies of a range of pulsations from a power spectrum of the time series, a pattern emerge at every $\Delta\nu$ (the so-called large frequency separation). A finer pattern also occur described by $\delta\nu$. Last the frequency at maximum power is also measured from the power spectrum, ν_{max}. These frequency separations are used to obtain $\log g$ via

$$\nu_{\text{max}} \propto \frac{g}{\sqrt{T_{\text{eff}}}} \tag{3.6}$$

$$= \frac{M/M_\odot}{(R/R_\odot)^2 \sqrt{T_{\text{eff}}/5777}} \, 3.05 \, \text{mHz}, \tag{3.7}$$

where $\nu_{\text{max},\odot} = 3.05 \, \text{mHz}$ is the frequency of maximum amplitude for the Sun. A similar equation exists for the determination of the stellar density:

$$\Delta\nu = (M/M_\odot)^{-1/2}(R/R_\odot)^{-3/2} \, 134.9 \, \mu\text{Hz}. \tag{3.8}$$

These simple scaling relation are described in detail in Kjeldsen and Bedding (1995). These two equations can be used together to determine the mass and radius of the star, often to a high precision. These scaling relations are applicable for stars which shows solar-like oscillations, mostly found in main sequence FGK stars, but can also be found in red giant stars. The mass and radius for a range of ν_{max} and $\Delta\nu$ can be seen in Figure 3.2, where $T_{\text{eff}} = 5777 \, \text{K}$. The star located at $\{\Delta\nu = 134.9 \, \mu\text{Hz}; \, \nu_{\text{max}} = 3.05 \, \text{mHz}\}$ is the Sun.

The small frequency separation, $\delta\nu$, is sensitive to the sound-speed gradient in the core which in turn is sensitive to the composition. Thus the small frequency separation is a very important diagnostic for stellar evolution. An interesting case is that of Bedding et al. (2011), where it was shown it is possible to distinguish between hydrogen- and helium-burning cores in red giant stars.

A drawback of asteroseismology is the dependence of T_{eff} in Equation 3.7 which has to be provided from another method. Ideally this will come from spectroscopy for which the determination of T_{eff} is often reliable. This drawback is minor compared to the lack of model dependence which is one of the strongest advantages of asteroseismology.
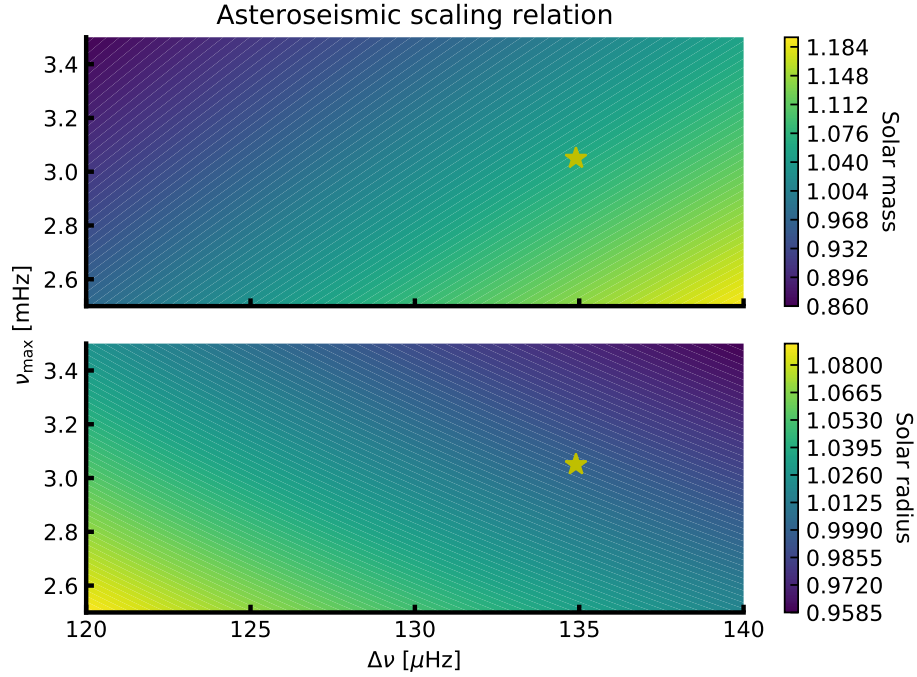
Figure 3.2: Mass and radius from asteroseismic scaling relation. The colour is the mass and radius for the upper and lower panel, respectively.

For both of the mentioned photometric methods to determine some atmospheric parameters a disadvantage is the dependence on the knowledge of other atmospheric parameters which usually comes from spectroscopy (e.g. metallicity). However, as will be discussed in Section 3.2 $\log g$ is often difficult to determine reliably and synergies are welcomed between different methods.

3.2 Spectroscopy

A spectrum can be analysed with a range of different methods. The method finally chosen depend on quality of the spectrum, i.e. high/low resolution and high/low S/N, the spectral type of the star, the region that was observed, e.g. UV, optical, NIR, etc., some stellar properties, e.g. fast-rotator, activity, etc. No methods work for all cases, but sometime several methods can be used for on case.

Since this thesis is focused on FGKM stars, and mainly dwarfs, three methods will be described; synthesis, spectral indices, and the EW method. The latter method will be described in a separate section since this is the main method used for the analysis in this thesis.

3.2.1 Synthesis

The synthesis fitting method is a standard method for obtaining stellar atmospheric parameters from a wide range of spectra, that is with different spectral resolution, spectral parameters such as $T_{\rm eff}$, $\log g$, $v \sin i$ the projected rotational velocity, etc., and S/N (see e.g. Tsantaki et al., 2017). The synthetic fitting method is in simple terms a comparison between the observed spectrum and a synthetic spectrum,

which is either calculated on the fly like Spectroscopy Made Easy (SME) (Valenti and Piskunov, 1996), or using a pre-calculated grid like Starfish (Czekala et al., 2015). By analysing the

$$\chi^2 = \sum_i^N \frac{(y_{\mathrm{obs,i}} - y_{\mathrm{model,i}})^2}{\sigma_i},$$
(3.9)

the synthetic spectrum that best match the observed spectrum can be found. Here the y_{obs} is the observed spectrum, y_{model} is the synthetic spectrum, and σ is the error on the measurement.

The synthetic fitting can be done by utilising small windows around sensitive spectral features such as ionized lines or hydrogen lines for obtaining the surface gravity, iron lines for obtaining the effective temperature, a series of different atomic lines for obtaining the overall metallicity. This approach is used by FASMA and SME (Tsantaki et al., 2017; Valenti and Piskunov, 1996, respectively) and is a compromise between fitting the entire spectral range and calculating the synthetic spectra on the fly which is time consuming. On the other hand the entire spectrum can be fitted if a pre-calculated grid of synthetic spectra are available. By masking small windows, one can also exclude different features that are troublesome, this can be telluric lines, bad reduction of the spectra, or real spectral features where there currently is poor atomic/molecular data such as the oscillator strength and thus it is not possible to reliably fit this feature.

This method is affected by the different approaches one can use, that is which atmosphere models are used (ATLAS, MARCS, etc.), atomic data and whether this has been calibrated, the radiative transfer code in the case the synthetic spectra are calculated on the fly, and the minimization procedure chosen. With these things in mind it is important to stress the wide range spectra and spectral classes this method works with.

3.3   FASMA

The EW method or curve-of-growth analysis is another standard method for obtaining stellar atmospheric parameters from spectra as the synthetic fitting method (Section 3.2.1). Since this is the method used throughout this thesis it will be explained in detail. This analysis follow a chain of tasks, each has been made automatic in the software Fast Analysis of Spectra Made Automatically (`FASMA`[1]) which was developed during this thesis (Andreasen et al., 2017b). `FASMA` is made of three `drivers`:

1. EW measurement driver

2. Obtain stellar atmospheric parameters driver

3. Abundance driver

An additional driver is under development; a synthetic fitting driver (Tsantaki et al., 2017). `FASMA` has been made available to the community via a web application at http://www.iastro.pt/fasma/.

3.3.1   Ingredients

`FASMA` is written in the Python programming language and glue together other software and model atmospheres necessary for obtaining stellar atmospheric parameters from high quality spectra. These

---

[1]   Greek for spectrum

software and models are described in greater detail in the following sections. In short, the curve-of-growth analysis require measured EWs where the latest version[2] of `ARES` is used (Sousa et al., 2015). These EWs are used to derive line abundances using model atmosphere like the ATLAS9 (Kurucz, 1993), MARCS models (Gustafsson et al., 2008), or PHOENIX models (Husser et al., 2013) to mention the most popular for this analysis. Note that the PHOENIX models are relative new and not as widely used yet. In tandem with model atmospheres a radiative transfer code is also needed. `FASMA` uses `MOOG` (Sneden, 1973) for this. The model atmosphere usually comes in a pre-calculated grid in the $\{T_{\mathrm{eff}}, \log g, [\mathrm{Fe}/\mathrm{H}]\}$ parameter space. These are interpolated in order to access the requested combination of parameters. Last, `FASMA` consist of a minimization routine which looks for the best matching parameters given a spectrum.

3.3.2 Wrapper for `ARES`

There are two ways to measure the EW of an absorption line, manually or automatically. There are advantages and disadvantages for both method. For the manual, an advantage is that we can inspect the lines and try to measure lines in different ways (which is useful if it is blended). We have more control over how blended lines are fitted, and which profiles are used. Disadvantages are that it is very time consuming, and it is prone to errors, as a measurement might change drastically by the eyes measuring it. Even for the same person, the measurement can change. By mentioning the advantages and disadvantages of the manual method, it should be clear that the advantages and disadvantages of the automatic method is the opposite of those. Especially the time to measure the lines are orders of magnitudes faster, which is crucial when dealing with more than a handful of spectra.

When a line is measurement by hand (manually) it is in this thesis done using the `splot` command in `IRAF`. Here the deblending mode is used whenever necessary. It is often necessary to fit one spectral lines with several Gaussians, as neighbouring lines might contaminate the line of interest.

When a line is measurement automatically it is in this thesis done with `ARES` (Sousa et al., 2015, 2007). When using `ARES` it is important to use a correct value of the `rejt` parameter. This parameter is used for placing the continuum level, and is thus directly related to the final measurement EW. It is difficult to get this parameter right, however the newest version of `ARES` has the option to analyse a few absorption free regions and measure the S/N. The `rejt` is then calculated as:

$$\texttt{rejt} = 1 - \frac{1}{\mathrm{S/N}}.$$

`ARES` is used via the first driver of `FASMA`. All the options available for `ARES` can be accessed by `FASMA`. The options are

- Setting the spectral window, λ_{min} and λ_{max}

- RV correction to be applied or a mask to measure the RV and automatic make this correction

- minimum and maximum EW to be considered ($5\,\mathrm{m\AA}$ and $150\,\mathrm{m\AA}$ respectively by default)

- Minimum distance between two consecutive lines

- Smoothing applied with a `boxcar` filter before measuring the EWs

---

[2]   The latest version can be found here: https://github.com/sousasag/ARES

An in-depth description of these options can be found in Sousa et al. (2015, 2007).

Sometimes ARES crash when measuring an absorption line. The reason is not clear, however when dealing with a large amount of spectra, it is important that the analysis moves on. To deal with this problem, FASMA finds the last line which ARES tried to measure in the log file. This line is temporarily removed from the line list and ARES is restarted. The line list used for deriving parameters consists of numerous iron lines, thus removing one line will have a negligible effect on the final derived parameters.

3.3.3   Interpolation of atmosphere models

FASMA has access to both ATLAS9 models by Kurucz (1993) and MARCS models by Gustafsson et al. (2008), both are in a pre-calculated grid as described above. Let this grid be described by $\{T_{\mathrm{eff,g}}, \log g_g, [\mathrm{Fe/H}]_g\}$, where subscript g is one of the grid points. Such a grid can be seen in Figure 3.3 for $[\mathrm{Fe/H}] = 0.00$ in the T_{eff} range; $3000\,\mathrm{K}\,to\,10\,000\,\mathrm{K}$. For visualisation the location of the Sun is shown as well. The colour scale corresponds to the temperature in the first layer of each model atmosphere, i.e. the uppermost layer. The requested value will be $\{T_{\mathrm{eff,r}}, \log g_r, [\mathrm{Fe/H}]_r\}$. The task is now to find the surrounding grid points in the parameter space of the requested parameters. For $\log g$ and $[\mathrm{Fe/H}]$ two neighbouring grid point are used, and for T_{eff} four surrounding grid point are used, in total $4 \times 2 \times 2 = 16$ model atmospheres for the interpolation. FASMA use the four surrounding grid points for T_{eff} instead of two, since the model atmosphere changes most with T_{eff}. This is common in other interpolations as well (see e.g. Valenti and Piskunov, 1996).
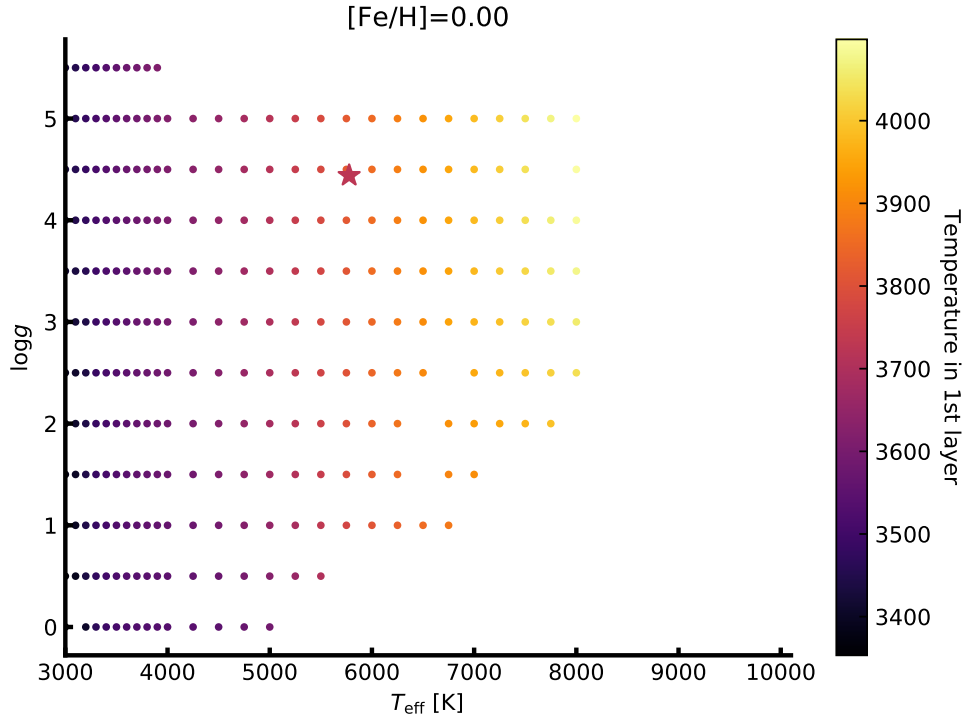
Figure 3.3: Model atmosphere grid from Kurucz (1993) at $[\mathrm{Fe/H}] = 0.00$ between $3000\,\mathrm{K}$ and $10\,000\,\mathrm{K}$. The grid extends to higher T_{eff}, but these are not considered in this thesis.

When the 16 model atmosphere have been located, the interpolation goes through each layer of the

model atmosphere, where there typical are 72 layers, and each column of which there are six. The columns are described in Section 2.2.1. The interpolation are done using the `griddata` function from `SciPy`[3]. The interpolation is linear in the parameter space. After the interpolation, the result is saved to a file in the format expected by `MOOG`.

3.3.4   Minimization

With the measured EWs for all the lines in the line list, we choose an atmosphere model to determine the abundances. If there is no prior knowledge of the star it is common simply to choose an atmosphere model with solar parameters as a starting point. Once the line abundances of all the iron lines has been determined, the linear correlation between the abundances and the reduced EWs (RW), and the abundances and the excitation potential is calculated. If there is a correlation it means the model atmosphere used is wrong. Moreover, we also have to check if the mean abundance of Fe I and Fe II lines are equal, and last if mean abundance of the Fe I lines is equal to the input [M /H] of the atmosphere model[4]. If one of these four criteria does not pass, then the atmosphere model is wrong, and we have to search for a new one. A common way to do this, is by combining the indicators into a scalar value:

$$f(\{T_{\text{eff}}, \log g, [Fe/H], \xi_{\text{micro}}\}) = \sqrt{a_{\text{EP}}^2 + a_{\text{RW}}^2 + \Delta\text{Fe}^2}, \tag{3.10}$$

where a_{EP} is the correlation between abundances and excitation potential, a_{RW} is the correlation between abundances and RW, and ΔFe is the difference between the mean abundances of Fe I and Fe II. This scalar function can be minimized using standard minimization procedures as the simplex downhill among others. However, there is another approach that takes into the account the information stored in these indicators. For example, if a_{EP} is positive it means T_{eff} has to be increased by an amount correlated by the numerical value of a_{EP}. In the same way, a non-zero a_{RW} means ξ_{micro} has to be changed, and ΔFe is an indicator for $\log g$. In the end it is a vector function being minimized which are more difficult, however we are not minimizing this using standard mathematical methods, but rather using the physical knowledge. This minimization is useless for anything else, but it is excellent for this. The vector function has the form:

$$f(\{T_{\text{eff}}, \log g, [Fe/H], \xi_{\text{micro}}\}) = \{a_{\text{EP}}, a_{\text{RW}}, \Delta\text{Fe}, \text{Fe I}\}. \tag{3.11}$$

The abundances of Fe I lines versus EP and RW are shown in Figure 3.4 for the planet host star HATS-1. The three rows are for three different model atmospheres. From upper to lower:

- Converged: $T_{\text{eff}} = 5959$ K, $\log g = 4.59$, [Fe /H] $= -0.04$, and $\xi_{\text{micro}} = 1.05$ km/s.

- Converged with 0.5 km/s added to ξ_{micro}.

- Converged with 500 K added to T_{eff}.

Left column show the abundances against the EP, and the right column is abundances against RW.

The minimization with the different options is depicted in Figure 3.5. In each iteration where convergence is not reached, the input metallicity is changed to that of the average output metallicity

---

3   https://scipy.org/
4   We use Fe I instead of Fe II lines for this, since they are more numerous.
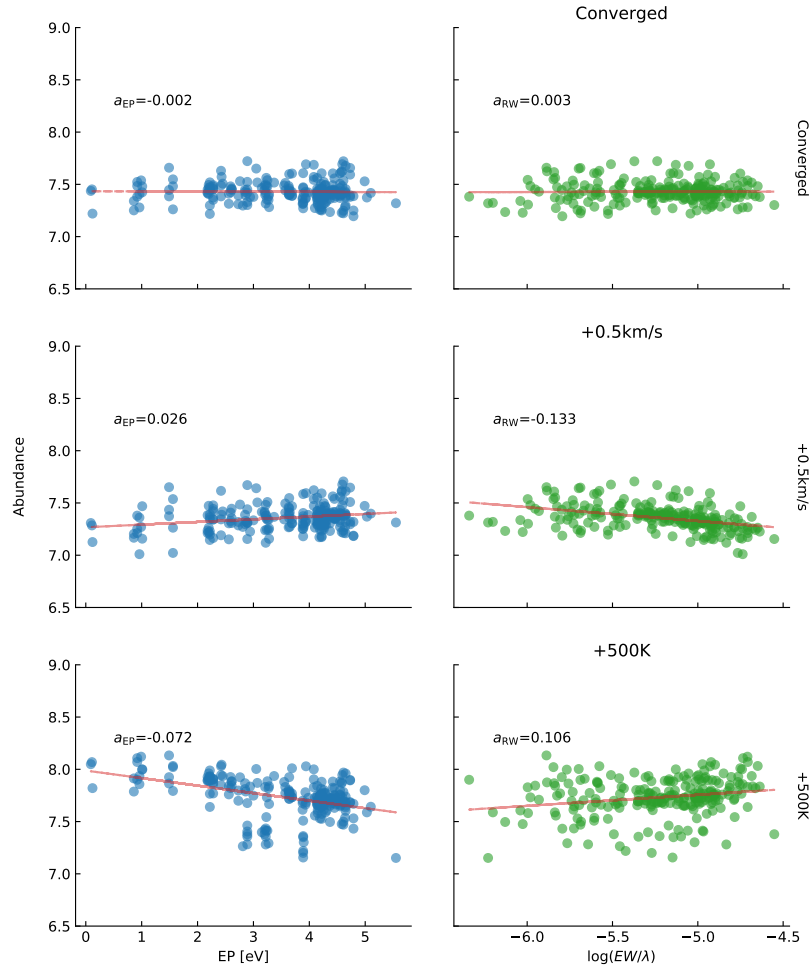
Figure 3.4: The abundances of Fe I for the planet host star: HATS-1. Upper plot: Converged parameters (see text for stellar parameters for this star). Middle plot: Converged parameters with $0.5\,\mathrm{km/s}$ added to ξ_{micro}. Lower plot: Converged parameters with $500\,\mathrm{K}$ added to T_{eff}.

using the Fe I lines. `FASMA` is able to fix one or all of the four atmospheric parameters, and when it reach convergence it checks if there are any outliers in the abundances. These will be removed, either:

- All outliers above 3σ once; minimization routine is restarted after removal of outliers.

- All outliers above 3σ iteratively; minimization routine is restarted after removal of outliers each time.

- One outlier above 3σ (with the highest deviation) is removed iteratively; minimization routine is restarted after removal of outliers each time.

All restarts of the minimization will start at the precious best found parameters. For the latter two were outliers are removed iteratively, this will continue until no outliers are present. An optical line list like the ones by Sousa et al. (2008); Tsantaki et al. (2013) have been tested thoroughly and it is safe to remove a larger amount of lines and still obtain reliable parameters, thus using the first option is common here. However, with a less tested line list, like the one by Andreasen et al. (2016) (and refined in Andreasen et al. (2017a)), one should remove outliers more carefully, and it is recommended that one outlier is removed iteratively.

Sometimes the minimization can not reach convergence with all parameters free. The first approach to progress is to fix ξ_{micro} to a value. This parameter is known to depend on the spectral type (see e.g. Tsantaki et al., 2013, and references therein). `FASMA` use one of two empirical relations to fix ξ_{micro} if this is close to either 0km/s or 5km/s and $|a_{\mathrm{RW}}| > 0.050$ at the end of the minimization. The empirical relations are:

$$vt = \begin{cases} 6.935 \cdot 10^{-4}\, T_{\mathrm{teff}} - 0.348 \log g - 1.437 & \text{For } \log g \geq 3.95 \\ 2.72 - 0.457 \log g + 0.072 \cdot [\mathrm{Fe\,/H}\,] & \text{For } \log g < 3.95, \end{cases} \tag{3.12}$$

where the first case is from Tsantaki et al. (2013) and the latter case is from Adibekyan et al. (2015). In this way ξ_{micro} is changed in each iteration according to one of these relations. This option is called `autofixvt` in Figure 3.5.

Last there is an option, `refine`. This apply more strict criteria for the indicators to reach convergence, thus making the minimization less sensitive to the initial guess since it could otherwise reach convergence from one "side" of the parameter space. The default criteria are:

$$a_{\mathrm{EP}} = 0.001$$
$$a_{\mathrm{RW}} = 0.003$$
$$\Delta \mathrm{Fe} = 0.001.$$

The criteria for a_{RW} is not as strict as a_{EP} since this indicator can change rapidly with small changes in ξ_{micro}, thus a very strict criteria might never lead to convergence. Convergence is reached once all of the above criteria are met, and the input and output metallicity are identical. If one or more of the parameters are fixed, the corresponding criterion is simply set to 0 and effectively ignored, thus not changing the parameter.

For each iteration, the change to be applied for the atmospheric parameters are defined by adding the

following:

$$T_{\text{eff}} : 2000 \,\text{K} \cdot a_{\text{EP}} \tag{3.13}$$

$$\xi_{\text{micro}} : 1.5 \,\text{km/s} \cdot a_{\text{RW}} \tag{3.14}$$

$$\log g : -\Delta\text{Fe} \tag{3.15}$$

to each parameter. Note again that metallicity is simply changed to the the output metallicity of the previous iteration. These are empirical relations. Note that by changing e.g. T_{eff} not only is a_{EP} affected, but the other indicators as well as seen in Figure 3.4. This inter-dependency between the parameters is ignored by `FASMA` as it is not a simple problem to solve. The stepping presented above is chosen to rapidly reach convergence, without causing problems for the inter-dependency.
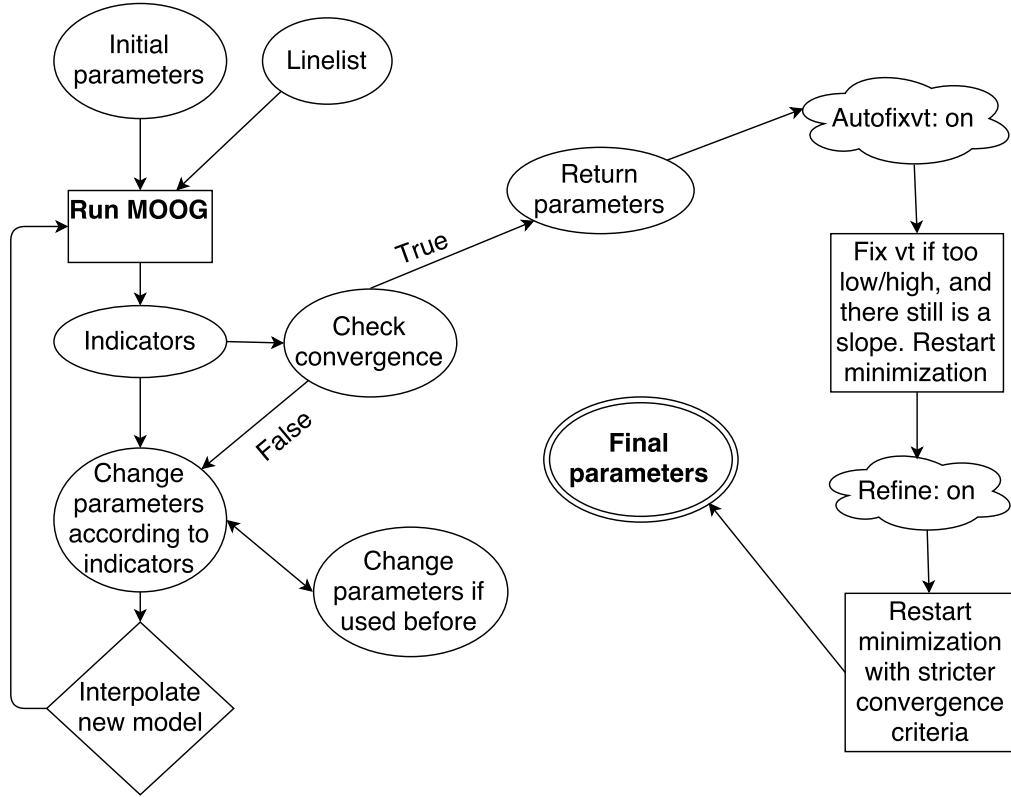
Figure 3.5: Overview of the minimization for `FASMA`. Credit: Andreasen et al. (2017b).

3.3.5 Error estimate

The error estimate is based on the same method presented in Neuforge-Verheecke and Magain (1997). The error on ξ_{micro} corresponds to the 1σ statistical error on the slope of the linear regression between Fe I abundances and RW. The error on T_{eff} is the statistical error on the slope between Fe I abundances and EP as well as the uncertainty in ξ_{micro}. The error for [Fe /H] corresponds to the dispersion of the Fe I abundances as well as the uncertainties in ξ_{micro} and T_{eff}. The error in $\log g$ corresponds to the dispersion in the pressure sensitive Fe II abundances.

Chapter 4

Results for FGK stars

> Don't cry because it's over, smile because it happened.
>
> Dr. Seuss

It is time to apply the theory and methodology on some real data. There is the compilation of a NIR iron line list for deriving stellar atmospheric parameters. This line list was tested against the well-studied solar-type star, HD 20010 in Andreasen et al. (2016). Later a second version of the line list was made. This was tested again on HD 20010 and additionally on two colder stars, Arcturus and 10 Leo in Andreasen et al. (2017a). A small summary of the stars and their characteristics can be found in Table 4.1. More details are provided in the individual sections below for each star. An update to SWEET-Cat (Santos et al., 2013), a catalogue which provides homogeneous stellar parameters of planet hosts, was provided in Andreasen et al. (2017b). Additionally in this work, there was an analysis of how a selection of lines with different excitation potential might affect the final parameters of a star, which is discussed in Section 4.8. Last is the analysis of a range of synthetic spectra from the PHOENIX spectral library (Husser et al., 2013), with T_eff lower than analysed in previous stars with the methodology described above in Section 3.3. However, before diving into the results of the analysis it is important to describe how the NIR line list was compiled, and why and how it was later refined.

Table 4.1: Summary of the four stars used in this thesis. The stellar parameters are an average from the PASTEL catalogue (Soubiran et al., 2016) (see text for details), except the parameters for the Sun.

Star	Spectrographs	Resolution	T_eff (K)	$\log g$ (dex)	ξ_micro (km/s)	[Fe/H] (dex)
Sun	FTS	600 000	5777	4.44	1.00	0.00
Arcturus	FTS	100 000	4300 ± 111	1.60 ± 0.29	1.93 ± 0.17	-0.54 ± 0.11
HD 20010	CRIRES	100 000	6152 ± 95	3.96 ± 0.11	1.17 ± 0.24	-0.27 ± 0.06
10 Leo	CRIRES	100 000	4742 ± 61	2.76 ± 0.17	1.45 ± 0.08	-0.03 ± 0.02

4.1 The creation of a NIR line list

Although previous work have compiled some NIR line lists for different purposes, there still does not exists an iron line list to determine stellar atmospheric parameters from high S/N and high resolution

which work exactly? See recent paper

spectra. With the advancement of NIR high resolution spectrographs the time has arrived to compile such a line list, which should be properly tested (used to determine parameters of well known stars).

As discussed extensively in Chapter 2 and Chapter 3, an atomic line list is needed for employing the method of deriving the stellar atmospheric parameters used in this thesis. This line list is composed by neutral and ionized iron lines in the NIR. This has already been mentioned in Chapter 2. Here the process will be explained in greater detail below for the two versions presented in Andreasen et al. (2016) and Andreasen et al. (2017a), respectively.

4.1.1 Measuring the EWs and first filtering

The first version of a NIR iron line list for determining stellar atmospheric parameters of high resolution and high S/N spectra were presented in Andreasen et al. (2016). Other NIR line lists exists such as the one from Lindgren et al. (2016); Önehag et al. (2012) for utilising the synthetic method described above of high resolution spectra. Their line list cover the J band in the NIR and consists of 48 lines of different elements.. For this line list all iron transitions between $10\,000\,\text{Å}$ to $25\,000\,\text{Å}$[1] were downloaded from the VALD database (Kupka et al., 2000; Piskunov et al., 1995), only including Fe I and Fe II transitions. In total were $50\,198$ Fe I and $28\,339$ Fe II lines respectively acquired.

The EW of all lines were measured in the solar atlas by Hinkle et al. (1995b). The EWs were measured using `ARES` due to the large amount of lines and to be as consistent as possible in the measurements. Since `ARES` expect a 1D spectrum with equidistant wavelength step, the solar spectrum was interpolated onto a regular wavelength grid of $0.01\,\text{Å}$. This did not change the appearance, and hence not the EW, of the final spectrum. This wavelength step is equivalent to a spectral resolution of $1\,500\,000$ at $15\,000\,\text{Å}$. The S/N for the solar atlas varies between 300 to 2000 across the spectrum, but is generally of a very high quality.

The EWs were measured by fitting Gaussian profiles to the spectral lines. For a given line, `ARES` output the central wavelength of the line (provided in the line list), the FWHM maximum of the fitted line, the number of lines fitted for the final result (in case of blending), the depth of the line, and the EW of the line of the line. In the latest version of `ARES`, the error of the EW is also provided (Sousa et al., 2015).

As a first selection step, lines were discarded according to the following four criteria:

- Lines with EW lower than $5\,\text{mÅ}$: these lines can be problematic to see in spectra with lower S/N or spectra with many spectral features. Therefore the measurements of these lines are less reliable than stronger lines.

- Lines with EW higher than $200\,\text{mÅ}$: These lines are too strong to be fitted with a Gaussian profile. These lines might also be saturated and do not fall in the linear regime of the curve-of-growth (see Figure 2.5).

- Lines where the total number of fitted lines are 10 or higher meaning the presence of severe blending.

- If the fitted central wavelength is more than $0.05\,\text{Å}$ away from the wavelength provided by VALD3 to avoid false identification. This should also remove some blended lines.

---

[1]   That is equivalent to the YJHK bands.

- Removal of lines with EP higher than $5.5\,\mathrm{eV}$. This cut was inspired by available EPs in the optical (see e.g. Sousa et al., 2008).

After this removal the number of Fe I and Fe II lines were reduced to 6060 and 2735, respectively.

4.1.2   Visual removal of lines

At this point a visual inspection was necessary. All atomic data for possible transitions from all elements were downloaded from the VALD3 database in a $3\,\mathrm{\AA}$ window around each of the nearly 9000 iron lines from the previous step. For each small spectral window, all absorption lines (including the iron line(s)) were located in a plot of the solar spectrum. An iron line was discarded if another line had the same central wavelength and/or the absorption line were severely blended. Most of the discarded iron lines had high EP, which are weak compared to the low EP lines. Therefore, it is fair to assume that many of these iron lines were falsely identified as another stronger line from another element. After the visual removal the number of Fe I and Fe II lines were reduced to a mere 593 and 22, respectively. In Figure 4.1 is a case where too many lines are present near the iron line of interest (green line in the middle). The green lines are all iron lines in the spectral region, while the orange lines are other elements or molecules. The depth and transparency is a measure by the line strength given by

$$\text{strength} = \log \mathrm{gf} - \chi\Theta, \tag{4.1}$$

where $\Theta = 5040\,\mathrm{K}/T_{\mathrm{eff}}$ (solar temperature is used here). Note that this strength of the lines does not include any abundance information, and should therefore be a guide rather than an actual measure.

For some of the absorption lines it was not clear which element was causing it. These lines were marked for further investigation with synthesis as described below.

4.1.3   Synthetic investigation

For the lines marked above for further investigation an even broader window of $6\,\mathrm{\AA}$ was used. Once again, all atomic data for possible transitions were downloaded from the VALD3 database in these spectral windows. `MOOG` was used with the `synth` driver to create a synthetic spectrum using a solar atmosphere model with $T_{\mathrm{eff}} = 5777\,\mathrm{K}$, $\log g = 4.438$, $A(\mathrm{Fe}) = 7.47$, and $\xi_{\mathrm{micro}} = 1.00\,\mathrm{km/s}$. The iron abundance (7.47) is from Gonzalez and Laws (2000), while the overall metallicity for the solar atmosphere model is $[\mathrm{M\,/H}] = 0.00$ by definition. This step is different from the step visual inspection done in Section 4.1.2 since synthetic spectra were created here. This was done for all spectral windows for three different iron abundances $[\mathrm{Fe\,/H}] = \{-0.20;\ 0.00;\ 0.20\}$ in order to identify iron lines and their impact on the synthetic spectra. Before creating a synthetic spectrum all elements which are more than singly ionised were removed since `MOOG` does not allow these. An example of the three synthetic spectra can be seen in Figure 4.2. Here the neutral iron line at $15\,550.439\,\mathrm{\AA}$ was investigated. The three coloured curves are synthetic spectra with the three different $[\mathrm{Fe\,/H}]$. The upper plot shows the result with the full VALD3 line list, while in the lower plot the iron line was removed from the line list. The grey curve is the solar atlas for reference. Note that it is not the purpose to match a synthetic spectrum to the solar atlas.

If the synthetic spectra shows variation at the iron line of interest, then it is assumed that the iron line is the cause for the absorption line. As a simple test, the iron line was also removed from the line list used to create the synthetic spectra. If the iron line in the synthetic spectra disappeared, it was a clear

> Write about the synth driver and options used...
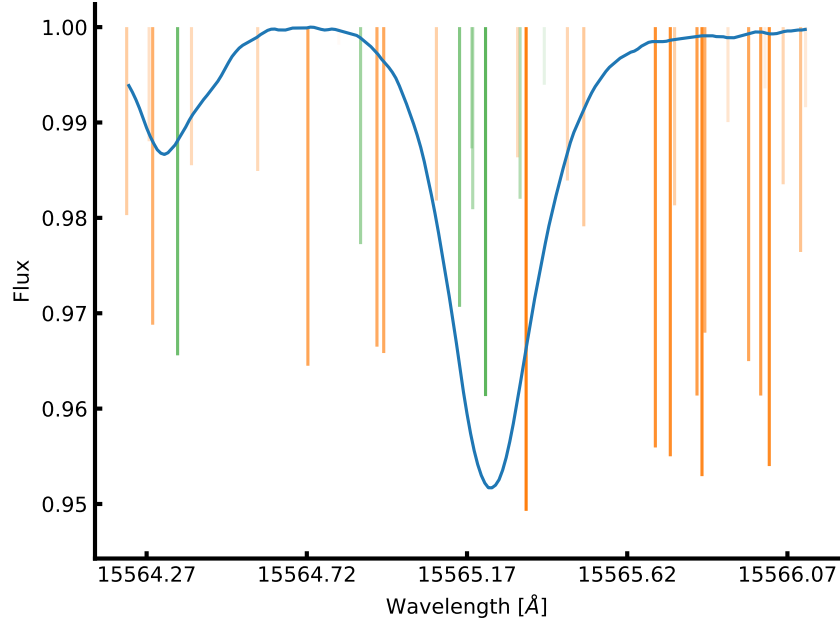
Figure 4.1: Solar spectrum (blue) with all iron lines in the spectral region (green) and other elements (orange). The depths and transparencies of the vertical lines are a measure of the line strengths (see Equation 4.1 for details). This is a case where the iron line is discarded due to blending, which is clear in the left wing of the central absorption line.
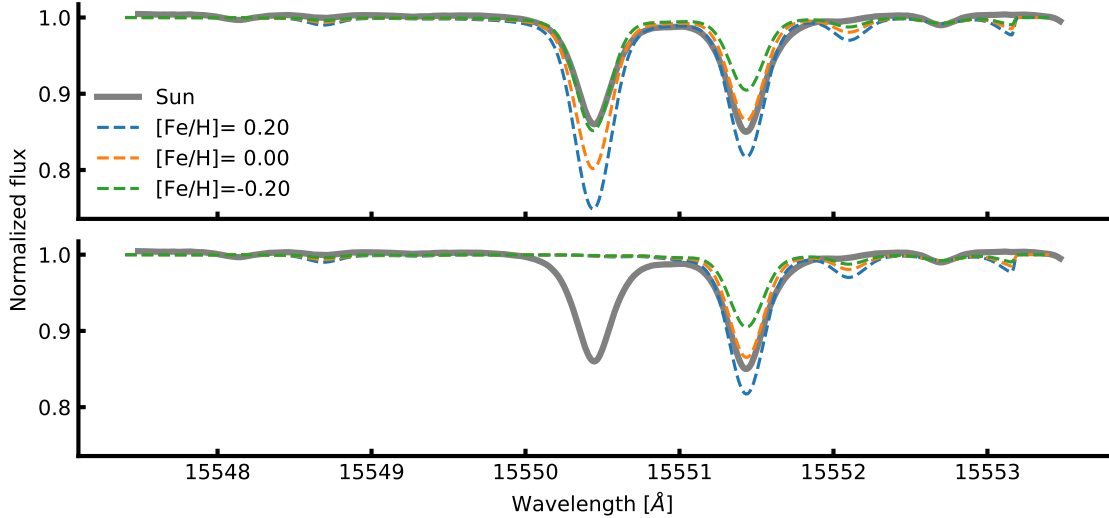
Figure 4.2: The three coloured curves represent different iron abundance, $\{-0.20; 0.00; 0.20\}$ compared to solar abundance. The grey curve is the solar atlas for reference. In this case the iron line at $15\,550.439$ Å was investigated. *Upper panel*: Synthetic spectra were computed using the full VALD line list in the spectral range for the three different iron abundances. *Lower panel*: Same as the upper panel, but with the iron line removed from the line list. Since the synthetic spectra shows no features at this absorption line anymore, it is a fair assumption to say the iron line is the cause of this absorption line.

signal that this line can be used in the final iron line list (this can be seen clearly in the lower plot of Figure 4.2). In some cases two iron lines had the same or very similar wavelength, and this technique was used to include the correct iron line. In cases where both iron lines causes the absorption line, they were both discarded since they are blended. In theory both iron lines will contribute to the absorption, however one of the contributions might be negligible, hence only one of the lines will be discarded.

In a few cases two iron lines had the same wavelength and EP but different $\log gf$. In these cases the two iron lines they can be combined into a single line by adding their gf values. After this step, there were 414 Fe I lines and 12 Fe II lines, respectively.

4.1.4 Calibrating the line list: astrophysical $\log gf$ values

These lines were collected into a single line list in the format required by MOOG (Sneden, 1973) and the line abundance were measured by all lines using the solar atmosphere model described above. If the derived abundance for a single line differs by more than 1.0 dex from the solar iron abundance, the line was discarded. All lines before this step can be seen in Figure 4.3 with all lines discarded marked in red.
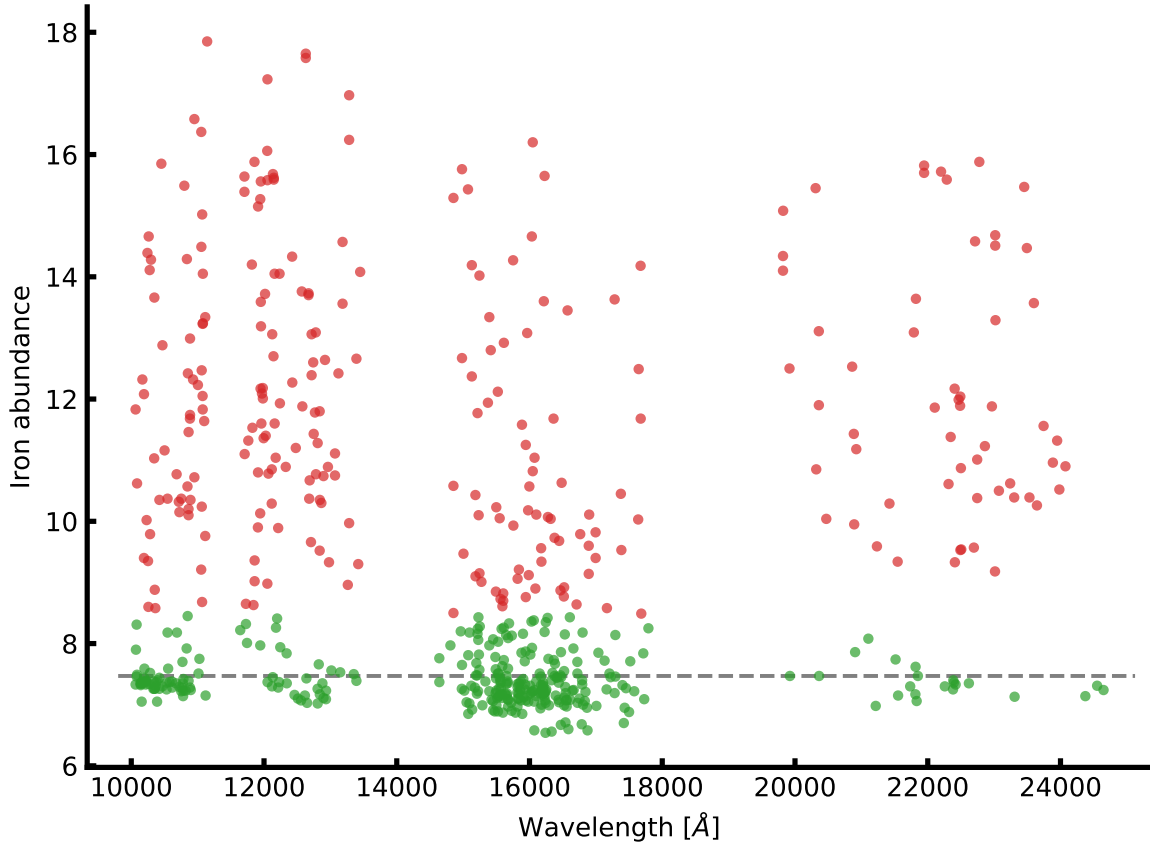
Figure 4.3: Line abundance of all iron lines before calibrating the $\log gf$ values. The green points are the points with a deviation less than 1.0 dex from the solar iron abundance. All the red points are discarded. The horizontal line shows the solar iron abundance.

After the removal of the lines mentioned above, the final line list is almost compiled. At this point the line list has to be calibrated. This is done by changing $\log gf$ so the line abundance for all iron lines

are 7.47 when using the solar atmosphere model mentioned above. As mentioned in Section 2.3 there is a anti-correlation between the abundance of a line and $\log gf$. This means a simple bisector minimization can be used to locate the $\log gf$ that gives the desired abundance. This was done for all the iron lines at this stage.

Note If the setup used to determine the parameters is changed, the it is important to calibrate the $\log gf$ values for the line list again. This includes the type of model atmospheres used (e.g. ATLAS9 or MARCS), the interpolation code to generate a model atmosphere from the grid, or the settings of the radiative code, here `MOOG`, and even the settings used in the radiative transfer code, i.e. the specific physics used. In the results listed below the setups are identical, except for the work done with synthetic spectra (see Section 4.7). There both ATLAS9 and MARCS model atmospheres were used, and a calibrated set of $\log gf$ values are available for both setups.

4.1.5 Removal of high dispersion lines

The line list calibrated above was used to derive parameters for HD 20010 (see Section 4.2), however the derived parameters showed poor results when compared to the literature values. This lead to the following test:

A Gaussian distribution was made for the EW of each line centred on the EW itself,

$$f(x, EW, \sigma) = \frac{1}{\sqrt{2\pi\sigma^2}} e^{-\frac{(x-EW)^2}{2\sigma^2}}, \tag{4.2}$$

where σ is the error on the EW, expressed by Cayrel (1988):

$$\sigma \simeq 1.6 \frac{\sqrt{\Delta\lambda EW}}{S/N}, \tag{4.3}$$

where $\Delta\lambda = 0.1$ and a S/N=50 were considered here, which is much lower than the actual S/N of the solar atlas. The search for lines to remove from the line list, in order to improve the results is as follows:

1. Make 100 draws for each EW (giving a total of 100 line lists)

2. Derive the line abundances for all 100 line lists using the solar model atmosphere and `MOOG`

3. Calculate the mean absolute deviation (MAD) for each line using the derived abundances

4. Locate the lines with highest dispersion in a MAD versus original EW plot (see Figure 4.4)

In the upper panel of Figure 4.4 the weaker lines (i.e. lines with lower EW) shows a higher MAD value, however this is expected since a small absolute change in the EW results in a large relative change in abundance for these lines. This does not mean these lines necessarily have a high dispersion, since it is just the expected outcome of this test. Moreover, these relatively weak lines from the solar atlas should be stronger for some other spectral types, and therefore important to include if possible. Therefore the disperse lines are found in the de-trended MAD value, where an exponential function was used for de-trending. A single point above 3σ was removed iteratively in the de-trended data. After this process there are 334 Fe I lines and 13 Fe II lines.
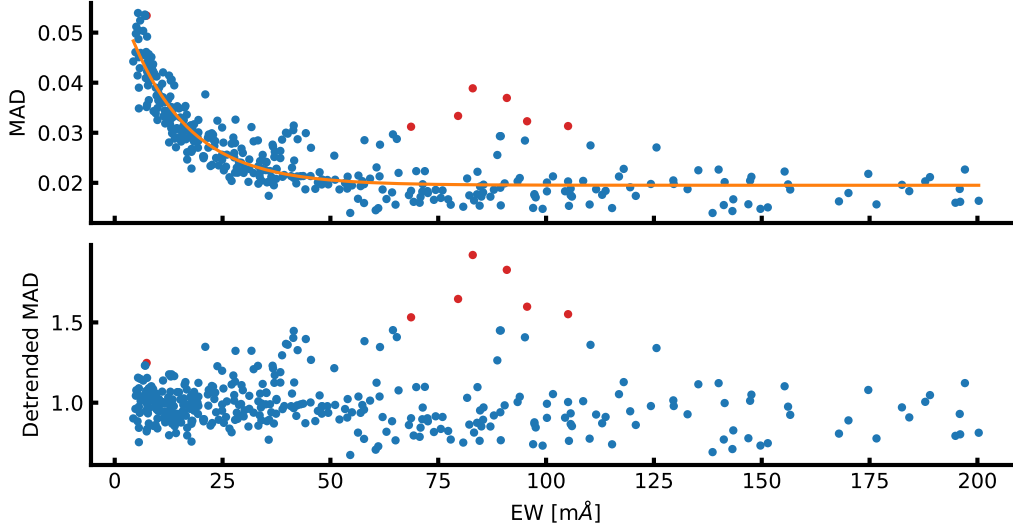
Figure 4.4: The most disperse lines. *Upper panel*: The MAD versus the original EW. The red points are the outliers which were discarded during this process. *Lower plot*: Same as above with the de-trended MAD by the exponential fit as shown in the upper panel.

4.2 HD20010

To test the NIR line list a well-studied solar-type star was needed. The spectrum for such a target needs to be available in the NIR at both high resolution and high S/N. An ideal place to look for such a star was the CRIRES-POP database (Lebzelter et al., 2012). Here, the best target for testing was HD 20010, an F8 subgiant star. At the time of writing this thesis and Andreasen et al. (2016) the spectrum of HD 20010 was not fully reduced. Here it is still contaminated by some telluric lines, and the wavelength solution used is not optimal; both which are essential, however a tedious and difficult task to accomplish.

HD 20010 star has been part of many surveys and is therefore well studied. Different parameters from the literature are listed in Table 4.2.

Table 4.2: Selection of literature values for the atmospheric parameters for HD 20010. The mean and a 3σ standard deviation is presented at the end of the table from the literature values included, which was used as a reference for the derived parameters.

Author	T_{eff} (K)	$\log g$ (dex)	[Fe /H] (dex)	ξ_{micro} (km/s)
Balachandran (1990)	6152	4.15	-0.27 ± 0.08	1.60
Favata et al. (1997)	6000	. . .	-0.35 ± 0.07	. . .
Santos et al. (2004)	6275 ± 57	4.40 ± 0.37	-0.19 ± 0.06	2.41 ± 0.41
Gonzalez et al. (2010)	6170 ± 35	3.93 ± 0.02	-0.206 ± 0.025	1.70 ± 0.09
Ramírez et al. (2012)	6073 ± 78	3.91 ± 0.03	-0.30 ± 0.05	. . .
Mortier et al. (2013a)	6114	. . .	-0.19	. . .
Mean	6131 ± 255	4.01 ± 0.60	-0.23 ± 0.14	1.90 ± 1.08

The data available at CRIRES-POP are in the raw format and pipeline reduced, while three small pieces of the spectrum are fully reduced on the web page[2]. The data is in the standard CRIRES format

---

[2] http://www.univie.ac.at/crirespop/data.htm

with each fits file including four binary tables with the data from the four detectors with the same resolution in each spectrum. In the future, the final reduced data will be presented by the CRIRES-POP team. In contrast to the pipeline reduced data, this will be of higher quality, a better wavelength calibration, and telluric corrected.

The EWs were measured of the pipeline reduced spectrum, and where there was an overlap with the fully reduced spectrum, the EW was measured in both cases as a consistency check. The measured EWs from the fully reduced spectra were consistent with the measured EWs from the pipeline reduced spectra, although with less noise in the fully reduced spectral parts. As mentioned above, the Y, J, H, and K-bands, which are all available for this star, were used in this analysis. The spectra come in pieces of 50 Å to 120 Å. These pieces overlap each other, and up to five EW measurements were made for some lines. Unfortunately, wavelength calibration is a difficult task for CRIRES owing to the rather small spectral regions measured on each detector. Each calibration was performed separately for each detector and required the availability of a sufficient number of calibration lines in the respective spectral region. This was not always the case and a default linear solution was applied. A pipeline reduced spectrum shows up as a stretched spectrum if the wavelength calibration is poor compared to a model spectrum or a solar spectrum, for example. The wavelength calibration does not have any effect on the signal-to-noise ratio, which is generally high for the spectrum of HD 20010. The signal-to-noise varies between 200 and 400 for different chunks. However, the stretched spectra will most likely have an effect on the measured EWs.

The pipeline reduced spectrum for HD 20010 contains tellurics and the wavelength is shifted in radial velocity. All of these factors make the line identification very difficult, so a program was developed[3] to properly identify the lines, which does the following:

1. Plotting the observed spectrum

2. Overplotting a model spectrum. In this particular case the solar spectrum was used since the atmospheric parameters are close enough, so the sun was able to serve as a model

3. Overplotting a telluric spectrum from the TAPAS web page (Bertaux et al., 2014)

4. Overplotting vertical lines at the location of lines in the list

5. Calculating the cross-correlation function (CCF) for the telluric spectrum with respect to the observed spectrum, locating the maximum value by a Gaussian fit, and using this to shift the telluric spectrum with the found RV

6. Performing the same as step 5, but for the model spectrum

7. Shifting the lines with the same RV as found for the model/solar spectrum

The final plot shows the shifted spectra, and the CCFs at the sides. An example of the software in use is shown in Figure 4.5. The two radial velocities (for the telluric and model spectrum) are part of the title of the plot. Once the lines were identified, the EWs were measured with the `splot` routine in *Image Reduction and Analysis Facility* (`IRAF`). The reason not to choose `ARES` for this task was to visually confirm the identification of the line given the relative poor wavelength calibration from the automatic pipeline. 249 Fe I lines and 5 Fe II EWs were measured compared to 344 Fe I lines and 13 Fe II

---

3   The program (and other small scripts) can be found here https://github.com/DanielAndreasen/astro_scripts
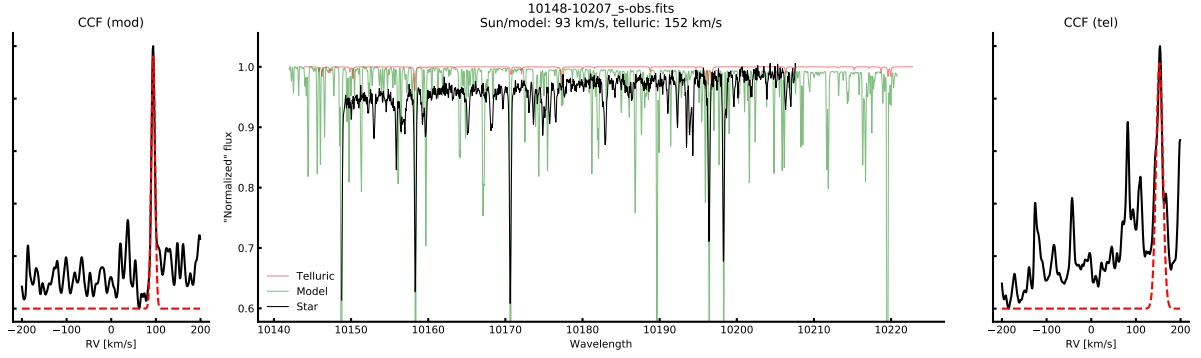
Figure 4.5: Line identification in piece of Arcturus spectrum with PHOENIX model and telluric model for correcting RV.

lines for the Sun over the whole NIR spectral region in the line list. Whenever there were more than one EW measurement of a line, due to overlap in different spectra, the average was used for the final EW. The stellar atmospheric parameters were derived using the standard procedure (see Section 3.3). Lines below 5 mÅ were removed in order to remove the lines which are most affected by contamination from either telluric or other line blends. Additionally, a cut in EP at 5.5 eV was made since the Fe I and Fe II lines usually used for stellar parameter determination in the optical regime are also limited to similar values (see e.g Sousa et al., 2008). Higher excitation potential lines are also more likely to be affected by non-LTE effects.

> Any reference for this?

When deriving the stellar atmospheric parameters, one outlier were removed at a time (after a completed minimization) until no outliers were present. Since we could only measure 5 Fe II lines, the parameter were also derived with $\log g = 4.01$ dex fixed at the reference mean value (see Table 4.2). The resulting atmospheric parameters and iron abundances are presented in Table 4.3. The effective temperature, surface gravity, and metallicity agree within the errors with the literature values. Similar parameters are obtained by fixing $\log g$ to the average literature value or by leaving it free.

Table 4.3: The derived parameters for HD20010 with and without fixed surface gravity.

	T_{eff} (K)	$\log g$ (dex)	ξ_{micro} (km/s)	[Fe/H] (dex)
Literature	6131 ± 255	4.01 ± 0.60	1.90 ± 1.08	-0.23 ± 0.14
	6116 ± 224	4.21 ± 0.58	2.45 ± 0.45	-0.14 ± 0.14
	6144 ± 212	4.01 (fixed)	2.66 ± 0.42	-0.13 ± 0.29

The errors on the atmospheric parameters for HD 20010 are much higher than what is achievable with other measurements in the literature, as presented above in Table 4.2. In order to explain these errors, the abundances for all lines which have at least two measurements of the EW were calculated from the highest and lowest measured EW. The differences in abundances are presented in Figure 4.6. The very large differences (more than 0.1 dex) translate to the high errors in the parameters.

This test strongly suggest that errors in the EWs, likely due to the telluric contamination and non-optimal reduction of the spectrum (poor default wavelength calibration), are responsible for the relatively large error in the derived stellar parameters. After the first analysis of HD 20010, the CRIRES-POP team published a fully reduced spectrum of 10 Leo (Nicholls et al., 2017) with telluric correction and an optimal wavelength solution. The results obtained from this star (see Section 4.6) are very promising for
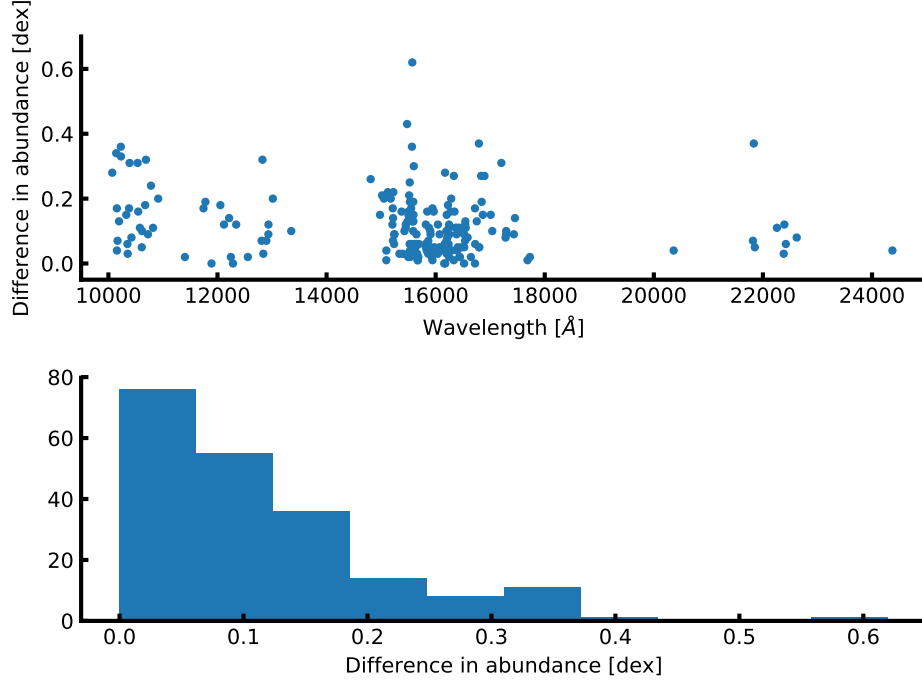
Figure 4.6: Difference in abundance for HD 20010 when multiple measurements of EW were obtained. The differences are between the lowest and highest measured EW in case of multiple measurements. This is shown against the wavelength (*upper panel*) and in a histogram (*lower panel*).

the method used here, and it encourage a complete re-visit of HD 20010 once the reduction is optimal.

4.3   The NIR line list - toward cooler stars

As will be seen in Section 4.2 the line list presented above was used to derive atmospheric parameters of HD 20010. Even though the first test of the line list was successful, it left room for improvements. The errors on the derived parameters were quite high for the spectral type compared results obtainable with a similar analysis utilising the optical spectrum (see Section 4.2 for details on this). Additionally, the derived metallicity was 0.10 dex higher than the literature values used.

If all derived parameters except metallicity are reliable (when compared to e.g. a literature value), then it suggest that the measured EW are either over- or underestimated. However, when using a line list for the first time like here, it can also suggest problems with the line list itself, most likely a bad calibration. This could have been wrong measurements of the EWs of the calibrator star, Sun in this case. This combines to several cases:

- Correct measurements of EWs of calibrator star:

  - Systematic lower measurements of EWs of target star leads to underestimated [M/H]

  - Systematic higher measurements of EWs of target star leads to overestimated [M/H]

  - Correct measurements of EWs of target star leads to correct [M/H]

- Systematic lower measurements of EWs of calibrator star:

– Systematic lower measurements of EWs of target star leads to underestimated [M /H]

– Systematic higher measurements of EWs of target star can lead to underestimated, correct or overestimated [M /H] depending on the amount of systematic higher measurements

– Correct measurements of EWs of target star leads to underestimated [M /H]

• Systematic higher measurements of EWs of calibrator star:

– Systematic lower measurements of EWs of target star can lead to overestimated, correct or underestimated [M /H] depending on the amount of systematic lower measurements

– Systematic higher measurements of EWs of target star leads to overestimated [M /H]

– Correct measurements of EWs of target star leads to overestimated [M /H]

It is important to note, that *correct* has been used here, assuming a perfect setup, that includes perfect model atmosphere, perfect radiative transfer code, etc. In reality the final [M /H] (and the other parameters) measured by different groups will occasionally differ regarding the setup used (see e.g. Hinkel et al., 2016).

As described in Section 4.1 the EW of the Sun (calibrator star) was measured with `ARES`. A crucial option to set when using `ARES` is the `rejt` parameter as mentioned in Section 3.3.2. This option is used to place the continuum and will thus directly affect the measured EW. At the time of compiling the first version of the line list it seems the `rejt` value used did not reflect the high S/N of the spectrum, thus placing the continuum too low and thereby underestimate the EW. The `rejt` parameter used was 0.995 (S/N=200), while it should have been closer to 0.999 (S/N=1000). This might have excluded some of the weakest lines, since a cut in EW was made at 5 mÅ.

In this second version of the line list, the goal is to:

1. Make sure the EW measurements are as correct as possible by measuring them by hand

2. Free of blended lines in cooler stars (K stars in this case)

The second point is a similar exercise which was done in the optical by Tsantaki et al. (2013), where blended lines were removed from the larger line list by Sousa et al. (2008). This allowed to determine the atmospheric parameters of stars colder than 5000 K. However, the optical spectrum still suffer for severely blended lines at low $T_{\rm eff}$, thus this method does not work for M stars.

Both of the above steps were done at the same time, by measuring the EWs by hand using `IRAF`. Whenever a line was difficult to reliably measure, i.e. a consistent measurement was not possible/easy, it was discarded since it was blended. This can be seen in Figure 4.7 where the EW measurements from the first version is shown against this version with the manual measurements. There are some measurements of EW higher than 150 mÅ which should have been removed. These lines have not been used during the analysis, however they were kept since they might appear useful on a later stage.

With the increased access to high quality NIR spectra and the gained experience during the course of the thesis, it was possible to improve the line list by a second visual inspection on the solar spectrum.

After the new measurements of the EWs, the line list was re-calibrated according to the procedure described above. The average change in log gf is -0.062 ± 0.157, i.e. on average the oscillator strengths are higher in the second version compared to the first version of the line list.

With the second version there are only 5 Fe II lines left which is a concern since these are crucial for the derivation of the surface gravity.
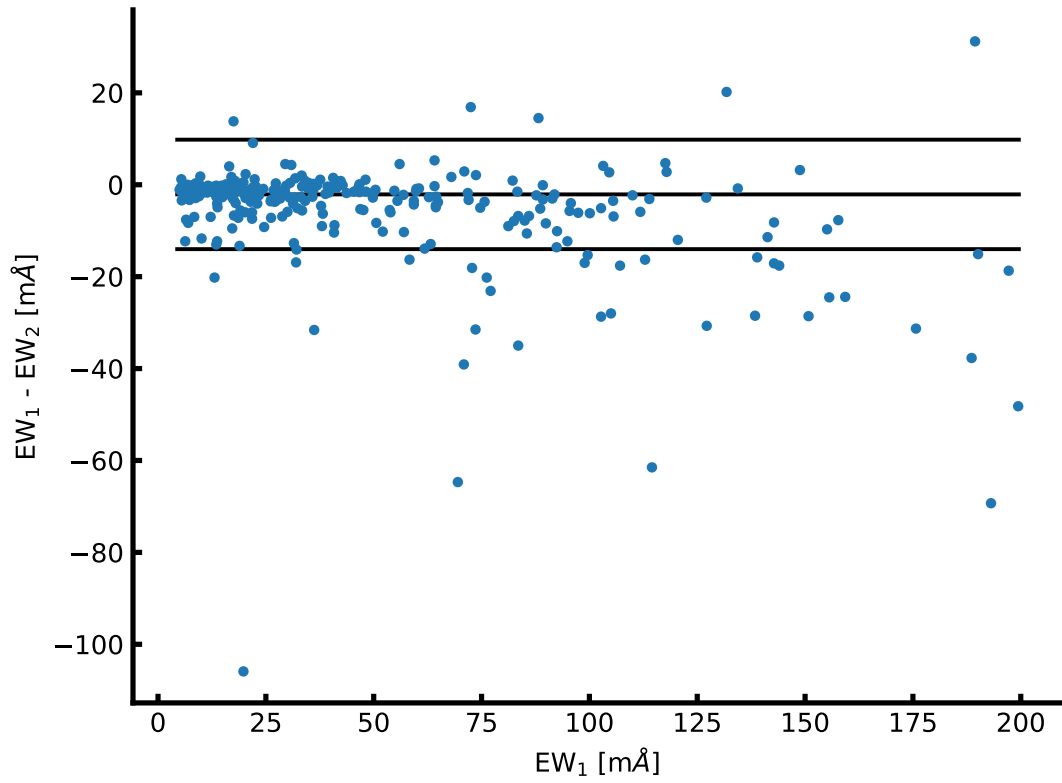
Figure 4.7: Comparison of the EW from the first version of the line list, EW_1, and the second version, EW_2. The EWs are generally higher in the second version, with an average difference between the two version of (2.1 ± 11.1) mÅ. The three horizontal lines show the average value and the standard deviation.

4.4 HD 20010 - revisited

During the analysis of Arcturus (see Section 4.5) and 10 Leo (see Section 4.6) with the refined line list presented in Section 4.3 it was a simple task to apply the updated line list on HD 20010 a second time as a test whether it would perform similar, worse or better. This is compared to results obtained from the literature and the previous results in Section 4.2.

Therefore HD 20010 was revisited, and the atmospheric stellar parameters were derived. The measured EWs from the results above in Section 4.2 were kept, however the lines which did not make the cut in the second version of the line list were removed. Moreover, the $\log gf$ values were updated since these were re-calibrated.

At this point `FASMA` was fully developed and was used to obtain the results which are shown in Table 4.4 along with the results for Arcturus and 10 Leo (details on their parameters will be found below). The agreement with the adopted average literature values are better for HD 20010 compared to the results from above in Section 4.2 (especially [Fe /H] and $\log g$), and smaller errors with the updated results. This first test of the line list already shows promising results. The literature values are slightly different here than compared to the first analysis of this star. This is solely because other references were used, the PASTEL catalogue (Soubiran et al., 2016). However, this does not change the improvement seen.

Table 4.4: Results for the three stars where first set of parameters are the literature values as presented in Table 4.1, second set of parameters are results with $\log g$ set to the same value during the minimization procedure as found in the literature (fixed), and last set of parameters are with all parameters free during the minimization procedure.

	HD 20010	10 Leo	Arcturus
Literature			
T_{eff} (lit.)	6152 ± 95	4741 ± 60	4300 ± 110
$\log g$ (lit.)	3.96 ± 0.19	2.76 ± 0.17	1.60 ± 0.29
[Fe /H] (lit.)	-0.27 ± 0.06	-0.03 ± 0.02	-0.54 ± 0.11
ξ_{micro} (lit.)	1.17 ± 0.24	1.45 ± 0.08	1.93 ± 0.13
$\log g$ fixed			
T_{eff}	6161 ± 164	4761 ± 118	4357 ± 74
$\log g$	3.96 (fixed)	2.76 (fixed)	1.60 (fixed)
[Fe /H]	-0.18 ± 0.11	0.01 ± 0.07	-0.55 ± 0.04
ξ_{micro}	1.72 ± 0.44	1.25 ± 0.11	1.55 ± 0.10
All free			
T_{eff}	6162 ± 184	4805 ± 98	4439 ± 62
$\log g$	4.08 ± 0.77	2.42 ± 0.61	1.20 ± 0.20
[Fe /H]	-0.18 ± 0.11	-0.01 ± 0.07	-0.58 ± 0.06
ξ_{micro}	1.59 ± 0.49	1.23 ± 0.10	1.55 ± 0.10

4.5 Arcturus

Arcturus is one of the brightest stars on the Northern hemisphere with a V magnitude of -0.05 (Ducati, 2002), and is well studied (see e.g. Griffin and Griffin, 1967; McWilliam, 1990; Ramírez et al., 2013, to mention just a few), and a benchmark star in current spectroscopic surveys such as Gaia-ESO (Jofré et al., 2014; Smiljanic et al., 2014). Hence it is a prime target for testing with the numerous measurements of

the atmospheric parameters.

Use benchmark parameters instead of PASTEL!

The atlas of Arcturus, acquired at Kitt Peak National Observatory using the FTS spectrograph at the Mayall telescope by Hinkle et al. (1995a), covers the spectral range of interest (YJHK bands). Strong telluric features were identified with a spectrum from the TAPAS web page (Bertaux et al., 2014) which was useful during the line identification. The atlas also comes with a telluric standard and the ratio of the two spectra in order to correct for the tellurics. The telluric spectrum from TAPAS was only used for telluric line identification. Both the telluric corrected and non-corrected spectra was used during the analysis, however the focus was on the non-corrected spectrum since it is simple to identify the telluric lines in this spectrum.

The atlas consists of both a summer observation set and a winter observation set. The two data sets have been obtained in order to minimise the effect of tellurics at different spectral regions. A comparison between the two sets of measured EWs, both the manual measurements using `IRAF` and the automatic measurements using `ARES`, are shown in Figure 4.8. The automatic EW measurements for the summer set and winter set show excellent agreement with a dispersion of 7 mÅ and a systematic difference of 0.1 mÅ, i.e. ineligible. This means that the two data sets are very similar, thus it was decided to only manually measure the EWs for one set (summer). Since this is a test of the line list (rather than a study of Arcturus) and the fact that the EWs are very similar, the parameters are only derived from the summer set with the EWs measured by `ARES`. Parameters were derived with and without $\log g$ set to a fixed value (1.60 dex, the average literature value adopted). The derivation of the parameters followed the same procedure as described above for HD 20010 using `FASMA`. Again outliers in abundance were removed one at the time until there were no more outliers. The final results are presented in Table 4.4 together with mean parameters from the literature.

There is overall good agreement between the derived parameters and the average values from the literature adopted (see Table 4.4). The only parameter being difficult to measure is the surface gravity due to the low number of Fe II lines in the NIR. This was already suspected and mentioned in Section 4.3. There are also some problems determining ξ_{micro}, however this is not a major concern, since it is not as important a parameter as the other three. The derived metallicity is consistent with the literature here which is promising since there were some problems with this parameter in Section 4.2.

4.6 10 Leo

The spectrum for 10 Leo was recently made available by the CRIRES-POP team (Nicholls et al., 2017). 10 Leo is very similar to Arcturus, which is also one reason this star was the first to be fully reduced by the CRIRES-POP team. The spectrum is divided into several pieces according to the atmospheric windows in the NIR: YJ (only together), H, K, L, and M. Here the first three were used since this is the range of the line list. Some small gaps are present in the spectrum due to tellurics that could not be properly removed, low S/N, bad pixels, etc. Rather than giving an uncertain interpolation, Nicholls et al. (2017) decided to leave small gaps in the data. This had very little effect on this line by line analysis, however, due to those gaps, one Fe II line were not measured which are crucial to determine the surface gravity.

The approach for determining the atmospheric stellar parameters for 10 Leo is identical to Arcturus. `ARES` was used on each band (YJ, H, and K-band) separately. For the small gaps in the spectrum, the flux was simply set to 1, since the spectrum has already been normalised. This also prevented `ARES` to
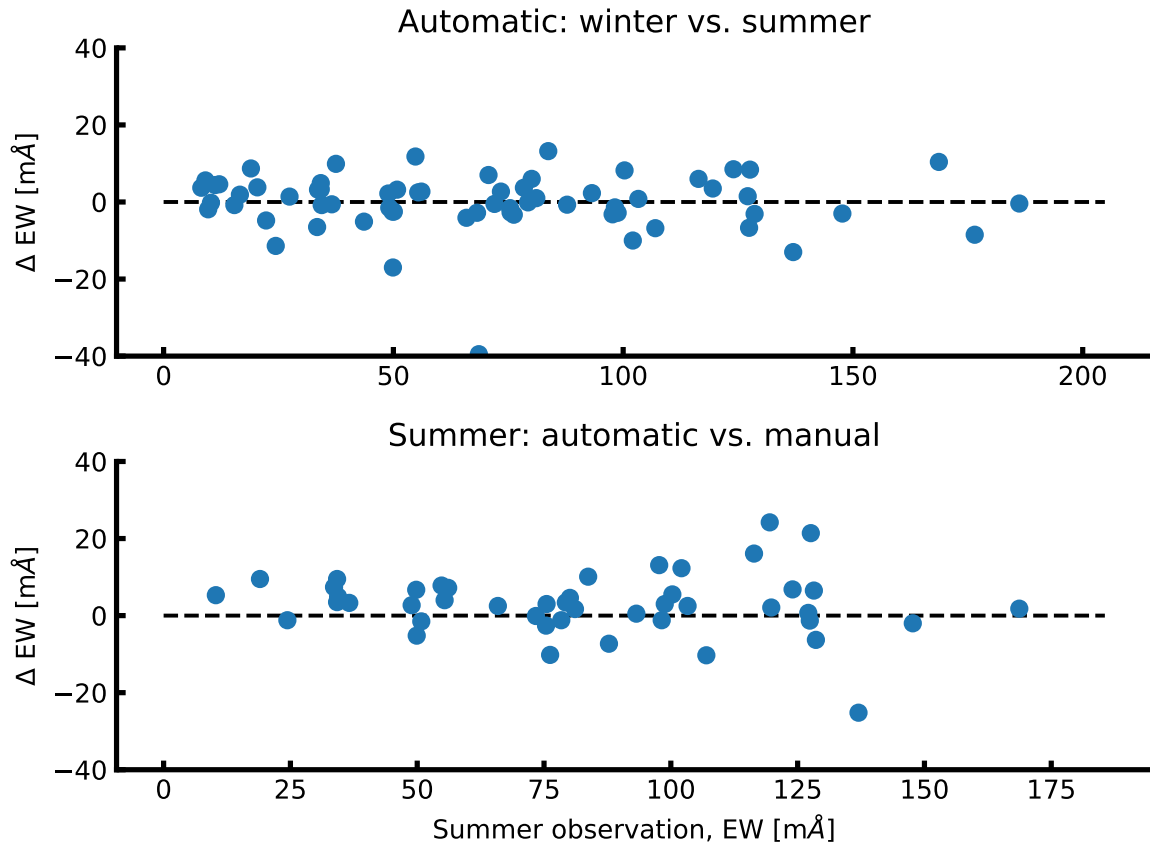
Figure 4.8: Top figure: Difference of the automatic EW measurements between the summer observations and winter observations from the Arcturus spectra. Bottom figure: Same as above, but with manual measurements from ARES (summer) and automatic measurements (summer).

identify and measure any lines in these regions. The EWs from the three regions were combined to one final line list used for the determination of the parameters. The final results can be seen in Table 4.4.

Generally the derived parameters are in excellent agreement with the literature values listed here. A 64 K difference is seen for T_{eff} with $\log g$ set as a free parameter, well within the errors. The only parameter that show a discrepancy compared to the literature value is ξ_{micro} with a difference of 0.22 km/s, which is at the limit of the errors reported. We note that this parameter is not reported in the PASTEL database, and this was a derived parameter from an empirical relation. $\log g$ was derived with large errors which is a result from the few Fe II (three lines) measured. However, the $\log g$ is not far from the literature value, only 0.34 dex lower, which is well within the large errors reported. However, it also shows it is safer to obtain $\log g$ from other more reliable methods, such as asteroseismology when possible.

> Then find some reliable values instead

4.7   Synthetic cool stars

Mainly due to lack of available high quality spectra in the NIR, it is a good test to use a simulation. By deriving parameters from synthetic spectra, it is possible to carefully control the work flow, in the sense that the target parameters are known. In this section the synthetic library[4] by Husser et al. (2013) will be used. These are synthetic spectra created from spherical symmetric PHOENIX atmosphere models under local thermodynamic equilibrium. The model atmospheres does not include dust settling since all models are hotter than 2300 K. The details for the atmosphere models can be seen in Husser et al. (2013).

For this test only the T_{eff} will vary, ranging from 3500 K to 6000 K with most densely sampled at lower temperatures (see Figure 4.9). Here $\log g = 4.5$ dex and [M /H] = 0.00 dex, i.e. synthesised dwarf stars with solar metallicity. Before analysing the data, the spectra was broadened to have a spectral resolution of 100 000, comparable with current and future high resolution NIR spectrographs.

In this test ARES was used to measure the EWs of as many lines from the line list (second version) as possible for each of the 12 synthetic spectra. These line list were used to derive parameters with two different model atmospheres, ATLAS9 (Kurucz, 1993) and MARCS (Gustafsson et al., 2008), with FASMA. This was done twice, with all parameters derived from FASMA (Figure 4.9), and again with $\log g$ fixed at 4.5 dex and ξ_{micro} fixed which means it is changed in each iteration (see Section 3.3 for details) according to an empirical relation. The latter case with fixed parameters is shown in Figure 4.10.

For the results with $\log g$ and ξ_{micro} fixed at the correct parameters during the derivation, the first thing noticed is the good agreement between the two model atmospheres. Second, the derived T_{eff} are underestimated for $T_{\mathrm{eff}} > 4000$ K while for the two lowest T_{eff} it is the opposite case. It is important to know that the grid of ATLAS9 models only go down to 3750 K, however these synthetic spectra were included for completeness. For $T_{\mathrm{eff}} > 4000$ K it is systematically lower by the same amount, roughly 100 K. As have been shown in the previous sections in this chapter, the methodology is reliable for T_{eff} ranging from 4300 K to 6200 K (see Table 4.4). With the consistent offset in T_{eff}, it is a clear indication that the methodology is reliable down to these temperatures.

In the case of $\log g$ and ξ_{micro} fixed the derived mean metallicity for the 12 synthetic spectra are [Fe /H] = (-0.12 ± 0.17) dex and [Fe /H] = (-0.19 ± 0.12) dex for the ATLAS9 and MARCS model atmospheres, respectively. The offset is likely to be found in the discrepancy between the model atmosphere and real data (Arcturus in this case) as shown in Figure 4.12. Here a PHOENIX synthetic spectrum with

---

[4]   http://phoenix.astro.physik.uni-goettingen.de/
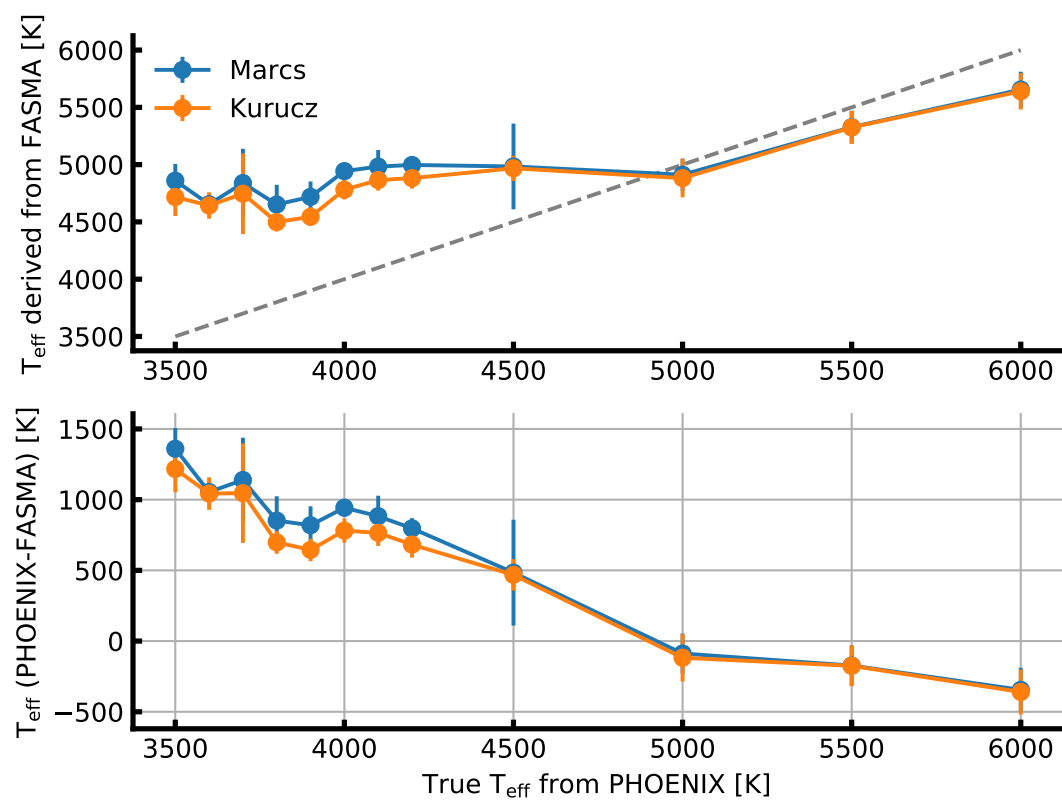
Figure 4.9: Derived parameters of 12 synthetic PHOENIX spectra with varying T_{eff}.

$T_{\mathrm{eff}} = 4300\,\mathrm{K}$, $\log g = 1.50\,\mathrm{dex}$, and $[\mathrm{Fe}/\mathrm{H}] = -0.50\,\mathrm{dex}$ is plotted with a piece of the Arcturus atlas from Section 4.5. The synthetic spectrum has similar parameters as Arcturus, thus they should have similar spectral features. However, in the plot the spectral lines are deeper for the PHOENIX model and there seem to be more absorption lines in this synthetic spectrum compared to the observed spectrum. This have a direct effect on the measured EWs as they will be blended and deeper than expected.
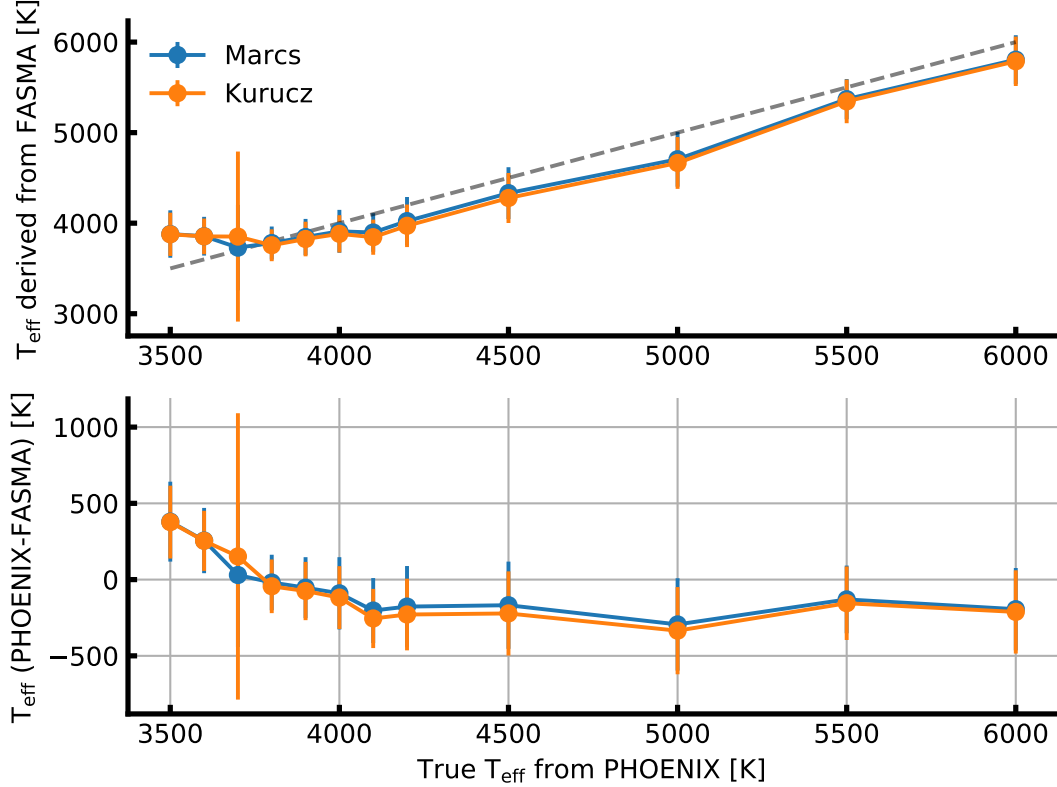
Figure 4.10: Derived parameters of 12 synthetic PHOENIX spectra with varying T_{eff}. Here $\log g$ is fixed at 4.5 dex and ξ_{micro} fixed according to an empirical relation, thus only deriving T_{eff} and $[\mathrm{Fe}/\mathrm{H}]$.

A comparison with EWs from the iron line list from the observed Arcturus spectrum and the synthetic spectrum which resembles Arcturus closest is shown in Figure 4.11. The EWs are clearly getting more disperse with increasing EW.

When all the parameters are derived it is a very different story for T_{eff}. In this case the T_{eff} are overestimated for the synthetic spectra colder than $5000\,\mathrm{K}$. Above this limit the T_{eff} are slightly underestimated with a hint of the results getting worse further from this limit. The reason for this can partly be found in the measured Fe II lines. As mentioned before, these are used to determine $\log g$. There have been measured between 1 and 3 Fe II lines, generally fewer the lower T_{eff} is, out of 5 possible measurements. The mean derived values for the surface gravity are $\log g = (1.11 \pm 1.63)\,\mathrm{dex}$ and $\log g = (1.38 \pm 1.45)\,\mathrm{dex}$ for ATLAS9 and MARCS model atmospheres, respectively. Similarly for the metallicity the following mean values are $[\mathrm{Fe}/\mathrm{H}] = (-0.73 \pm 0.37)\,\mathrm{dex}$ and $[\mathrm{Fe}/\mathrm{H}] = (-0.73 \pm 0.38)\,\mathrm{dex}$ for ATLAS9 and MARCS model atmospheres, respectively. The measured iron abundance for the 12
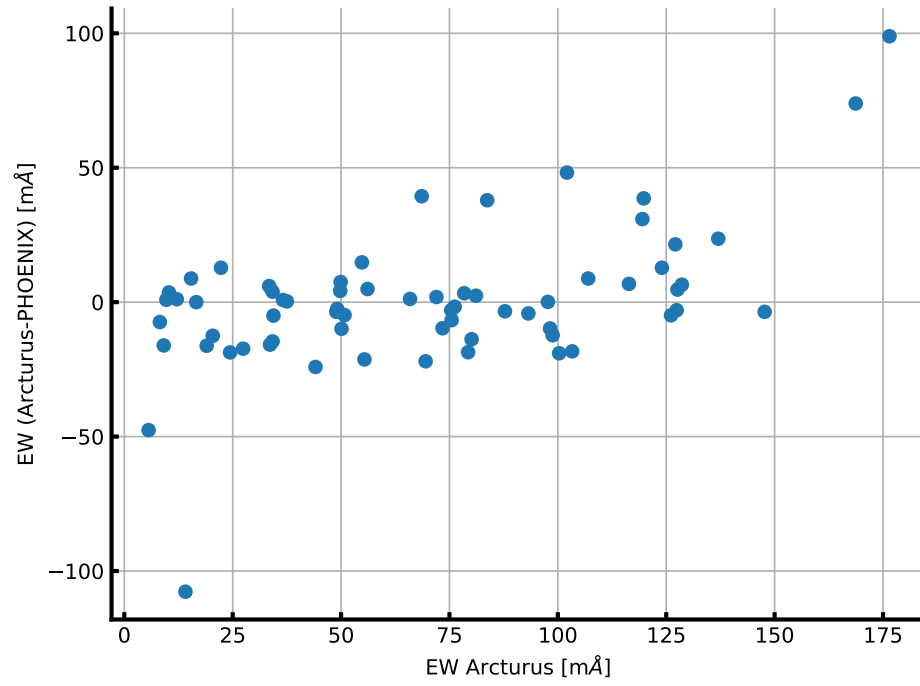
Figure 4.11: Common EWs between Arcturus and the synthetic spectrum with closest parameters (see text for details). The EWs are getting more disperse with increasing EW which is expected when seeing the direct comparison of the spectrum in Figure 4.12.

synthetic spectra can be seen in Figure 4.13. The figure only includes runs which reached convergence with `FASMA`.
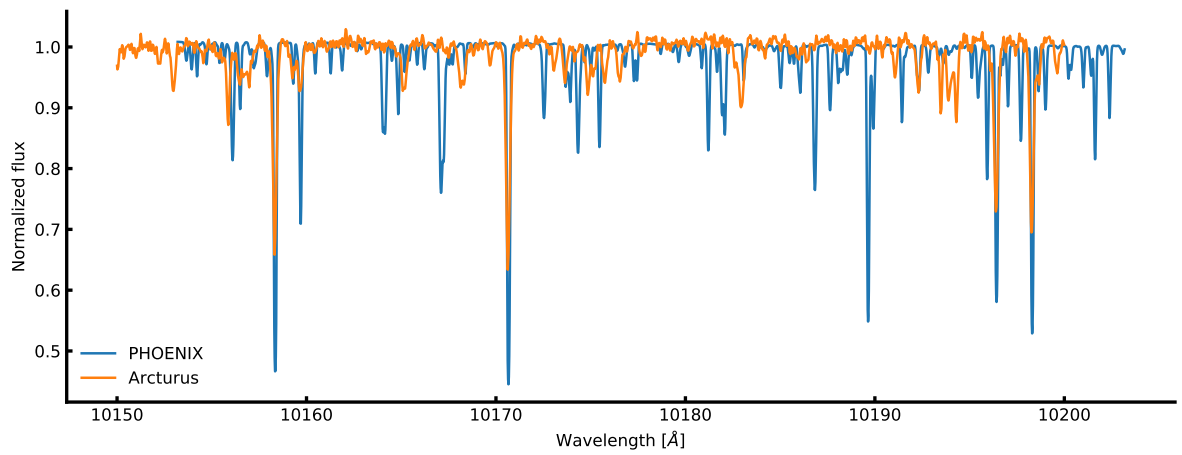
Figure 4.12: Comparison between the Arcturus atlas and a PHOENIX synthetic spectrum with similar parameters to Arcturus (see text for details).
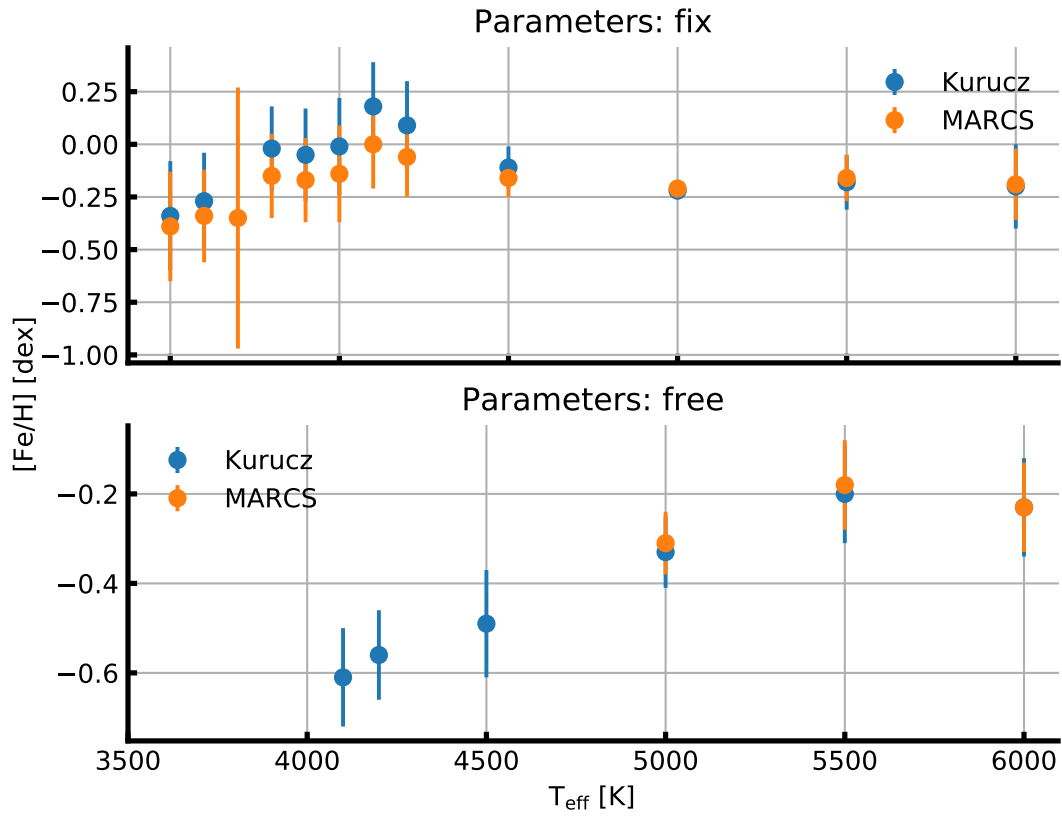
Figure 4.13: Derived [Fe /H] with respect to the true T_{eff} for runs that reached convergence. *Top panel*: $\log g$ fixed at $4.5\,\mathrm{dex}$ and ξ_{micro} to the empirical relation (see text for details). *Lower panel*: All parameters free.

4.8   Parameter dependence on EP cut

It is common practise, as in this case, to make a cut in EP for a line list when deriving parameters. This was suggested in Andreasen et al. (2016) (later done in Andreasen et al., 2017a) for the NIR line list used here. This cut was made at 5.5 eV, inspired by a similar cut in the optical (Sousa et al., 2008), including only lines below this limit. The lines with higher EP might also be affected by non-LTE effects which is not treated in this methodology.

As the parameters are dependent on this cut in EP, it seemed interesting to divide a line list in two with upper and lower EPs and analyse those separately. Before going into that analysis it is important to note, that the parameters should not depend on any cut in EP if the theory is right, the radiative transfer code is working properly, and the atmospheric models are correct. Lines with different EP are likely to be formed in different layers of the atmosphere as discussed in Section 2.2, however this should not effect the final derived abundance, which is the problem here.

Make a figure that shows this

Chapter 5

SWEET-Cat

Part of the work during the thesis has been dedicated to regularly update SWEET-Cat[1], a catalogue with all discovered planet hosts, and the stellar parameters.

In this chapter a detailed description of SWEET-Cat will be presented. Moreover an analysis of 50 planet hosts was performed during the thesis with updated planetary parameters (mass and radius).

5.1   What is SWEET-Cat?

As mentioned above, SWEET-Cat is a catalogue of planet host stars. However, the strength of SWEET-Cat is the homogeneously analysed stars utilising the method described in Section 3.3 with `FASMA` or a similar tool before the creation of `FASMA`.

In the era with a large number of discovered exoplanets (more than 3500 confirmed exoplanet at the moment of writing), the time for in-depth statistical studies has arrived. However, when conducting these studies it is crucial to have consistent measurements of e.g. stellar atmospheric parameters. This can be obtained by using a single analysis to obtain these parameters, as it is know that different methods will lead to different results (see e.g. Hinkel et al., 2016, for a recent review).

To obtain stellar atmospheric parameters from one method is an on-going goal with SWEET-Cat, where high quality spectra are obtained for stars hosting planets. These are used to determine the stellar parameters in a homogeneous way. All stars in SWEET-Cat analysed with the method from our group are marked with a flag showing whether it is analysed homogeneously or not. The columns provided in SWEET-Cat are summarised in Table 5.1. It is important to note that SWEET-Cat does not include any planetary parameters.

SWEET-Cat is updated on a weekly basis if new planet hosts are discovered, and whenever planet hosts have been analysed with the method from our group, as described in this thesis.

5.2   Data for 50 planet hosts

In this section the data for a large update to SWEET-Cat will be described. The majority of the data comes as a result from proposals submitted for observational time, while some of the data was found in the archive. In the next section the analysis of the 50 spectra will be presented along with the results.

---

[1]   https://www.astro.up.pt/resources/sweet-cat/

Table 5.1: Columns in SWEET-Cat

Column	Unit	Description
Name		Popular stellar name
HD number		HD number
RA	deg	Right ascension
Dec	deg	Declination
Vmag	mag	V magnitude
$\sigma(\text{Vmag})$	mag	Error on V magnitude
π	mas	Parallax
$\sigma(\pi)$	mas	Error on parallax
Source of π		Source of parallax measurement
T_{eff}	K	Effective temperature
$\sigma(T_{\text{eff}})$	K	Error on effective temperature
$\log g$	dex	Surface gravity
$\sigma(\log g)$	dex	Error on surface gravity
$\log g_{\text{LC}}$	dex	Surface gravity corrected from light curves
$\sigma(\log g_{\text{LC}})$	dex	Error on surface gravity corrected from light curves
ξ_{micro}	km/s	Micro turbulence
$\sigma(\xi_{\text{micro}})$	km/s	Error on micro turbulence
[Fe /H]	dex	Metallicity
$\sigma([\text{Fe /H}])$	dex	Error on metallicity
Mass	$M_\odot$	Stellar mass
$\sigma(\text{Mass})$	$M_\odot$	Error on stellar mass
Reference		Reference for parameters
Homogeneity flag	0/1	0 for not homogeneous analysis, 1 otherwise
Last updated	date	Last updated
Comments		Any special remarks/comments (e.g. M star)

5.2.1   Data collected from proposals

Data[2] for 43 out of the 50 stars were collected by the SWEET-Cat team using the UVES/VLT (Dekker et al., 2000), FEROS/2.2m telescope in La Silla (Kaufer et al., 1999), and FIES/NOT (Frandsen and Lindberg, 1999) spectrographs. The remaining spectra were found in various archives. This includes spectra from the HARPS/3.6m telescope in La Silla (Mayor et al., 2003) and ESPaDOnS/CFHT (Donati, 2003). Some characteristics of the spectrographs are presented in Table 5.2 with the mean S/N for the spectra used. The S/N for each star can be seen in Table A.1 along with the atmospheric parameters of the stars. The S/N is measured automatically by ARES, however note that ARES smoothes the spectra before measuring the S/N, hence it is listed higher than the actual S/N. These 50 stars are confirmed exoplanet hosts listed in SWEET-Cat, but they belonged to the list of stars that have not previously been analysed by our team.

---

[2]   Based on observations collected at the La Silla Observatory, ESO (Chile), with FEROS/2.2m (run 2014B/020), with UVES/VLT at the Cerro Paranal Observatory (runs ID 092.C-0695, 093.C-0219, 094.C-0367, 095.C-0324, and 096.C-0092), and with FIES/NOT at Roque de los Muchachos (Spain) (runs ID 14AF14 and 53-202).

Table 5.2: Spectrographs used for this paper with their spectral resolution, wavelength coverage, and mean S/N from the spectra used.

Spectrograph	Resolution	Spectral range	Mean S/N
HARPS	115 000	378 nm to 691 nm	642
UVES	110 000	480 nm to 1100 nm	212
ESPaDOnS	81 000	370 nm to 1050 nm	775
FIES	67 000	370 nm to 730 nm	763
FEROS	48 000	350 nm to 920 nm	208

5.2.2   Data collected from archive

The spectra[3] was obtained with the highest possible resolution for a given spectrograph, and in cases with multiple observations, we include all the observations unless a spectrum is close to the saturation limit for a given spectrograph. For multiple spectra, we combine them after first correcting the radial velocity (RV) and using a sigma clipper to remove cosmic rays. The individual spectra are then combined to a single spectrum for a given star to increase the S/N. This single spectrum is used in the analysis described below. For most of the spectra in the archive included here, several spectra were combined as described above, while for the observations dedicated to this work, the spectrum would be a single spectrum, or in cases of faint stars, it would be observed a few times to reach the desired S/N. This is mostly due to the difference in science cases behind the observations; for example, the HARPS spectra were mostly used for RV monitoring or follow-up of the exoplanet(s), while the UVES spectra were mostly used to characterise stellar parameters or other similar projects.

5.3   Analysis of 50 planet hosts

The method of determining atmospheric parameters from the curve of growth analysis has been applied several times in the optical (see e.g. Mortier et al., 2013b; Santos et al., 2013; Sousa et al., 2011; Tsantaki et al., 2013). When studying stars with planets and any correlations between stellar and planetary parameters it is important to have a homogeneous characterisation of the stars. An effort to create such a sample was initiated by Santos et al. (2013) with the SWEET-Cat database. The motivation to homogenise the stellar hosts is mainly to compare the hosts and make statistical studies on one consistent scale. When doing these statistical studies, the results might otherwise suffer from offsets between different methods.

The skills acquired during the NIR studies as mentioned above were directly translated into deriving parameters for a sample of 50 known planet host stars that were not previously analysed by our group (Andreasen et al., 2017b). The spectra of these stars were required at UVES, FIES, HARPS, and ESPaDOnS with the mean S/N higher than 200.

A Hertzsprung-Russell diagram of the sample can be seen in Figure 5.1. The sample covers a large range of T_{eff}, FGK, while there are both dwarf, sub-giant, and some giant stars. The colours indicate the

---

[3]   Based on observations collected at the La Silla Observatory, ESO (Chile), with HARPS/3.6m (runs 60.A-9036(A), 072.C-0488(E), 081.C-0842(D), 083.C-1001(A), 084.C-0229(A), 087.C-0012(B) 089.C-0732(A), 091.C-0034(A), 092.C-0721(A), 093.C-0409(A), 183.C-0972(A), 188.C-0265(A,D,F,G,H,I,J,K,L,M,N), 192.C-0852(A,M)), and with ESPaDOnS/CFHT at the National Research Council of Canada (runs 14AF14, 07bo03, 11AQ78, 05AC23, 06AF22).

$\log g$. In order to determine the luminosity of each star the simple relation

$$L = 4\pi R^2 \sigma T_{\text{eff}}^4$$

is used, where L is the luminosity, R is the stellar radius, and σ is the Stefan-Boltzmann constant. In solar units this relation is simply:

$$\frac{L}{L_\odot} = \left(\frac{R}{R_\odot}\right)^2 \left(\frac{T_{\text{eff}}}{T_{\text{eff},\odot}}\right)^4$$

In order to determine the the stellar radius, the empirical relation from Torres et al. (2010) was used.
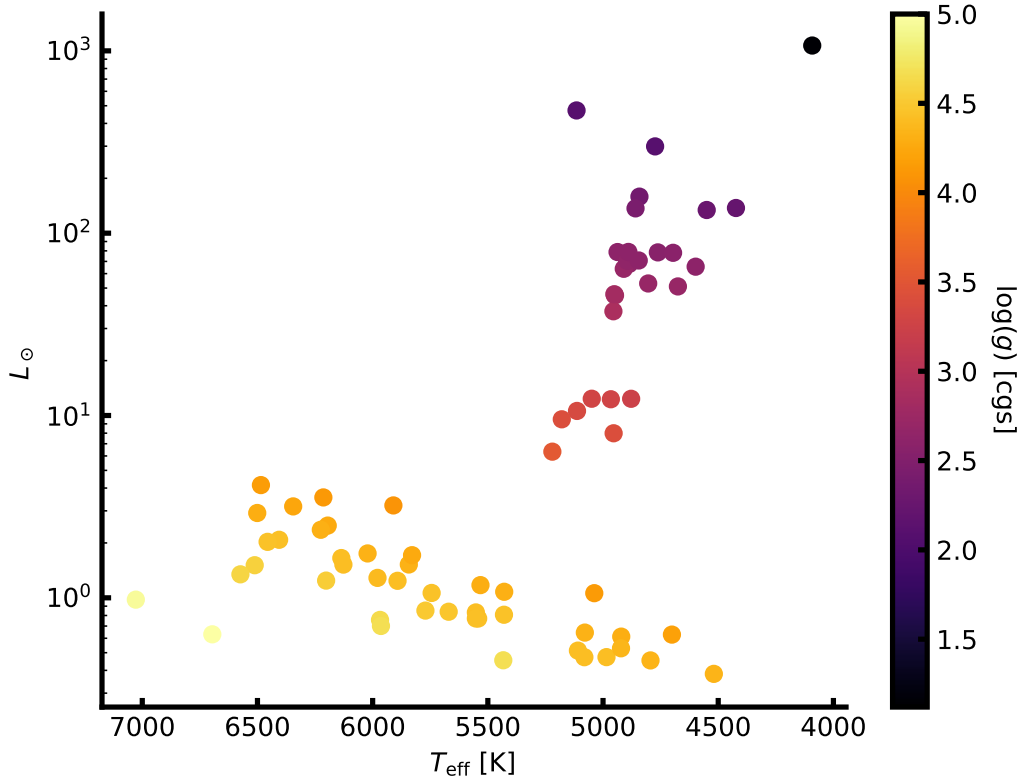
Figure 5.1: A Hertzsprung-Russell diagram of the sample of 50 planet host stars added to SWEET-Cat. The parameters were derived using optical high resolution and high S/N spectra in tandem with `FASMA` and an optical line list. The colour scale shows the derived $\log g$ for each star.

The parameters were derived using `FASMA` with the optical line list compiled by Sousa et al. (2008) and Tsantaki et al. (2013) for stars where T_{eff} was below 5200 K. All the new derived parameters were added to SWEET-Cat, available for the community.

A correction to the spectroscopic surface gravity ($\log g_{\text{spec}}$) is applied based on asteroseismology as

found by Mortier et al. (2014) given by:

$$\log g_{\rm seis} = \log g_{\rm spec} - (3.89 \pm 0.23) \times 10^{-4}\, T_{\rm eff} + 2.10 \pm 0.14, \tag{5.1}$$

where $\log g_{\rm seis}$ is the corrected surface gravity. This correction is only used for FGK dwarf stars, i.e. between $4800\,{\rm K} \leq T_{\rm eff} \leq 6500\,{\rm K}$ and $\log g \geq 4.2\,{\rm dex}$. For stars with a $\log g$ lower than this limit the correction will not be applied, and if the $\log g$ changes to below this limit after the correction, the spectroscopic $\log g$ will be used again. The correction for $\log g$ depends on both $T_{\rm eff}$ and $\log g$. The correction can be up to $0.5\,{\rm dex}$, depending on the $T_{\rm eff}$.

With these updated parameters the completeness of SWEET-Cat for stars brighter than V magnitude 10 is 85% (77% for stars brighter than 12). For fainter stars it is time expensive to acquire spectra of the quality needed for this method. Moreover, many of the fainter planet host stars have been observed with the *Kepler* space mission, where most stars are faint.

5.3.1   Habitable zone

The habitable zone of a star is at the distance where liquid water may exists. This distance depends on $T_{\rm eff}$ and the luminosity, but also on the planetary atmosphere and its composition. Using Kopparapu et al. (equation 3 described in 2013) to calculate the inner and upper limits of the habitable zone. The equation is rather simple:

$$d = \sqrt{\frac{L/L_\odot}{S_{\rm eff}}}\,{\rm AU},\, S_{\rm eff} = S_{\rm eff,\odot} + aT_* + bT_*^2 + cT_*^3 + dT_*^4, \tag{5.2}$$

where $T_* = T_-SI5780K$, and the coefficients can be found in Table 3 in Kopparapu et al. (2013), which depends on the specific model of habitable zone used. Here are used the "Runaway Greenhouse" for the inner limit and "Maximum Greenhouse" for the outer limit of the habitable zone. The equation above is only valid for main sequence stars FGKM, thus only stars with $\log g \geq 4.2\,{\rm dex}$ have been included.

It was possible to find three planets within this zone; GJ 785 c, HD 37124 c, and KELT-6 c. These planets does not have known radii, and their minimum masses are $(0.076, 0.652, 3.710)M_{\rm Jupiter}$, respectively. Thus, it is fair to assume they are all gas planets. All three host stars are metal-poor. A correlation between orbital period and host star metallicity is known (see e.g. Adibekyan et al., 2013), where metal-poor stars have planets with higher orbital period. It is thus not a surprise that the three planets found in the habitable zone all orbit a metal-poor star. A quick summary of the system is shown in Table 5.3.

In Figure 5.2 the habitable zone of the stars analysed here are shown along with the location of the planets. The three systems mentioned above are highlighted in the figure.

5.3.2   Changes to planetary parameters

As a results to the analysis above, it is expected that some planetary parameters will change compared with the previous literature values.

Therefore the radius and mass of all the 50 new stars updated in SWEET-Cat were computed using the empirical formula presented in Torres et al. (2010). Some of the stars have radii derived from different methods, usually from isochrones. These radii generally show a good correlation with radii derived from
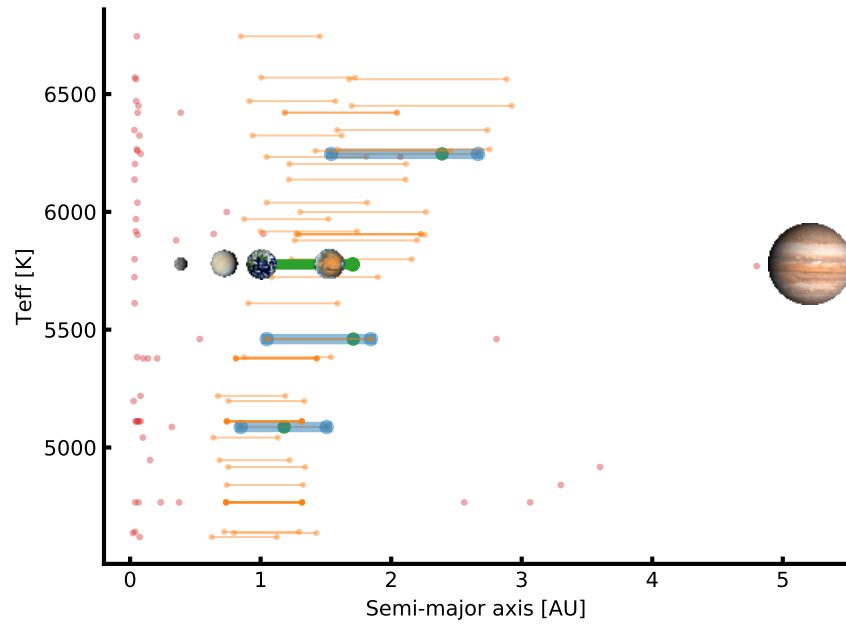
Figure 5.2: The habitable zone for the updated SWEET-Cat stars. The coloured line shows the theoretical habitable zone, while the dots shows the location of the planets in the actual system. The blue lines show the habitable zone of the three stars where a planet is located within it (green points). The red dots and orange lines are systems which does not lie within the habitable zone. Finally, the green line shows the location of the Sun's habitable zone and the first five planets placement. In this model both Earth and Mars are within the habitable zone.

Table 5.3: Host star and planetary properties of GJ 785, HD 37124, and KELT-6; all which have an exoplanet in the habitable zone.

Parameter	GJ 785	HD 37124	KELT-6
Stellar parameters			
T_{eff}	$(5087 \pm 48)\,\text{K}$	$(5460 \pm 35)\,\text{K}$	$(6246 \pm 88)\,\text{K}$
$\log g$	$(4.30 \pm 0.10)\,\text{dex}$	$(4.26 \pm 0.04)\,\text{dex}$	$(4.22 \pm 0.09)\,\text{dex}$
[Fe /H]	$(-0.01 \pm 0.03)\,\text{dex}$	$(-0.42 \pm 0.03)\,\text{dex}$	$(-0.22 \pm 0.06)\,\text{dex}$
Luminosity	$0.72 L_{\odot}$	$1.10 L_{\odot}$	$2.70 L_{\odot}$
V magnitude	6.13	7.68	10.38
Planetary parameters			
Planet	GJ 785 c	HD 37124 c	KELT-6 c
Period	525 days	885 days	1276 days
Mass	$0.076 M_J$	$0.652 M_J$	$3.710 M_J$
Semi-major axis	1.18 AU	1.71 AU	2.39 AU
Inner HZ limit	0.86 AU	1.04 AU	1.56 AU
Outer HZ limit	1.53 AU	1.84 AU	2.70 AU

Torres et al. (2010) if the literature parameters of T_{eff}, $\log g$, and [Fe /H] are used. However, when comparing with the new radius derived using the parameters presented here, the results can differ by up to 65%. This is shown in Figure 5.3 how the radius calculated from Torres et al. (2010) differs between the literature atmospheric parameters and the new homogeneous atmospheric parameters presented here. Note that stellar radii are provided by many of the authors from different discovery papers, but here the atmospheric parameters via the derivation of the stellar radius, as described above, are compared, rather than comparing the stellar radii from different methods.

In the sections below there follow a discussion of the systems (seven stars, eight exoplanets) where the radius or mass of the stars changes more than 25% and how this influences the planetary parameters. The changes in radius for a star is primarily due to changes in $\log g$, which can be used as an indicator of the evolutionary stage of a star.

The planetary radius, mass, and semi-major axis were re-derived when possible following the three simple scaling relations based on Newton's law of gravity (Newton, 1687) for deriving mass and distance and simple geometry for radius (see e.g. Torres et al., 2008)

$$M_{\text{pl,new}} = \left(\frac{M_{*,\text{lit}}}{M_{*,\text{new}}} \right)^{-2/3} M_{\text{pl,lit}} \tag{5.3}$$

$$R_{\text{pl,new}} = \left(\frac{R_{*,\text{lit}}}{R_{*,\text{new}}} \right) R_{\text{pl,lit}} \tag{5.4}$$

$$a_{\text{pl,new}} = \left(\frac{M_{*,\text{lit}}}{M_{*,\text{new}}} \right)^{1/3} a_{\text{pl,lit}}, \tag{5.5}$$

where the subscript "lit" denotes the value from the literature used in the comparison, the subscript "new" indicates the new computed values, the subscript "pl" is short for planet, and the subscript "$*$" is short for star; M, R, and a are mass, radius, and semi-major axis, respectively. Note that for the literature values, the values reported directly from the literature were used and not the derived radius and mass from Torres et al. (2010). To identify outliers, the radii and masses were compared when derived from Torres et al. (2010) since this is a measure of how the atmospheric parameters have changed.
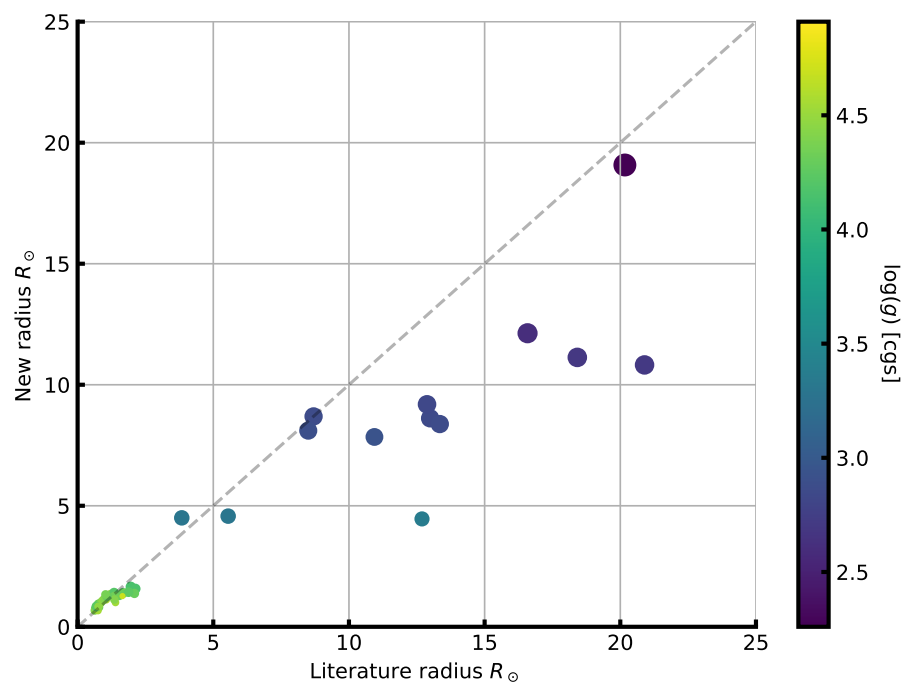
Figure 5.3: Stellar radius on both axes calculated based on Torres et al. (2010). The x-axis shows the stellar radius based on the atmospheric parameters from the literature, while the y-axis indicates the new homogeneous parameters presented here. The colour and size indicate the surface gravity. This clearly shows that the disagreement is biggest for more evolved stars.

5.3.2.1 HAT-P-46

HAT-P-46 has two known exoplanets according to Hartman et al. (2014). The outer planet HAT-P-46 c is not transiting, hence the radius is not known for this planet. The results presented above for this star come from UVES/VLT data with a S/N of 208. Hartman et al. (2014) derived the following spectroscopic parameters: $T_{\mathrm{eff}} = (6120 \pm 100)\,\mathrm{K}$, $\log g = (4.25 \pm 0.11)\,\mathrm{dex}$, and [Fe /H] $= (0.30 \pm 0.10)\,\mathrm{dex}$. Note that for this star the asteroseismic correction applied (see Section 5.3) results in a corrected $\log g$ below 4.2dex, so the spectroscopic $\log g$ was used for this star.

If mass and radius is derived of HAT-P-46 b with the new parameters, the radius obtained is $R_{\mathrm{pl}} = 0.93 R_J$, while Hartman et al. (2014) derived $R_{\mathrm{pl}} = 1.28 R_J$. No change in mass is seen (Hartman et al. 2014 found $M_{\mathrm{pl}} = 0.49 M_J$); however, there is a decrease in the radius, and this results with a more dense planet, $\rho_{\mathrm{pl}} = 0.76\,\mathrm{g/cm^3}$ from $\rho_{\mathrm{pl}} = (0.28 \pm 0.10)\,\mathrm{g/cm^3}$.

Only the minimum mass is known for the secondary companions, as it does not transit HAT-P-46 seen from Earth. With the derived parameters here, the minimum mass is $M \sin i_{\mathrm{pl}} = 1.97 M_J$, where Hartman et al. (2014) presented $M \sin i_{\mathrm{pl}} = 2.00 M_J$, so a very small change, as expected.

5.3.2.2 HD 120084

The exoplanet orbiting this star with a period of 2082 days and a quite eccentric orbit at 0.66 was discovered by Sato et al. (2013). The atmospheric parameters were derived by Takeda et al. (2008) using a similar method to that described here. The quality of the spectra they analysed, however, were not as high as those used here. Using the HIDES spectrograph at the 188 cm reflector at NAOJ, Takeda et al. (2008) reported an average S/N for their sample of 100-300 objects at a resolving power of 67 000. The spectrum used here is from ESPaDOnS with a resolving power of 81 000, and with a S/N for this star at 850. With the new parameters obtained, there is a slight decrease in stellar mass for the star at $1.93 M_\odot$ compared to $2.39 M_\odot$ obtained by Takeda et al. (2008), hence the minimum planetary mass is also slightly lower, from $m_{\mathrm{pl}} \sin i = 4.5 M_J$ to $m_{\mathrm{pl}} \sin i = 3.9 M_J$. The stellar radius decrease by 28%, from $9.12 R_\odot$ to $7.81 R_\odot$. Since there are no observations of the planet transiting, the planetary radius has not been computed.

5.3.2.3 HD 233604

HD 233604 b was discovered by Nowak et al. (2013), while the stellar atmospheric parameters of the star were derived by Zieliński et al. (2012), who used the same method as described here using the HRS spectrograph at HET with a resolving power of 60 000 with a typical S/N at 200-250. For the analysis presented here, a spectrum from the FIES spectrograph was used with a slightly higher resolution at 67 000, and similar but also slightly higher S/N at 320 for this star.

This planet is in a very close orbit with a semi-major axis of $\sim 15 R_*$ (R_* is the stellar radius) using the parameters from Nowak et al. (2013). Using the updated parameters presented in this paper the stellar mass increase slightly from $1.5 M_\odot$ to $1.9 M_\odot$, and a decrease in stellar radius from $10.5 R_\odot$ to $8.6 R_\odot$. This increases the semi-major axis to $\sim 21 R_*$. We note that the correct stellar radii are used to describe the semi-major axis in both cases. The increase in stellar mass leads to an increase in the minimum planetary mass, from $m_{\mathrm{pl}} \sin i = 6.58 M_J$ to $m_{\mathrm{pl}} \sin i = 7.79 M_J$.

Moreover, Nowak et al. (2013) found a high Li abundance at $A(\mathrm{Li})_{\mathrm{LTE}} = (1.400 \pm 0.042)\,\mathrm{dex}$ for this star and speculated that this star might have engulfed a planet. A more likely explanation is that

this star has not yet reached the first dredge-up process (Nowak et al., 2013). In the analysis here a much lower value is found, $A(\text{Li})_{\text{LTE}} = 0.92$ dex, and hence the star is not believed to be Li rich. The Li abundance found here is in excellent agreement with Adamów et al. (2014). Even applying a NLTE correction, as was done in Adamów et al. (2014) ($A(\text{Li})_{\text{NLTE}} = 1.08$), this star is not Li rich.

5.3.2.4   HD 5583

This exoplanet was discovered by Niedzielski et al. (2016) with an orbital period of 139 days around a K giant. This exoplanet was discovered with the radial velocity technique, and the planetary radius is not known. The stellar parameters were derived in a similar manner to that presented here (see Niedzielski et al., 2016, and references therein); the biggest disagreement is in the surface gravity. Here was derived a $\log g$ that is higher by 0.34 dex, which gives a stellar radius that is smaller by 37%. The derived mass is 15% higher, which in turn increases the minimum planetary mass from $m_{\text{pl}} \sin i = 5.78 M_J$ to $m_{\text{pl}} \sin i = 8.63 M_J$. Even with the increase in mass, it is still within the planetary regime for most inclinations, as was noted by Niedzielski et al. (2016).

5.3.2.5   HD 81688

This exoplanet was discovered by Sato et al. (2008) with the RV method. The host star is a metal-poor K giant. The atmospheric parameters presented in Sato et al. (2008) are obtained via the same method as presented here, and the agreement is quite good. Once again the big disagreement is in the surface gravity: Here was obtained 0.48 dex higher. Even though the stellar atmospheric parameters, and hence the planetary parameters, do change, the radius and mass derived are not far from the values presented in the paper by Sato et al. (2008). This is a case where the star was marked as an outlier, due to the comparison between the radius and mass derived from Torres et al. (2010).

The new stellar mass is the same as before, $2.1 M_\odot$. The stellar radius changed from $13.0 R_\odot$ to $10.8 R_\odot$. Since a transit of this star has not been observed and the stellar mass remains the same, there is no change in the planetary parameters.

It is worth noting that this system is in an interesting configuration with a very close orbit around an evolved star. This system, among others, has been the subject of work on planet engulfment (see e.g. Kunitomo et al., 2011).

5.3.2.6   HIP 107773

The planetary companion was presented in Jones et al. (2015) as an exoplanet around an intermediate-mass evolved star. The stellar parameters were obtained from the analysis by Jones et al. (2011) using the same method as presented here, but with a different line list, which might lead to some disagreements. A higher $\log g$ (2.83 dex compared to 2.60 dex) was derived here, thus the star is slightly smaller with $11.6 R_\odot$ to $9.2 R_\odot$ and $2.4 M_\odot$ to $2.1 M_\odot$ for radius and mass of the star, respectively. The other atmospheric parameters are very similar to those derived by Jones et al. (2011). This leads to a reduced minimum mass of the planetary companion from $m \sin i = 1.98 M_J$ to $m \sin i = 1.78 M_J$. The planetary radius has not been measured.

5.3.2.7   WASP-97

The exoplanet orbiting WASP-97 was discovered by Hellier et al. (2014). The host star parameters were derived using a similar method to that described here after co-adding several spectra from the CORALIE spectrograph. They reach a S/N of 100 with a spectral resolution of 50 000. The parameters presented here come from the UVES spectrograph with a S/N of more than 200.

The parameters do not change much for this planet. The minimum planetary mass changes from $m_{\mathrm{pl}} \sin i = 1.32 M_J$ to $m_{\mathrm{pl}} \sin i = 1.37 M_J$ and the radius from $1.13 R_J$ to $1.42 R_J$. This affects the density quite strongly; it changes from $1.13\,\mathrm{g/cm^3}$ to $0.59\,\mathrm{g/cm^3}$. This exoplanet is then in the same category as Saturn; its density is lower than water, but it is slightly larger than Jupiter.

5.3.2.8 ω Serpentis (ome Ser)

The exoplanet orbiting this star with a period of 277 days and an eccentric orbit at 0.11 was also presented by Sato et al. (2013). The atmospheric parameters were derived in the same way as for HD 120084. Data from FIES with a resolving power of 67 000 was used, and with a S/N for this star of 1168. With the new parameters a slightly higher stellar mass for the star is obtained at $2.19 M_\odot$ compared to the value of $2.17 M_\odot$ obtained by Takeda et al. (2008). This change is not significant enough to change the minimum planetary mass at $m_{\mathrm{pl}} \sin i = 1.7 M_J$. The stellar radius decreases by more than one solar radius, from $12.3 R_\odot$ to $11.1 R_\odot$. However, since there are no observations of transiting exoplanets, any change in planetary radius cannot be detected.

5.3.2.9   o Ursa Major (omi UMa)

omi UMa b was discovered by Sato et al. (2012) using the RV method. The stellar parameters are from Takeda et al. (2008), as discussed above. The spectrum used for this star is from ESPaDOnS with a S/N of more than 500 compared to the value of 100-300 reached for the large sample presented in Takeda et al. (2008). The luminosity and mass for omi UMa were obtained from theoretical evolutionary tracks (see Sato et al., 2012, and references therein). The radius was then estimated using the Stefan-Boltzmann relationship, using the measured luminosity and T_{eff}.

The parameters presented here mainly differ in the surface gravity: here it is 0.72 dex higher at $\log g = 3.36$. This leads to a big change in stellar mass and radius from $3.1 M_\odot$ to $1.6 M_\odot$ and $14.1 R_\odot$ to $4.5 R_\odot$, respectively. Sato et al. (2012) have reported that omi UMa b is the first planet candidate around a star more massive than $3 M_\odot$, which is not supported by the results presented here. With these updated results, the minimum mass of the planet is now $m \sin i = 2.7 M_J$, whereas previously it was $m \sin i = 4.1 M_J$ (Sato et al., 2012). The exoplanet is not reported to transit, as seen from Earth, so the radius for this exoplanet is not known, which would have changed a great deal with these new results.

5.4   Discovering two giant planet populations

SWEET-Cat was recently combined with planetary masses to see two distinctive populations for giant planets by Santos et al. (2017). This can be seen in the mass histogram in Figure 5.4 for the full sample of giant planets, with masses higher than 1 Jupiter mass and lower than 20 Jupiter masses, and for a sample constrained by: $4000\,\mathrm{K} \leq T_{\mathrm{eff}} \leq 6500\,\mathrm{K}$ in order to have reliably atmospheric parameters from spectroscopic data, orbital periods above 10 days to avoid hot jupiters whose formation and migration

process is debated (Ngo et al., 2016, see e.g.), orbital periods below 5 years to allow for the sample to be reasonable complete. Last only stars brighter than 13 magnitude were included to ensure that the planetary masses can have been derived with reasonable confidence using the radial velocities.
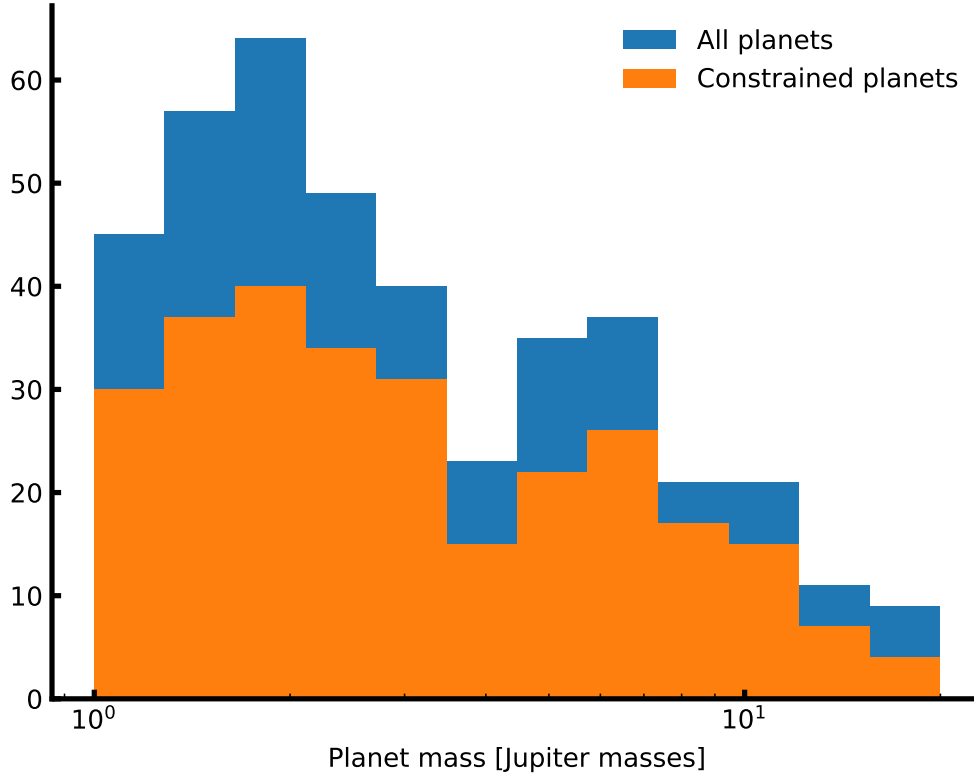
Figure 5.4: Giant planet masses for the full sample and constrained sample (see text for details). This study was performed by Santos et al. (2017) to distinct two giant planet populations.

By separating the distribution into two at $4M_{Jup}$, it can be shown (see Santos et al., 2017, for details) that the stars hosting the more massive giant planets are in average more metal-poor compared to the stars hosting the lower mass giant planets. This suggest two different stellar populations forming giant planets.

5.5   Updating SWEET-Cat

While SWEET-Cat is already a success, it is important to strive to improve the catalogue. Therefore several improvements for SWEET-Cat are planned. The most important additions are the derivation of chemical abundances and derivation of mass[4], radius, and age using stellar modelling.

With the deviation of chemical abundances, it is possible to make more in-depth studies of the planet hosts, e.g. by studying trends with condensation temperatures (see e.g. Adibekyan et al., 2016). By deriving the masses and radii of the planet hosting stars, the planetary parameters, (mass and radius,

---

[4]   The mass is currently available, however it is derived from a empirical relation.

and thus the bulk density) can be derived in a consistent way. This leads to a third improvement of SWEET-Cat; namely re-derived planetary parameters using the homogeneously derived stellar parameters.

When deriving the stellar masses and radii, the luminosity is also an output, which could be added to the future version of SWEET-Cat. This leads to simple estimates of the habitable zone limits (see the discussion above in Section 5.3.1). The implication of this is immediately evident: locating exoplanets in the habitable zone with the updated stellar parameters. This is of course particular interesting if the exoplanet is rocky.

Two other additions to SWEET-Cat could be the projected rotational velocity, $v \sin i$, and activity indicators such as $\log R'_{\mathrm{HK}}$. Note that $v \sin i$ will be difficult to derive. Here it is simplest to use synthesis to estimate this parameter, although for slow rotating stars (below $10\,\mathrm{km/s}$) it is difficult to measure accurately with a high precision. These slow rotating stars are the ones used with the method described above in e.g. Section 5.3. The activity is very important to include, since relations with stellar age and stellar rotation might be explored. Moreover, some non-obvious correlations such as the correlation found between $\log R'\mathrm{HK}$ and planetary surface gravity (Figueira et al., 2014; Hartman, 2010) might be explored as well.

The last update on the wish-list is for the web page itself. It could be made modern with plotting capabilities, and in tandem combine SWEET-Cat with an exoplanet database, such as Exoplanet.eu[5]. This will allow any user to quickly explorer relations between stellar and planetary properties. The tool for plotting has already been developed and is distributed along with other scripts developed during this PhD under `astro_scripts`[6].

---

[5] http://exoplanet.eu/
[6] Can be found here: https://github.com/DanielAndreasen/astro_scripts, and can be installed with `pip install astro-scripts`

Chapter 6

Future work

Appendix A

SWEET-Cat update of 50 planet hosts

Table A.1: Derived parameters for the 50 stars in our sample. The S/N was measured by ARES.

Star	T_{eff} [K]	$\log g$ [cgs]	[Fe /H]	ξ_{micro} [km/s]	ξ_{micro} fixed?	Instrument	S/N
BD -11 4672	4553 ± 75	4.87 ± 0.51	-0.30 ± 0.02	0.14 ± 0.07	yes	FIES	487
BD +49 828	5015 ± 36	$2.87 \pm 0.09^{\mathrm{a}}$	-0.01 ± 0.03	1.48 ± 0.04	no	FIES	567
GJ 785	5087 ± 48	4.42 ± 0.10	-0.01 ± 0.03	0.69 ± 0.10	no	HARPS	801
HATS-1	5969 ± 46	4.39 ± 0.06	-0.04 ± 0.04	1.06 ± 0.08	no	UVES	155
HATS-5	5383 ± 91	4.41 ± 0.22	0.08 ± 0.06	0.91 ± 0.14	no	UVES	158
HAT-P-12	4642 ± 106	4.53 ± 0.27	-0.26 ± 0.06	0.28 ± 0.63	no	FIES	185
HAT-P-24	6470 ± 181	4.33 ± 0.27	-0.41 ± 0.10	1.40 ± 0.03	yes	UVES	158
HAT-P-39	6745 ± 236	4.39 ± 0.47	-0.21 ± 0.12	1.53 ± 0.04	yes	UVES	127
HAT-P-42	5903 ± 66	$4.29 \pm 0.10^{\mathrm{a}}$	0.34 ± 0.05	1.19 ± 0.08	no	UVES	130
HAT-P-46	6421 ± 121	$4.53 \pm 0.14^{\mathrm{a}}$	0.16 ± 0.09	1.67 ± 0.18	no	UVES	208
HD 120084	4969 ± 40	$2.94 \pm 0.14^{\mathrm{a}}$	0.12 ± 0.03	1.41 ± 0.04	no	ESPaDOnS	852
HD 192263	4946 ± 46	4.61 ± 0.14	-0.05 ± 0.02	0.66 ± 0.12	no	HARPS	415
HD 219134	4767 ± 70	4.57 ± 0.17	0.00 ± 0.04	0.59 ± 0.24	no	ESPaDOnS	725
HD 220842	5999 ± 39	$4.30 \pm 0.06^{\mathrm{a}}$	-0.08 ± 0.03	1.21 ± 0.05	no	FIES	459
HD 233604	4954 ± 46	$2.86 \pm 0.11^{\mathrm{a}}$	-0.14 ± 0.04	1.61 ± 0.05	no	FIES	314
HD 283668	4841 ± 73	4.51 ± 0.18	-0.74 ± 0.04	0.16 ± 0.61	no	FIES	592
HD 285507	4620 ± 126	4.72 ± 0.61	0.04 ± 0.06	0.74 ± 0.43	no	UVES	239
HD 5583	4986 ± 35	$2.87 \pm 0.09^{\mathrm{a}}$	-0.35 ± 0.03	1.62 ± 0.04	no	FIES	933
HD 81688	4903 ± 21	$2.70 \pm 0.05^{\mathrm{a}}$	-0.21 ± 0.02	1.54 ± 0.02	no	b	1350, 860
HD 82886	5123 ± 18	$3.30 \pm 0.04^{\mathrm{a}}$	-0.25 ± 0.01	1.16 ± 0.02	no	c	1198,1294
HD 87883	4917 ± 68	4.53 ± 0.19	0.02 ± 0.03	0.46 ± 0.21	no	ESPaDOnS	753
HIP 107773	4957 ± 49	$2.83 \pm 0.09^{\mathrm{a}}$	0.04 ± 0.04	1.49 ± 0.05	no	UVES	218
HIP 11915	5770 ± 14	4.33 ± 0.03	-0.06 ± 0.01	0.95 ± 0.02	no	HARPS	709
HIP 116454	5042 ± 72	4.69 ± 0.15	-0.16 ± 0.03	0.71 ± 0.17	no	UVES	412

Table A.1: continued.

Star	T_{eff} [K]	$\log g$ [cgs]	[Fe /H]	ξ_{micro} [km/s]	ξ_{micro} fixed?	Instrument	S/N
HR 228	5042 ± 42	$3.30 \pm 0.09^{\text{a}}$	0.07 ± 0.03	1.14 ± 0.04	no	UVES	400
KELT-6	6246 ± 88	$4.22 \pm 0.09^{\text{a}}$	-0.22 ± 0.06	1.66 ± 0.13	no	FIES	374
Kepler-37	5378 ± 53	4.47 ± 0.12	-0.23 ± 0.04	0.58 ± 0.13	no	FIES	205
Kepler-444	5111 ± 43	4.50 ± 0.13	-0.51 ± 0.03	0.37 ± 0.15	no	FIES	675
mu Leo	4605 ± 94	$2.61 \pm 0.26^{\text{a}}$	0.25 ± 0.06	1.64 ± 0.11	no	ESPaDOnS	354
ome Ser	4928 ± 35	$2.69 \pm 0.06^{\text{a}}$	-0.11 ± 0.03	1.55 ± 0.04	no	FIES	1168
omi UMa	5499 ± 52	$3.36 \pm 0.07^{\text{a}}$	-0.01 ± 0.05	1.98 ± 0.06	no	ESPaDOnS	527
Qatar-2	4637 ± 316	4.53 ± 0.62	0.09 ± 0.17	0.63 ± 0.83	no	UVES	97
SAND364	4457 ± 104	$2.26 \pm 0.20^{\text{a}}$	-0.04 ± 0.06	1.60 ± 0.11	no	UVES	220
TYC+1422-614-1	4908 ± 41	$2.90 \pm 0.12^{\text{a}}$	-0.07 ± 0.03	1.57 ± 0.05	no	FIES	506
WASP-37	5917 ± 72	4.25 ± 0.15	-0.23 ± 0.05	0.59 ± 0.13	no	FIES	232
WASP-44	5612 ± 80	4.39 ± 0.30	0.17 ± 0.06	1.32 ± 0.13	no	UVES	125
WASP-52	5197 ± 83	4.55 ± 0.30	0.15 ± 0.05	1.16 ± 0.14	no	UVES	125
WASP-58	6039 ± 55	4.23 ± 0.10	-0.09 ± 0.04	1.12 ± 0.08	no	FIES	310
WASP-61	6265 ± 168	$4.21 \pm 0.21^{\text{a}}$	-0.38 ± 0.11	1.44 ± 0.02	yes	UVES	163
WASP-72	6570 ± 85	4.25 ± 0.13	0.15 ± 0.06	2.30 ± 0.15	no	UVES	174
WASP-73	6203 ± 32	$4.16 \pm 0.06^{\text{a}}$	0.20 ± 0.02	1.66 ± 0.04	np	[d]	193,231
WASP-75	6203 ± 46	$4.42 \pm 0.22^{\text{a}}$	0.24 ± 0.03	1.45 ± 0.06	no	UVES	189
WASP-76	6347 ± 52	$4.29 \pm 0.08^{\text{a}}$	0.36 ± 0.04	1.73 ± 0.06	no	UVES	165
WASP-82	6563 ± 55	$4.29 \pm 0.10^{\text{a}}$	0.18 ± 0.04	1.93 ± 0.08	no	UVES	239
WASP-88	6450 ± 61	$4.24 \pm 0.06^{\text{a}}$	0.03 ± 0.04	1.79 ± 0.09	no	UVES	174
WASP-94 A	6259 ± 34	$4.34 \pm 0.07^{\text{a}}$	0.35 ± 0.03	1.50 ± 0.04	no	UVES	356
WASP-94 B	6137 ± 21	$4.42 \pm 0.05^{\text{a}}$	0.33 ± 0.02	1.29 ± 0.03	no	UVES	397
WASP-95	5799 ± 31	$4.29 \pm 0.05^{\text{a}}$	0.22 ± 0.03	1.18 ± 0.04	no	UVES	247
WASP-97	5723 ± 52	4.24 ± 0.07	0.31 ± 0.04	1.03 ± 0.08	no	UVES	219

Table A.1: continued.

Star	T_{eff} [K]	$\log g$ [cgs]	[Fe /H]	ξ_{micro} [km/s]	ξ_{micro} fixed?	Instrument	S/N
WASP-99	6324 ± 89	4.34 ± 0.12	0.27 ± 0.06	1.83 ± 0.12	no	UVES	249
WASP-100	6853 ± 209	$4.15 \pm 0.26^{\mathrm{a}}$	-0.30 ± 0.12	1.87 ± 0.02	yes	UVES	166

[a] Spectroscopic $\log g$.

[b] Weighted average of ESPaDoNS and FIES results. The parameters are (FIES in parantheses): $T_{\mathrm{eff}} = 4870(4934) \pm 30(29)$, $\log g = 2.50(2.73) \pm 0.14(0.05)$, [Fe /H] $= -0.26(-0.19) \pm 0.03(0.02)$, and $\xi_{\mathrm{micro}} = 1.50(1.59) \pm 0.03(0.03)$.

[c] Weighted average of ESPaDoNS and FIES results. The parameters are (FIES in parantheses): $T_{\mathrm{eff}} = 5124(5121) \pm 22(29)$, $\log g = 3.30(3.31) \pm 0.05(0.07)$, [Fe /H] $= -0.25(-0.24) \pm 0.02(0.02)$, and $\xi_{\mathrm{micro}} = 1.15(1.17) \pm 0.03(0.04)$.

[d] Weighted average of UVES and FEROS results. The parameters are (FEROS in parantheses): $T_{\mathrm{eff}} = 6313(6162) \pm 61(37)$, $\log g = 4.26(4.14) \pm 0.15(0.06)$, [Fe /H] $= 0.22(0.19) \pm 0.04(0.03)$, and $\xi_{\mathrm{micro}} = 1.85(1.61) \pm 0.08(0.04)$.

Bibliography

Adamów, M., Niedzielski, A., Villaver, E., Wolszczan, A., and Nowak, G.: 2014, *A&A* **5**69, A55

Adibekyan, V., Delgado-Mena, E., Figueira, P., Sousa, S. G., Santos, N. C., González Hernández, J. I., Minchev, I., Faria, J. P., Israelian, G., Harutyunyan, G., Suárez-Andrés, L., and Hakobyan, A. A.: 2016, *A&A* **5**92, A87

Adibekyan, V. Z., Benamati, L., Santos, N. C., Alves, S., Lovis, C., Udry, S., Israelian, G., Sousa, S. G., Tsantaki, M., Mortier, A., Sozzetti, A., and De Medeiros, J. R.: 2015, *MNRAS* **4**50, 1900

Adibekyan, V. Z., Figueira, P., Santos, N. C., Mortier, A., Mordasini, C., Delgado Mena, E., Sousa, S. G., Correia, A. C. M., Israelian, G., and Oshagh, M.: 2013, *A&A* **5**60, A51

Aerts, C., Christensen-Dalsgaard, J., and Kurtz, D. W.: 2010, *Asteroseismology*, Springer-Verlag

Andreasen, D. T., Sousa, S. G., Delgado Mena, E., Santos, N. C., Lebzelter, T., Mucciarelli, A., and Neil, J. J.: 2017a, *A&A* **5**85, A143

Andreasen, D. T., Sousa, S. G., Delgado Mena, E., Santos, N. C., Tsantaki, M., Rojas-Ayala, B., and Neves, V.: 2016, *A&A* **5**85, A143

Andreasen, D. T., Sousa, S. G., Tsantaki, M., Teixeira, G. D. C., Mortier, A., Santos, N. C., Suárez-Andrés, L., Delgado Mena, E., and Ferreira, A. C. S.: 2017b, *A&A* **6**00, A69

Balachandran, S.: 1990, *ApJ* **3**54, 310

Bedding, T. R., Mosser, B., Huber, D., Montalbán, J., Beck, P., Christensen-Dalsgaard, J., Elsworth, Y. P., García, R. A., Miglio, A., Stello, D., White, T. R., De Ridder, J., Hekker, S., Aerts, C., Barban, C., Belkacem, K., Broomhall, A.-M., Brown, T. M., Buzasi, D. L., Carrier, F., Chaplin, W. J., di Mauro, M. P., Dupret, M.-A., Frandsen, S., Gilliland, R. L., Goupil, M.-J., Jenkins, J. M., Kallinger, T., Kawaler, S., Kjeldsen, H., Mathur, S., Noels, A., Silva Aguirre, V., and Ventura, P.: 2011, *Nature* **4**71, 608

Bertaux, J. L., Lallement, R., Ferron, S., Boonne, C., and Bodichon, R.: 2014, *A&A* **5**64, A46

Blackwell, D. E. and Shallis, M. J.: 1977, *MNRAS* **1**80, 177

Bochanski, J. J., Hawley, S. L., Covey, K. R., West, A. A., Reid, I. N., Golimowski, D. A., and Ivezić, Ž.: 2010, *AJ* **1**39, 2679

Casagrande, L., Portinari, L., and Flynn, C.: 2006, *MNRAS* **3**73, 13

Cayrel, R.: 1988, in G. Cayrel de Strobel and M. Spite (eds.), *The Impact of Very High S/N Spectroscopy on Stellar Physics*, Vol. 132 of *IAU Symposium*, p. 345

Chaplin, W. J., Kjeldsen, H., Christensen-Dalsgaard, J., Basu, S., Miglio, A., Appourchaux, T., Bedding, T. R., Elsworth, Y., García, R. A., Gilliland, R. L., Girardi, L., Houdek, G., Karoff, C., Kawaler, S. D., Metcalfe, T. S., Molenda-Żakowicz, J., Monteiro, M. J. P. F. G., Thompson, M. J., Verner, G. A., Ballot, J., Bonanno, A., Brandão, I. M., Broomhall, A.-M., Bruntt, H., Campante, T. L., Corsaro, E., Creevey, O. L., Doğan, G., Esch, L., Gai, N., Gaulme, P., Hale, S. J., Handberg, R., Hekker, S., Huber, D., Jiménez, A., Mathur, S., Mazumdar, A., Mosser, B., New, R., Pinsonneault, M. H., Pricopi, D., Quirion, P.-O., Régulo, C., Salabert, D., Serenelli, A. M., Silva Aguirre, V., Sousa, S. G., Stello, D., Stevens, I. R., Suran, M. D., Uytterhoeven, K., White, T. R., Borucki, W. J., Brown, T. M., Jenkins, J. M., Kinemuchi, K., Van Cleve, J., and Klaus, T. C.: 2011, *Science* **332**, 213

Christensen-Dalsgaard, J., Kjeldsen, H., Brown, T. M., Gilliland, R. L., Arentoft, T., Frandsen, S., Quirion, P.-O., Borucki, W. J., Koch, D., and Jenkins, J. M.: 2010, *ApJL* **7**13, L164

Czekala, I., Andrews, S. M., Mandel, K. S., Hogg, D. W., and Green, G. M.: 2015, *ApJ* **8**12, 128

Dekker, H., D'Odorico, S., Kaufer, A., Delabre, B., and Kotzlowski, H.: 2000, in M. Iye and A. F. Moorwood (eds.), *Optical and IR Telescope Instrumentation and Detectors*, Vol. 4008 of *Proceedings of the SPIE*, pp 534–545

Donati, J.-F.: 2003, in J. Trujillo-Bueno and J. Sanchez Almeida (eds.), *Solar Polarization*, Vol. 307 of *Astronomical Society of the Pacific Conference Series*, p. 41

Ducati, J. R.: 2002, *VizieR Online Data Catalog* 2237

Favata, F., Micela, G., and Sciortino, S.: 1997, *A&A* **323**, 809

Figueira, P., Oshagh, M., Adibekyan, V. Z., and Santos, N. C.: 2014, *A&A* **5**72, A51

Frandsen, S. and Lindberg, B.: 1999, in H. Karttunen and V. Piirola (eds.), *Astrophysics with the NOT*, p. 71

Gonzalez, G., Carlson, M. K., and Tobin, R. W.: 2010, *MNRAS* **4**03, 1368

Gonzalez, G. and Laws, C.: 2000, *AJ* **1**19, 390

Gray, D. F.: 2005, *The Observation and Analysis of Stellar Photospheres, 3rd ed.*

Griffin, R. and Griffin, R.: 1967, *MNRAS* **1**37, 253

Grundahl, F., Fredslund Andersen, M., Christensen-Dalsgaard, J., Antoci, V., Kjeldsen, H., Handberg, R., Houdek, G., Bedding, T. R., Pallé, P. L., Jessen-Hansen, J., Silva Aguirre, V., White, T. R., Frandsen, S., Albrecht, S., Andersen, M. I., Arentoft, T., Brogaard, K., Chaplin, W. J., Harpsøe, K., Jørgensen, U. G., Karovicova, I., Karoff, C., Kjærgaard Rasmussen, P., Lund, M. N., Sloth Lundkvist, M., Skottfelt, J., Norup Sørensen, A., Tronsgaard, R., and Weiss, E.: 2017, *ApJ* **8**36, 142

Gustafsson, B., Edvardsson, B., Eriksson, K., Jørgensen, U. G., Nordlund, Å., and Plez, B.: 2008, *A&A* **4**86, 951

Hartman, J. D.: 2010, *ApJL* **7**17, L138

Hartman, J. D., Bakos, G. Á., Torres, G., Kovács, G., Johnson, J. A., Howard, A. W., Marcy, G. W., Latham, D. W., Bieryla, A., Buchhave, L. A., Bhatti, W., Béky, B., Csubry, Z., Penev, K., de Val-Borro, M., Noyes, R. W., Fischer, D. A., Esquerdo, G. A., Everett, M., Szklenár, T., Zhou, G., Bayliss, D., Shporer, A., Fulton, B. J., Sanchis-Ojeda, R., Falco, E., Lázár, J., Papp, I., and Sári, P.: 2014, *AJ* **1**47, 128

Hellier, C., Anderson, D. R., Cameron, A. C., Delrez, L., Gillon, M., Jehin, E., Lendl, M., Maxted, P. F. L., Pepe, F., Pollacco, D., Queloz, D., Ségransan, D., Smalley, B., Smith, A. M. S., Southworth, J., Triaud, A. H. M. J., Udry, S., and West, R. G.: 2014, *MNRAS* **4**40, 1982

Hinkel, N. R., Young, P. A., Pagano, M. D., Desch, S. J., Anbar, A. D., Adibekyan, V., Blanco-Cuaresma, S., Carlberg, J. K., Delgado Mena, E., Liu, F., Nordlander, T., Sousa, S. G., Korn, A., Gruyters, P., Heiter, U., Jofré, P., Santos, N. C., and Soubiran, C.: 2016, *ApJS* **2**26, 4

Hinkle, K., Wallace, L., and Livingston, W.: 1995a, *Publications of the ASP* **1**07, 1042

Hinkle, K. H., Wallace, L., and Livingston, W.: 1995b, in A. J. Sauval, R. Blomme, and N. Grevesse (eds.), *Laboratory and Astronomical High Resolution Spectra*, Vol. 81 of *Astronomical Society of the Pacific Conference Series*, p. 66

Huber, D., Silva Aguirre, V., Matthews, J. M., Pinsonneault, M. H., Gaidos, E., García, R. A., Hekker, S., Mathur, S., Mosser, B., Torres, G., Bastien, F. A., Basu, S., Bedding, T. R., Chaplin, W. J., Demory, B.-O., Fleming, S. W., Guo, Z., Mann, A. W., Rowe, J. F., Serenelli, A. M., Smith, M. A., and Stello, D.: 2014, *ApJS* **2**11, 2

Husser, T.-O., Wende-von Berg, S., Dreizler, S., Homeier, D., Reiners, A., Barman, T., and Hauschildt, P. H.: 2013, *A&A* **5**53, A6

Jofré, P., Heiter, U., Soubiran, C., Blanco-Cuaresma, S., Worley, C. C., Pancino, E., Cantat-Gaudin, T., Magrini, L., Bergemann, M., González Hernández, J. I., Hill, V., Lardo, C., de Laverny, P., Lind, K., Masseron, T., Montes, D., Mucciarelli, A., Nordlander, T., Recio Blanco, A., Sobeck, J., Sordo, R., Sousa, S. G., Tabernero, H., Vallenari, A., and Van Eck, S.: 2014, *A&A* **5**64, A133

Jones, M. I., Jenkins, J. S., Rojo, P., and Melo, C. H. F.: 2011, *A&A* **5**36, A71

Jones, M. I., Jenkins, J. S., Rojo, P., Olivares, F., and Melo, C. H. F.: 2015, *A&A* **5**80, A14

Kaufer, A., Stahl, O., Tubbesing, S., Nørregaard, P., Avila, G., Francois, P., Pasquini, L., and Pizzella, A.: 1999, *The Messenger* **9**5, 8

Kippenhahn, R. and Weigert, A.: 1994, *Stellar Structure and Evolution*, Springer-Verlag

Kirkpatrick, J. D., Henry, T. J., and McCarthy, Jr., D. W.: 1991, *ApJS* **7**7, 417

Kjeldsen, H. and Bedding, T. R.: 1995, *A&A* **2**93, 87

Kopparapu, R. K., Ramirez, R., Kasting, J. F., Eymet, V., Robinson, T. D., Mahadevan, S., Terrien, R. C., Domagal-Goldman, S., Meadows, V., and Deshpande, R.: 2013, *ApJ* **7**65, 131

Kunitomo, M., Ikoma, M., Sato, B., Katsuta, Y., and Ida, S.: 2011, *ApJ* **7**37, 66

Kupka, F. G., Ryabchikova, T. A., Piskunov, N. E., Stempels, H. C., and Weiss, W. W.: 2000, *Baltic Astronomy* **9**, 590

Kurucz, R.: 1993, *ATLAS9 Stellar Atmosphere Programs and 2 km/s grid. Kurucz CD-ROM No. 13. Cambridge, Mass.: Smithsonian Astrophysical Observatory, 1993.* 13

Lebzelter, T., Seifahrt, A., Uttenthaler, S., Ramsay, S., Hartman, H., Nieva, M.-F., Przybilla, N., Smette, A., Wahlgren, G. M., Wolff, B., Hussain, G. A. J., Käufl, H. U., and Seemann, U.: 2012, *A&A* **5**39, A109

Lindgren, S., Heiter, U., and Seifahrt, A.: 2016, *A&A* **5**86, A100

Mayor, M., Pepe, F., Queloz, D., Bouchy, F., Rupprecht, G., Lo Curto, G., Avila, G., Benz, W., Bertaux, J.-L., Bonfils, X., Dall, T., Dekker, H., Delabre, B., Eckert, W., Fleury, M., Gilliotte, A., Gojak, D., Guzman, J. C., Kohler, D., Lizon, J.-L., Longinotti, A., Lovis, C., Megevand, D., Pasquini, L., Reyes, J., Sivan, J.-P., Sosnowska, D., Soto, R., Udry, S., van Kesteren, A., Weber, L., and Weilenmann, U.: 2003, *The Messenger* **1**14, 20

Mayor, M. and Queloz, D.: 1995, *A Jupiter-mass companion to a solar-type star*

McWilliam, A.: 1990, *ApJS* **7**4, 1075

Mortier, A., Santos, N. C., Sousa, S., Israelian, G., Mayor, M., and Udry, S.: 2013a, *A&A* **5**51, A112

Mortier, A., Santos, N. C., Sousa, S. G., Adibekyan, V. Z., Delgado Mena, E., Tsantaki, M., Israelian, G., and Mayor, M.: 2013b, *A&A* **5**57, A70

Mortier, A., Sousa, S. G., Adibekyan, V. Z., Brandão, I. M., and Santos, N. C.: 2014, *A&A* **5**72, A95

Neuforge-Verheecke, C. and Magain, P.: 1997, *A&A* **3**28, 261

Newton, I.: 1687, *Philosophiae Naturalis Principia Mathematica. Auctore Js. Newton*

Ngo, H., Knutson, H. A., Hinkley, S., Bryan, M., Crepp, J. R., Batygin, K., Crossfield, I., Hansen, B., Howard, A. W., Johnson, J. A., Mawet, D., Morton, T. D., Muirhead, P. S., and Wang, J.: 2016, *ApJ* **8**27, 8

Nicholls, C. P., Lebzelter, T., Smette, A., Wolff, B., Hartman, H., Käufl, H.-U., Przybilla, N., Ramsay, S., Uttenthaler, S., Wahlgren, G. M., Bagnulo, S., Hussain, G. A. J., Nieva, M.-F., Seemann, U., and Seifahrt, A.: 2017, *A&A* **5**98, A79

Niedzielski, A., Villaver, E., Nowak, G., Adamów, M., Kowalik, K., Wolszczan, A., Deka-Szymankiewicz, B., Adamczyk, M., and Maciejewski, G.: 2016, *A&A* **5**88, A62

Nowak, G., Niedzielski, A., Wolszczan, A., Adamów, M., and Maciejewski, G.: 2013, *ApJ* **7**70, 53

Önehag, A., Heiter, U., Gustafsson, B., Piskunov, N., Plez, B., and Reiners, A.: 2012, *A&A* **5**42, A33

Piskunov, N. E., Kupka, F., Ryabchikova, T. A., Weiss, W. W., and Jeffery, C. S.: 1995, *A&A Supp.* **1**12, 525

Ramírez, I., Allende Prieto, C., and Lambert, D. L.: 2013, *ApJ* **7**64, 78

Ramírez, I., Fish, J. R., Lambert, D. L., and Allende Prieto, C.: 2012, *ApJ* **7**56, 46

Ramírez, I. and Meléndez, J.: 2005, *ApJ* **6**26, 465

Santos, N. C., Adibekyan, V., Figueira, P., Andreasen, D. T., Barros, S. C. C., Delgado-Mena, E., Demangeon, O., Faria, J. P., Oshagh, M., Sousa, S. G., Viana, P. T. P., and Ferreira, A. C. S.: 2017, *ArXiv e-prints*

Santos, N. C., Israelian, G., and Mayor, M.: 2004, *A&A* **4**15, 1153

Santos, N. C., Sousa, S. G., Mortier, A., Neves, V., Adibekyan, V., Tsantaki, M., Delgado Mena, E., Bonfils, X., Israelian, G., Mayor, M., and Udry, S.: 2013, *A&A* **5**56, A150

Sato, B., Izumiura, H., Toyota, E., Kambe, E., Ikoma, M., Omiya, M., Masuda, S., Takeda, Y., Murata, D., Itoh, Y., Ando, H., Yoshida, M., Kokubo, E., and Ida, S.: 2008, *PASJ* **6**0, 539

Sato, B., Omiya, M., Harakawa, H., Izumiura, H., Kambe, E., Takeda, Y., Yoshida, M., Itoh, Y., Ando, H., Kokubo, E., and Ida, S.: 2012, *PASJ* 64

Sato, B., Omiya, M., Harakawa, H., Liu, Y.-J., Izumiura, H., Kambe, E., Takeda, Y., Yoshida, M., Itoh, Y., Ando, H., Kokubo, E., and Ida, S.: 2013, *PASJ* 65

Smiljanic, R., Korn, A. J., Bergemann, M., Frasca, A., Magrini, L., Masseron, T., Pancino, E., Ruchti, G., San Roman, I., Sbordone, L., Sousa, S. G., Tabernero, H., Tautvaišienė, G., Valentini, M., Weber, M., Worley, C. C., Adibekyan, V. Z., Allende Prieto, C., Barisevičius, G., Biazzo, K., Blanco-Cuaresma, S., Bonifacio, P., Bragaglia, A., Caffau, E., Cantat-Gaudin, T., Chorniy, Y., de Laverny, P., Delgado-Mena, E., Donati, P., Duffau, S., Franciosini, E., Friel, E., Geisler, D., González Hernández, J. I., Gruyters, P., Guiglion, G., Hansen, C. J., Heiter, U., Hill, V., Jacobson, H. R., Jofre, P., Jönsson, H., Lanzafame, A. C., Lardo, C., Ludwig, H.-G., Maiorca, E., Mikolaitis, Š., Montes, D., Morel, T., Mucciarelli, A., Muñoz, C., Nordlander, T., Pasquini, L., Puzeras, E., Recio-Blanco, A., Ryde, N., Sacco, G., Santos, N. C., Serenelli, A. M., Sordo, R., Soubiran, C., Spina, L., Steffen, M., Vallenari, A., Van Eck, S., Villanova, S., Gilmore, G., Randich, S., Asplund, M., Binney, J., Drew, J., Feltzing, S., Ferguson, A., Jeffries, R., Micela, G., Negueruela, I., Prusti, T., Rix, H.-W., Alfaro, E., Babusiaux, C., Bensby, T., Blomme, R., Flaccomio, E., François, P., Irwin, M., Koposov, S., Walton, N., Bayo, A., Carraro, G., Costado, M. T., Damiani, F., Edvardsson, B., Hourihane, A., Jackson, R., Lewis, J., Lind, K., Marconi, G., Martayan, C., Monaco, L., Morbidelli, L., Prisinzano, L., and Zaggia, S.: 2014, *A&A* **5**70, A122

Sneden, C. A.: 1973, *Ph.D. thesis*, THE UNIVERSITY OF TEXAS AT AUSTIN.

Soubiran, C., Le Campion, J.-F., Brouillet, N., and Chemin, L.: 2016, *A&A* **5**91, A118

Sousa, S. G., Santos, N. C., Adibekyan, V., Delgado-Mena, E., and Israelian, G.: 2015, *A&A* **5**77, A67

Sousa, S. G., Santos, N. C., Israelian, G., Mayor, M., and Monteiro, M. J. P. F. G.: 2007, *A&A* **4**69, 783

Sousa, S. G., Santos, N. C., Israelian, G., Mayor, M., and Udry, S.: 2011, *A&A* **5**33, A141

Sousa, S. G., Santos, N. C., Mayor, M., Udry, S., Casagrande, L., Israelian, G., Pepe, F., Queloz, D., and Monteiro, M. J. P. F. G.: 2008, *A&A* **4**87, 373

Takeda, Y., Sato, B., and Murata, D.: 2008, *PASJ* **6**0, 781

Torres, G., Andersen, J., and Giménez, A.: 2010, *Astronomy and Astrophysics Reviews* **1**8, 67

Torres, G., Winn, J. N., and Holman, M. J.: 2008, *ApJ* **6**77, 1324

Tsantaki, M., Andreasen, D. T., Teixeira, G. D. C., Sousa, S. G., Santos, N. C., Delgado-Mena, E., and Bruzual, G.: 2017, *MNRAS* **5**55, A150

Tsantaki, M., Sousa, S. G., Adibekyan, V. Z., Santos, N. C., Mortier, A., and Israelian, G.: 2013, *A&A* **5**55, A150

Valenti, J. A. and Piskunov, N.: 1996, *A&A Supp.* **1**18, 595

Wolszczan, A. and Frail, D. A.: 1992, *Nature* **3**55, 145

Zieliński, P., Niedzielski, A., Wolszczan, A., Adamów, M., and Nowak, G.: 2012, *A&A* **5**47, A91